An investigation into a generalized Fisk-type heliospheric magnetic field

PJ Steyn

25261630

Dissertation submitted in partial fulfillment of the requirements for the degree *Magister Scientiae* in Space Physics at the Potchefstroom Campus of the North-West University

Supervisor: Prof RA Burger

November 2016

It all starts here ™

NORTH-WEST UNIVERSITY
YUNIBESITI YA BOKONE-BOPHIRIMA
NOORDWES-UNIVERSITEIT

To my wife, Linell, who walked this path with me from the very beginning.

The scientist does not study nature because it is useful;
he studies it because he delights in it,
and he delights in it because it is beautiful.
- Henri Poincaré

Abstract

The existence of a Fisk-type heliospheric magnetic field (HMF) has been contested since the Fisk field [*Fisk*, 1996] challenged the traditional view of the HMF first proposed by *Parker* [1958]. Several modifications of the original Fisk field model have been published in the past [*Schwadron*, 2002], of which the Fisk-Parker hybrid HMF model of *Burger and Hitge* [2004] is one. A detailed derivation and the uniqueness of the Fisk-Parker hybrid magnetic field expressions are shown in this study for the first time. This study also presents a divergence-free generalised Fisk HMF model to further test the existence of a Fisk-type field. The generalised Fisk field model implements a spatially dependent differential rotation rate of the photosphere by using newly developed transformations to map a magnetic field line from the solar wind source surface to the photosphere. The footpoint trajectories on the source surface as well the magnetic field line configurations are shown. The data analyses methods of *Forsyth et al.* [2002] are used to search for a signature of a generalised Fisk field model during solar minimum conditions using the magnetic field data from the first solar orbit of *Ulysses*. The generalised Fisk field agrees better with the observed magnetic field during all intervals scanned by *Ulysses* except during one interval. The 26-day recurrent cosmic-ray variations from data collected from the global neutron monitor network are investigated and agree well with the results of *Richardson et al.* [1999] and *Paizis et al.* [1999]. The results of this study provides further support for the existence of a Fisk-type HMF.

Keywords:
`Fisk-type heliospheric magnetic field, cosmic rays, recurrent cosmic-ray variations`

Opsomming

The bestaan van 'n Fisk-tipe heliosferiese magneetveld (HMV) is betwis sedert the Fisk veld [*Fisk*, 1996] die tradisionele uitgangspunt van die eerste HMV uitgedaag het wat voorgestel is deur *Parker* [1958]. Verskeie veranderinge van die oorspronklike Fisk veld is gepubliseer in die verlede [*Schwadron*, 2002], waarvan die Fisk-Parker hibried HMV van *Burger and Hitge* [2004] een is. 'n Gedetailleerde afleiding en uniekheid van die Fisk-Parker hibried magneetveld vergelykings word vir die eerste keer voorgestel in hierdie studie. Hierdie studie stel ook die divergensie-vrye veralgemeende Fisk HMV model bekend om die bestaan van 'n Fisk-tipe veld verder te toets. Die veralgemeende Fisk model implementeer 'n ruimtelike afhanklike differensiële rotasie tempo van die fotosfeer deur gebruik te maak van nuwe transformasies om magneetveldlyne van die sonwindbronoppervlak na die fotosfeer te spoor. Die voetpuntbane op die bronoppervlak sowel as die magneetveldlynopset word gewys. Die data-ontleding metodes van *Forsyth et al.* [2002] word gebruik om te soek vir 'n handtekening van die veralgemeende Fisk veld gedurende son-minimum toestande deur gebruik te maak van die magneetveld data van die eerste sonomwenteling van *Ulysses*. The veralgemeende Fisk veld stem beter ooreen met die geobserweerde magneetveld gedurende al die intervalle wat geskandeer is deur *Ulysses* behalwe vir een interval. Die 26-dag herhalende kosmiesestraalvariasies van die data versamel deur die globale neutron monitor netwerk is ondersoek en stem baie goed ooreen met die resultate van *Richardson et al.* [1999] en *Paizis et al.* [1999]. The resultate van hierdie studie gee verdere ondersteuning vir die bestaan van 'n Fisk-tipe HMV.

Sleutelwoorde:
`Fisk-tipe heliosferiese magneetveld, kosmiese strale, herhalende kosmiesestraalvariasies`

Nomenclature

Listed below are abbreviations used in the text. For the purpose of clarity, the abbreviations are written out in full when it appears for the first time in the text or wherever relevant.

AU	Astronomical Unit (1 AU $= 1.49 \times 10^8$ km)
CR	Cosmic Ray
CIR	Co-Rotating Interaction Region
CH	Coronal Hole
CME	Coronal Mass Ejection
CMF	Coronal Magnetic Field
FLS	Fast Latitude Scan
HCS	Heliospheric Current Sheet
HMF	Heliospheric Magnetic Field
LISM	Local Interstellar Medium
MHD	Magnetohydromagnetic
NM	Neutron Monitor
PCH	Polar Coronal Hole
PFSS	Potential Field Source Surface
SS	Source Surface
SW	Solar Wind
TS	Termination Shock
TPE	Transport Equation
WCS	Wavy Current Sheet
WSO	Wilcox Solar Observatory

Contents

Chapter 1

Introduction

The heliospheric magnetic field (HMF) has been studied extensively during the past ~ 60 years after *Parker* [1958] proposed the first successful model to describe both the solar origin and the geometrical structure of the HMF. The field structure of the Parker model is depicted by Archimedian spirals where the magnetic field lines remain on cones of constant heliographic latitudes. Since the advent of regular interplanetary spacecraft and satellite missions, more and more heliospheric magnetic field data have been collected and has lead to several modifications to the original Parker field model in an attempt to match theory with experiment. As a result, *Fisk* [1996] proposed a field model addressing the relationship between the differential rotation of the HMF footpoints on the photosphere and the subsequent super-radial expansion of these same field lines to the solar wind source surface resulting in extensive excursions of HMF field lines with heliographic latitude. Furthermore, *Burger and Hitge* [2004] modified the model of *Fisk* [1996] and proposed a Fisk-Parker hybrid HMF model, thereby introducing a field model valid at all latitudes by making use of a transition function to switch between the Parker field in the equatorial region, and the Fisk field at higher solar latitudes. The existence of Fisk-type fields have been debated in the past and this study addresses this very question.

The first aim of this dissertation is to introduce a generalised Fisk field model based on the original field of *Fisk* [1996]. The generalised Fisk field relaxes the assumption that the differential rotation rate of the photosphere, when mapped to the source surface where the solar wind plasma flow becomes radial, should be a constant fraction of the equatorial rotation rate of the Sun, but rather, have a meridional and azimuthal spacial dependence. Transformations mapping magnetic field lines from the solar wind source surface to the photosphere are presented. The need for a generalised Fisk field is two-fold: to have an HMF model valid at all latitudes that transforms from Parker behaviour to Fisk behaviour in a natural way without the use of a transition function, and to be able to explain the over- and underwinding of field lines reported by the *Ulysses* spacecraft mission during its first orbit around the Sun. The second aim is to use magnetic field data from *Ulysses* and cosmic-ray data from neutron monitors around the globe to compare the results of the generalised Fisk field with the standard Parker model during solar minimum conditions. This study finds evidence of the expected signature of a Fisk-type field.

In Chapter 2, the basic structure of the Sun and the global features of the heliosphere are discussed. Both the 11-year sunspot cycle and the 22-year solar magnetic cycle is described, to-

gether with its influences on Fisk-type fields. Finally, the Parker [*Parker*, 1958] and Fisk [*Fisk*, 1996] models are presented after which a brief introduction into cosmic rays and cosmic-ray modulation is given.

Chapter 3 introduces the generalised Fisk field model. The mapping of field lines from the source surface to the photosphere is shown, after which the derivation of the footpoint velocity field and the footpoint trajectories are shown. The resultant field line trajectories are then used to depict the configuration of the magnetic field lines of the generalised Fisk field. Finally, the divergence-free expressions for the field are presented.

The Fisk-Parker hybrid HMF model of *Burger and Hitge* [2004] is discussed in Chapter 4. For the first time, a complete derivation of the hybrid model is given, following an argument showing the magnetic field expressions of the hybrid field are unique. Furthermore, an existing hybrid field with a solar-cycle dependence is described. The existence of a Fisk-type field is considered, as well as what direct or indirect signatures to expect in either magnetic field data or cosmic-ray data.

The magnetic field and neutron monitor data analyses are presented in Chapters 5 and 6, respectively. The azimuth angle of the HMF is introduced and used to compare the predicted magnetic field directions with the observed directions using polar plots and histograms. At the end of Chapter 5, the magnetic field components, B_r and B_ϕ, of the Parker and generalised Fisk models are compared to the components observed by *Ulysses*. Recurrent cosmic-ray intensity variations for both $A > 0$ and $A < 0$ epochs are investigated in Chapter 6, using cosmic-ray data from neutron monitors across the globe. Data before, during, and after solar minimum conditions are analysed. In Chapter 7, a summary and conclusions of the main results are given.

A part of the research from this study has been presented at the *Studentesimposium in die Natuurwetenskappe* annual conference presented by the South African Academy for Natural Sciences in November 2014 and was published in its conference proceedings, see *Steyn and Burger* [2015].

Chapter 2

The Sun and the Heliosphere

2.1 Introduction

Any model for the heliospheric magnetic field (HMF) has as starting point the Sun, where the field originates. This introductory chapter will therefore focus on the Sun and some of its properties relevant to the development of a model of the HMF. It will also cover some heliospheric phenomena that are either of importance for an HMF model, or to give some perspective beyond the scope of the present study.

The basic internal structures of the Sun and its properties will be discussed, after which the solar atmosphere will be reviewed together with its influences on the solar magnetic field. Polar coronal holes (PCH), the darker and cooler areas on the Sun's corona found in the polar regions of the Sun and the source of the fast solar wind, will be reviewed [*Nolte et al.*, 1976]. The heliosphere is the region of influence of the Sun, and its global features and boundaries, such as the termination shock (TS) and bow shock (BS) will be briefly described. The Sun's 22-year solar magnetic cycle and its 11-year sunspot and activity cycle will be discussed, as well as the heliospheric current sheet (HCS).

The differential rotation rate of the surface of the Sun, the photosphere, plays a key role in all Fisk-type fields including the generalised Fisk field model presented in the current study. The HMF and the solar wind (SW) play crucial roles in the transport processes of charged particles in the heliosphere. In this introduction only the model of *Parker* [1958] will be discussed; Fisk-type fields will be the main subject of two of the following chapters. Finally, a brief introduction to cosmic-ray modulation in the heliosphere is presented.

2.2 Basic Structure of the Sun

The large sphere of hot plasma in the centre of our solar system, a yellow dwarf star of G2V spectral type and magnitude 4.8, is called the Sun. It has a mass of 1.99×10^{30} kg, is $\sim 1.5 \times 10^{8}$ km, or 1 astronomical unit (AU) away from the Earth, and has a radius of $r_{\odot} = 6.96 \times 10^{5}$ km [*Mullan*, 2009].

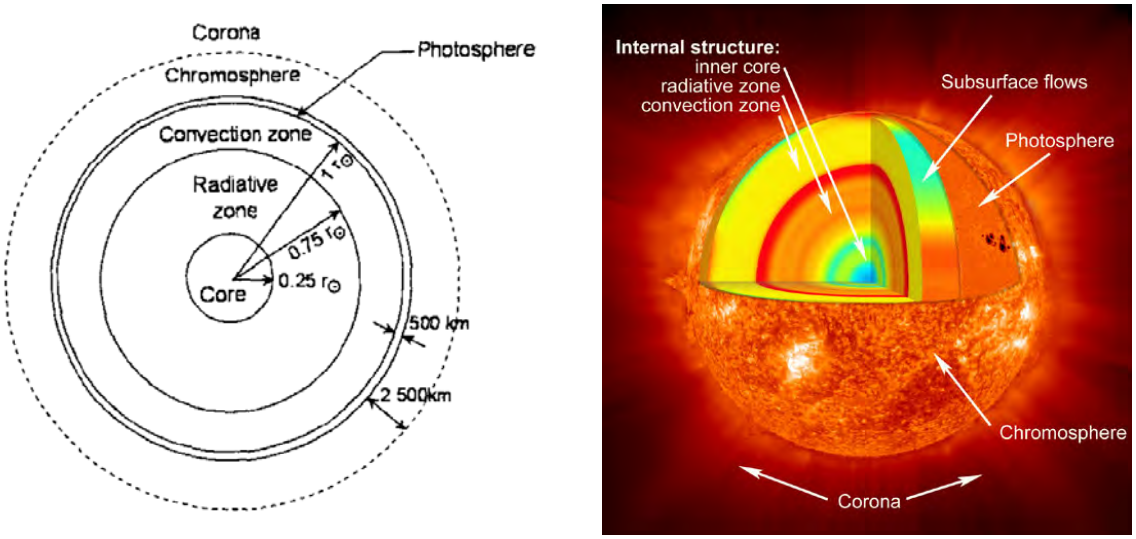

(a) (b)

Figure 2.1: (a): Two-dimensional schematic representing the internal structure of the Sun and its atmosphere (adapted from *Priest et al.* [1995]). (b): Three-dimensional representation of the structures of the Sun (figure from `planetfacts.org`).

Hydrogen and helium are responsible for $\sim 75\%$ and $\sim 24\%$ of its mass, respectively, with the rest attributed to heavier elements such as carbon, nitrogen and oxygen [*Priest et al.*, 1995]. Figure 2.1 shows a two- and three-dimensional representation of the internal and external structures of the Sun. Starting in the centre of Figure 2.1a, the core spans $0.25r_\odot$ and is the largest thermonuclear power plant in our solar system. The extremely hot (1.5×10^7 K) and dense (1.6×10^5 kg·m^{-3}) core prompted a nuclear fusion reaction approximately 4.6 billion years ago.

The internal temperature of the Sun drops significantly with increasing radius. From the core to the top of the radiative zone ($0.75r_\odot$), the temperature drops to 2×10^6 K. As its name suggests, the radiative zone transfers energy primarily through radiation and not thermal convection since the temperature gradient is too small to drive convection. The radiation generated in the core moves slowly through the radiative zone towards the convective zone at $1r_\odot$ due to its very opaque characteristics. Photons undergo many deflections and take $\sim 1.0 \times 10^7$ years to reach the convective zone. The large temperature differences between the internal layers are responsible for the turbulent nature of the convective zone [*Priest et al.*, 1995].

The atmosphere of the Sun consists of three layers namely the photosphere, the chromosphere and the corona, in order of decreasing densities. The photosphere is commonly referred to as the surface of the Sun and is about 500 km thick with a density of 10^{-6} kg·m^{-3}. The surface is not smooth but shows significant granulation, a process by which parcels of plasma rise continuously from the convective zone to the photosphere via a buoyancy force due to the difference in densities. Each granule has an average diameter of 500 km and a lifetime of 5 minutes. Much larger granules, called supergranules, are of the order 3.0×10^4 km in diameter and have a lifespan of a few days [*Gizon et al.*, 2003].

The chromosphere has a density of 10^{-9} kg·m^{-3} and is visible in the red Hα (656.3 nm) emission region. When viewing the chromosphere, sunspots (shown as blemishes in Figure 2.1b) are observed together with the brighter areas around the sunspots, called active regions. When

such an active region brighten very rapidly, a solar flare is released. Darker structures called filaments or prominences are also visible. The corona is the outer most part of the solar atmosphere and has a density of 10^{-13} kg·m^{-3} [*Priest et al.*, 1995]. The particles in the corona are constantly accelerated outwards away from the Sun due to the large pressure gradient between the solar corona and interplanetary space [*Parker*, 1958] and forms the solar wind.

The inclination of the Sun's rotation axis with respect to Earth's orbital plane is 7° and rotates with a sidereal equatorial rotation rate of ~ 25 days.

2.2.1 Polar Coronal Holes

Coronal holes (CHs) are regions of low proton density and temperature on the Sun having magnetic field lines open freely into the heliosphere, and appear dark in soft X-ray images. Fast solar wind streams flow from CHs and aid the propagation of charged particles from the photosphere to the high corona and therefore they are the sources of the fast solar wind [*Nolte et al.*, 1976], [*Woo et al.*, 1999].

Polar coronal holes (PCHs) are CHs in the solar polar regions which expand significantly in latitude from the photosphere to the high corona during solar minimum conditions [*Kopp and Holzer*, 1976]. PCH areas are anti-correlated with the amount of sunspots observed on the photosphere, implying they have a periodicity of ~ 11 years [*Dorotovič*, 1996]. During solar minimum conditions, large PCHs cover the solar poles while non-polar coronal holes are found mainly in the equatorial region. As solar activity increases, the CHs migrate towards the pole of opposite polarity. After a few solar rotations, small PCHs cover the polar cap and replace the old-polarity holes. The old-polarity PCHs disappear gradually or migrate toward the equator. During the rest of the solar cycle, the PCH area gradually increases again [*Bilenko*, 2002]. PCHs plays an important part in the structure of the HMF and is explained in Section 2.7.

2.3 Global Features of the Heliosphere

The word heliosphere is derived from the ancient Greek word for the Sun, $\eta\epsilon\lambda\iota o\zeta$ (helios), and denotes its region of influence. As the name suggests, the heliosphere is the bubble separating the Sun and the solar system from the local interstellar medium (LISM) [*Balogh et al.*, 2007], shown in Figure 2.2. The boundary between the heliosphere and the LISM is defined by the interaction between the solar wind and the LISM. The solar wind is accelerated away from the Sun to becomes supersonic up to where the solar wind pressure is low enough in terms of the LISM pressure to reduce the flow to subsonic. A shock is then created, called the termination shock (TS) (see *Zank* [2015] and references therein). The TS was first crossed by the Voyager 1 spacecraft at 94 AU in December 2004 and then by Voyager 2 in August 2007 at 84 AU (see *Stone et al.* [2005] and *Intriligator et al.* [2008]). The difference in distances confirms the asymmetry of the heliosphere. Past the TS, the ultimate outer boundary between the heliosphere and the LISM is found, called the heliopause (HP).

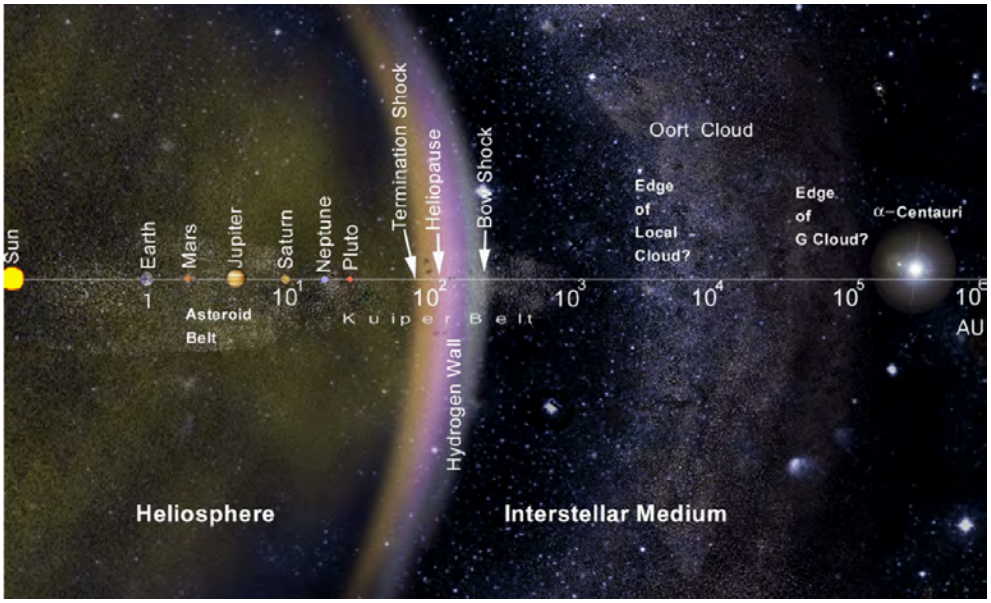

Figure 2.2: Our solar system and its nearby Galactic neighbourhood presented on a logarithmic scale from less than 1 AU to 10^6 AU (adapted from *Balogh et al.* [2007]).

Next, a bow shock (BS) beyond the heliosphere is expected at $\sim$ 250 AU in the direction of travel of Voyager 1, if the interstellar plasma flows supersonically. The existence of the BS is a highly contested issue. The Interstellar Boundary Explorer (IBEX) spacecraft reported that the bow shock does not exist, but more likely a bow wave since the heliosphere is moving too slowly to create a shock [*McComas et al.*, 2012]. On the other hand, *Scherer and Fichtner* [2014] included the He^+ component of the LISM and concluded the BS remains viable. The space between the TS and the HP and the HP and the BS is called the inner and outer heliosheath, respectively. The hydrogen wall is a region of neutral hydrogen and helium on the outside of the HP. The neutral atoms penetrate the heliosphere and can travel close to the Sun where a portion become ionized by the solar wind via charge exchange. The atoms are then picked-up by the solar wind and carried back to the TS where they are energised. At higher energies, these pick-up ions form part of the cosmic-ray population. They also generate turbulence which in turns scatters charged particles.

The size of the heliosphere is not constant and depends on solar activity and the properties of the solar wind [*Balogh and Erdõs*, 2013]. On the solar system scale, the heliosphere is very large, but in astrophysical terms it is dwarfed by the vastness of the universe as indicated by the right side of Figure 2.2. Voyager 1 crossed the HP and left the heliosphere at 121 AU in August of 2012, and is $\sim$ 137 AU ($\sim$ 19 light-hours) from Earth as of 14 October 2016 (see `http://voyager.jpl.nasa.gov/where/`).

2.4 Solar Activity Cycle

When solar activity increases, an increase in extreme ultraviolet and x-ray emissions are observed from the Sun leading to far-reaching effects in the Earth's upper-atmosphere. The subsequent atmospheric heating is responsible for both an increase in temperature and density of

the atmosphere which in turn dramatically influences the lifespan of low-Earth orbit satellites [*Hathaway*, 2015]. Also, during increased solar activity the number of solar flares and coronal mass ejections (CMEs) increase the likelihood of damage to both biological matter and sensitive instruments.

2.4.1 Sunspot Number

Four centuries ago, scientists lookeding at the Sun observed dark spots on the photosphere, now known as sunspots. Sunspots are dark patches on the Sun where intense magnetic fields loop up through the surface from the deep interior [*Hathaway*, 2015]. Heinrich Schwabe discovered during his 18-year observation period of the Sun that the sunspot numbers have a mean periodicity of 11 years [*Schwabe*, 1844]. Upon further investigation, *Maunder* [1904] found that the latitude distribution of the sunspots fluctuate with the same 11-year period. He introduced the "butterfly" diagram shown in the top-panel of Figure 2.3. The 11-year periodicity is seen on the horizontal axis together with a symmetry across the solar equator. The area of the sunspots are colour-coded according to the percentage area covered in a particular latitude region. The bottom panel of Figure 2.3 shows the area of the sunspots according to the percentage covered of the visible hemisphere. After investigating the Zeeman splitting of sunspot spectra,

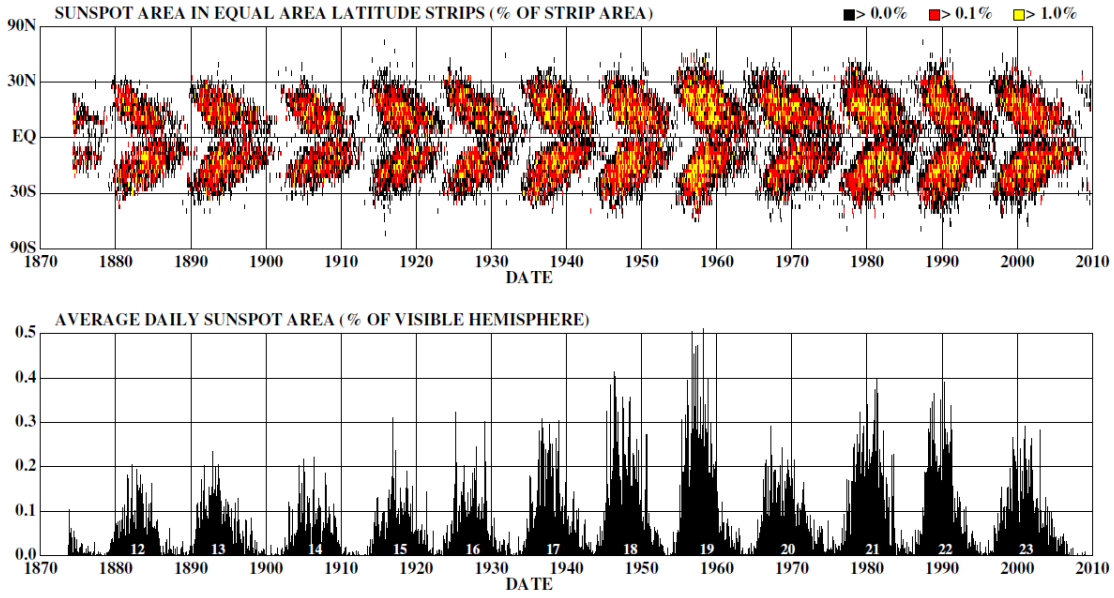

Figure 2.3: Top panel: Butterfly diagram showing the sunspot area as a function of latitude and time. The relative area in equal area latitude strips is illustrated with a colour code. Sunspots form in both hemispheres, starting at about 25° from the equator at the start of a cycle and progress toward the equator. Bottom panel: Average daily sunspot area for each solar rotation since May 1874 as a function of time. Figure adapted from *Hathaway* [2015].

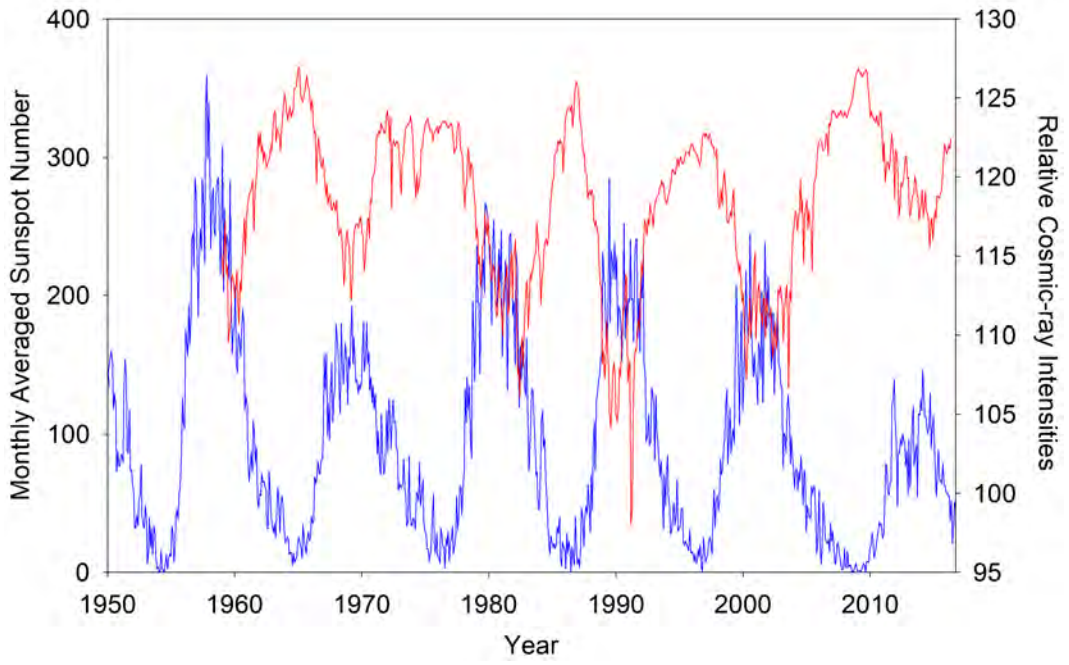

Figure 2.4: Sunspot numbers (blue) with a periodicity of ~ 11 years anti-correlated with the relative cosmic-ray intensities (red) from the Hermanus Neutron Monitor Station in South Africa. Sunspot number data courtesy of Sunspot Index and Long-term Solar Observations (`http://www.sidc.be/silso/home`). Neutron monitor data provided by the Neutron Monitor Database (`www.nmdb.eu`).

Hale [1908] established the fact that the leading spots in a sunspot pair have opposite polarities in opposite hemispheres and alternate between successive sunspot cycles. This lead to the conclusion that the solar magnetic field has a periodicity of ~ 22 years, reversing polarity every ~ 11 years. Figure 2.4 shows the ~ 11-year periodicity found in the sunspot number from January 1950 to May 2016, indicated in blue. The anti-correlated plot shown in red is the relative cosmic-ray intensities throughout the solar activity cycle. The solar activity cycle is also responsible for the periodic modulation of the flux intensities of high energy cosmic rays. The propagation conditions of galactic cosmic rays (GCRs) in the heliosphere are dependent on the variation of solar activity [*Potgieter*, 2013]. During sunspot maximum, the propagation of GCRs from the boundaries to the inner heliosphere involves a greater decrease in intensity [*Balogh et al.*, 2014]. Therefore, the cosmic-ray intensities are in anti-phase with the sunspot number as shown in Figure 2.4. Upon closer inspection, it is apparent that there are differences in the peak intensities of the cosmic rays during alternate 11-year cycles. A flat-top intensity profile is observed between 1970 and 1980, and then again between 1990 and 2000, while the other profiles in-between are more sharply peaked. This phenomena confirms the 22-year Hale cycle when the polarity of the HMF alternates from positive to negative (11 years) and then back to positive again (11 years). When the northern HMF is outward with a positive polar field denoted by $A > 0$ (for historical reasons see e.g. *Jokipii et al.* [1977]), positively charged particles drift inward from the polar regions of the heliosphere to the equatorial plane in the inner heliosphere where the equatorial propagation conditions influence to a lesser extent the access of the particles. When the northern HMF is directed inward with a negative polar field denoted by $A < 0$, positively charged particles enter the inner heliosphere by drifting along

the HCS towards the equatorial regions of the heliosphere, where propagation conditions are controlled by the properties of the structures in the HMF that are co-rotating with the Sun [*Balogh et al.*, 2014].

2.4.2 The Heliospheric Current Sheet

As the magnetic field from coronal holes (Section 2.2.1) is carried out in the solar wind (Section 2.6), the magnetic polarities are separated by the heliospheric current sheet (HCS), a thin current-carrying layer, separating the inward and outward-pointing magnetic field lines [*Balogh et al.*, 2007]. Since the magnetic axis $\vec{M}$ of the Sun is not aligned with the rotational axis $\vec{\Omega}$ of the Sun, the HCS has a warped or wavy structure, referred to as the wavy current sheet (WCS).

The tilt angle α, defined as the angle between $+\vec{M}$ and $+\vec{\Omega}$ during an $A > 0$ epoch and $+\vec{\Omega}$ and $-\vec{M}$ during an $A < 0$ epoch, has an 11-year periodicity connected with the solar activity cycle which in turn gives rise to the 22-year magnetic polarity cycle (see *Balogh et al.* [2014], *Hathaway* [2015], and also *Krüger* [2005], *Van Niekerk* [2000]). Figure 2.5 shows that close to solar minimum conditions (small sunspot number), the HCS is close to the equatorial plane of the Sun (small tilt angle), while the HCS becomes very complex and highly inclined with the solar equator during solar maximum conditions. There are two different ways that Wilcox Solar Observatory calculates the tilt angle.

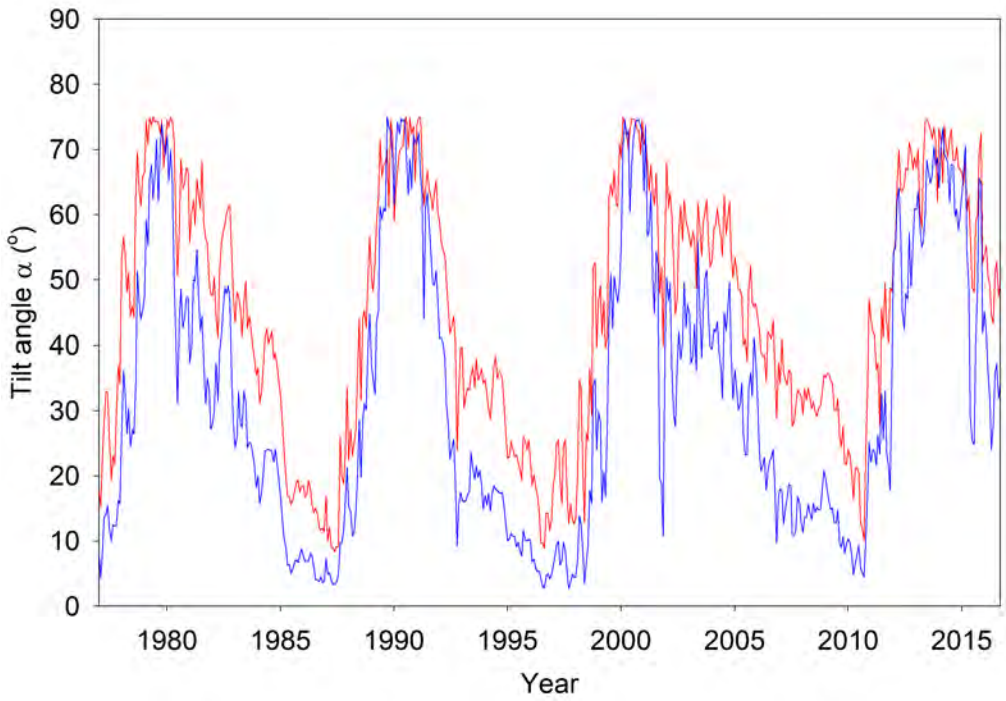

Figure 2.5: Monthly-averaged tilt angles α from January 1977 to July 2016. The red plot is tilt angles calculated with the Classic model, while the blue plot is calculated from the "new" model using a radial boundary condition and a source surface at $r_{SS} = 3.25 r_{\odot}$, courtesy of the Wilcox Solar Observatory (`http://wso.stanford.edu/Tilts.html`).

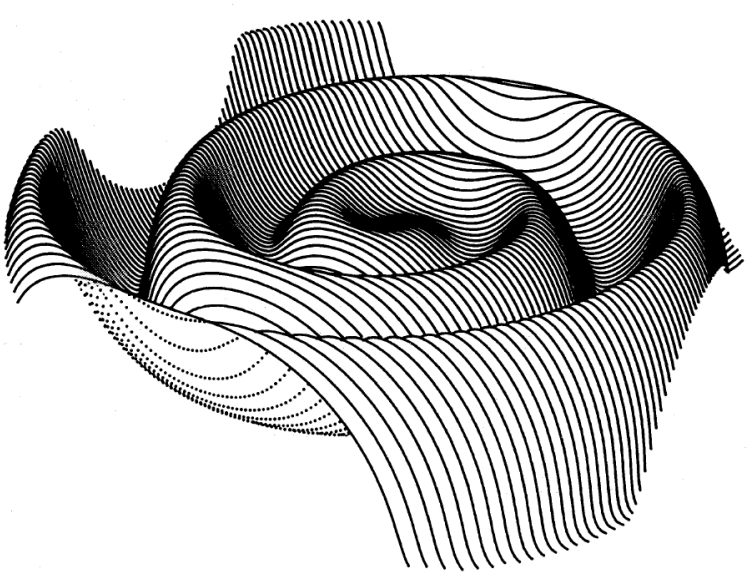

Figure 2.6: Representation of the HCS given by Eq. 2.1 as seen by an observer 30° above the equatotrial plane and 75 AU from the Sun. The tilt angle is chosen to be $\alpha = 15^\circ$ and the solar wind speed 400 km/sec (adapted from *Jokipii and Thomas* [1981]).

The classic model (red line in Figure 2.5) uses a line-of sight boundary condition at the photosphere and includes a significant polar field correction. The so-called new radial model uses a radial boundary condition at the photosphere and requires no polar field correction. The two models track each other, but the radial model typically predicts a smaller tilt angle.

For a constant and radial solar wind speed, the position and the wavy structure of the HCS is numerically modelled by the following equation [*Jokipii and Thomas*, 1981]:

$$\theta' \approx \frac{\pi}{2} + \alpha \sin\left[\phi + \frac{\Omega r}{V}\right], \tag{2.1}$$

where θ, ϕ, and r are spherical polar coordinates relative to the solar rotation axis, and Ω is the angular rotational velocity of the Sun.

2.4.3 Sector Structure of the Heliosphere

Wilcox and Ness [1965] used data from the magnetometer of the *Imp 1* spacecraft to show that a quasi-stationary co-rotating structure is observed in the interplanetary magnetic field. This suggested structure is shown in Figure 2.7 where the plus signs (positive radial component) indicate field lines directed away from the Sun, and minus signs (negative radial component) indicate field lines directed towards the Sun.

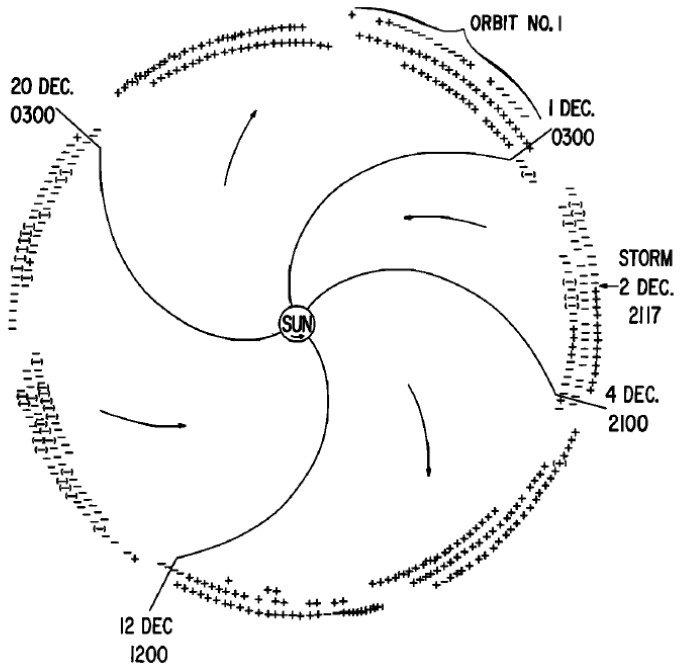

Figure 2.7: Sector structure of the heliosphere as first identified by *Wilcox and Ness* [1965].

2.5 Differential Rotation of the Sun

Snodgrass [1983] investigated the rotation of magnetic features on the solar photosphere, from the equator to very high latitudes, by cross-correlating magnetograms from observations made over successive days during a time period from 1 January 1967 to 29 May 1982, about 15.5 years. He found that the day-to-day rotation of the solar magnetic features to be steady over the entire photosphere, indicating no measurable dependence on the field strength and variation with time. It has been a well-established observation that the rotation of the Sun depends strongly on heliolatitude. Using a standard functional fit, *Snodgrass* [1983] found the rotation profile of the Sun to be:

$$\Omega(\theta) = 2.902 - 0.464\sin^2\theta - 0.328\sin^4\theta \quad \mu\text{rad/sec}, \tag{2.2}$$

where θ is the solar latitude. The first term in Eq. 2.2 indicates the solar equatorial rotation rate, while the coefficients of the second and third terms represent the differential rotation rate of the photosphere. It is more convenient to use spherical coordinates to describe a position on the Sun mathematically. Therefore, when using polar angles, also referred to as co-latitudes, the differential rotation profile of the Sun is given by:

$$\omega(\theta) = 0.464\cos^2\theta + 0.328\cos^4\theta \quad \mu\text{rad/sec}, \tag{2.3}$$

where θ is the polar angle. Figure 2.8 shows the rotation profiles of both Eqs. 2.2 and 2.3 and assumes that they are valid up to the poles, since Snodgrass only investigated up to 73° latitude. The rotation rate of the Sun $\Omega(\theta)$, indicated by the solid red line, increases from 2.1μrad/sec at the poles to about 2.9μrad/sec at the equator, and corresponds to rotation periods of about 34 days and 25 days, indicated by the dashed red line, respectively, in the fixed observer's frame. On the other hand, the profile of the differential rotation rate $\omega(\theta)$ is the inverse and indicated

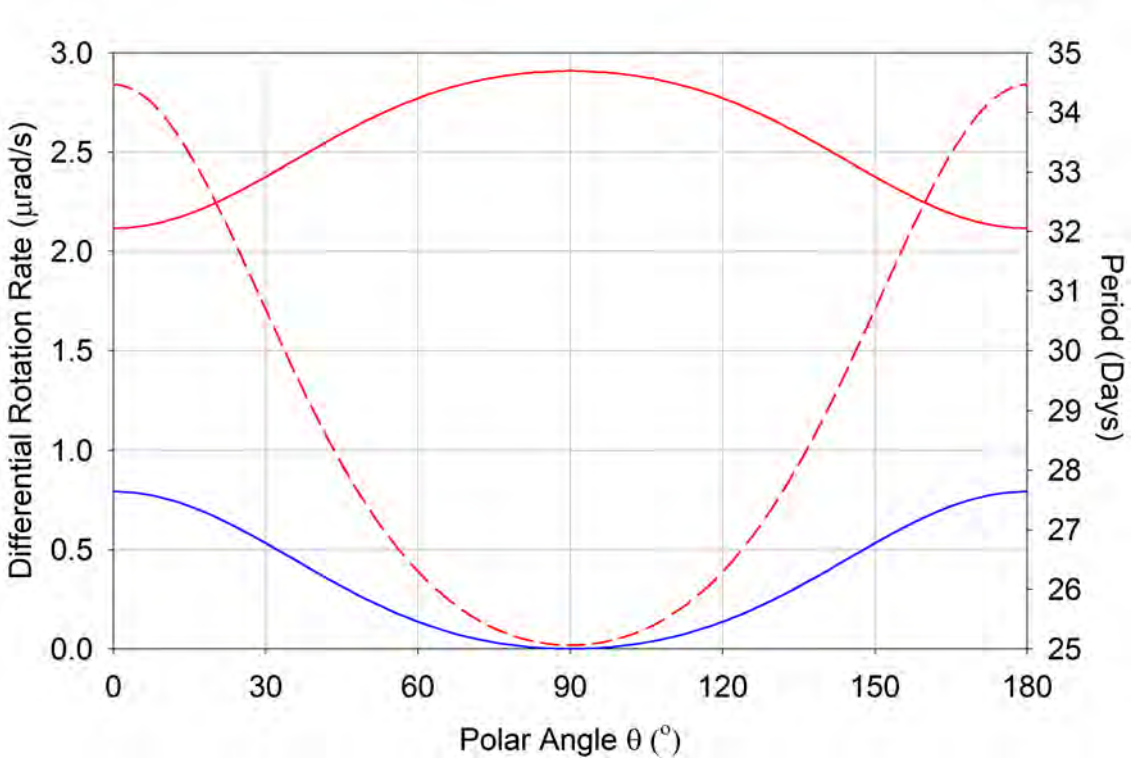

Figure 2.8: Rotation and differential rotation of the photosphere as modelled by *Snodgrass* [1983]. The red and blue plots are the rotation modelled using Eq. 2.2 and Eq. 2.3, respectively, both in μrad/sec and as a function of co-latitude. The dashed red plot shows the period in days of Eq.2.2 as a function of polar angle.

by the solid blue line. The maximum rotation rate of 0.79μrad/sec is attained at the solar poles, while it reduces to zero at the equator, in the co-rotating reference frame. In the Fisk model (section 2.7.3) of the HMF, the differential rotation rate is chosen to be $\omega = \Omega/4$ which equates to 0.725μrad/sec, a differential rotation rate close to the solar equator [*Fisk*, 1996], [*Zurbuchen et al.*, 1997].

The differential rotation rate of the photosphere plays a crucial role in the structure of the generalised Fisk field of Chapter 3.

2.6 The Solar Wind

The concept of the solar wind was first suggested by *Biermann* [1951] (see also *Bierman* [1961]) to explain the behaviour of comet tails that always point directly away from the Sun regardless of the position of the comet. He went on to show the pressure of the solar radiation cannot be solely responsible for this observation and proposed the solar wind always exists and effects the formation of comet tails. *Parker* [1958] coined the term "solar wind" when he showed the atmosphere of the Sun cannot only be in equilibrium and is expanding at supersonic speeds. Through various spacecraft missions, the constituents of the solar wind was established to be mainly ionized hydrogen (electrons and protons) with an 8% component of ionised helium and

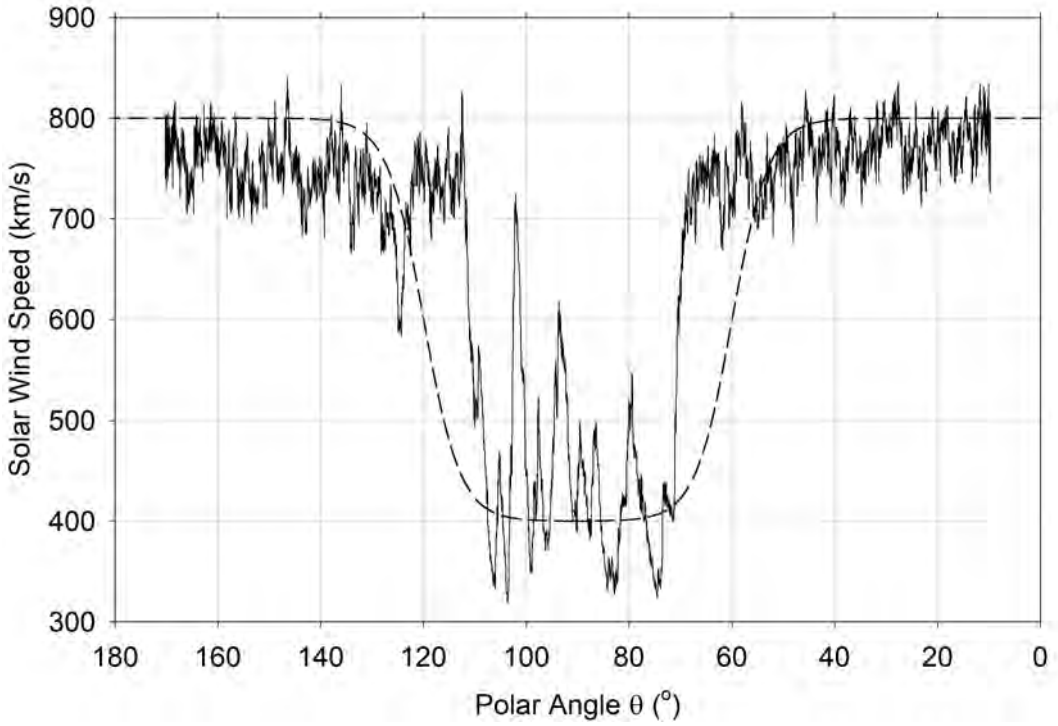

Figure 2.9: Illustration of the latitudinally-dependent nature of the solar wind observed by *Ulysses* during its fast latitude scan (FLS) during $1994/1995$. The modelled solar wind profile from Eq. 2.4 is superimposed on the plot, indicated by a black dashed line.

trace amounts of heavy ions and atomic nuclei such as carbon, nitrogen, oxygen, neon, magnesium, silicon, and iron [*Feldman et al.*, 1998]. Observations established the solar wind speed is not uniform over all latitudes and can be categorised into two classes: the fast solar wind (700 - 800 km/s) emanating from well-developed PCHs, and the slow solar wind (~ 450 km/s) originating near the equatorial region of the Sun during solar minimum conditions [*Zhao and Hundhausen*, 1981]. Figure 2.9 shows hourly-averaged solar wind speed data (solid black line) from the fast latitude scan (FLS) between the southern and the northern solar pole by the *Ulysses* spacecraft [*McComas et al.*, 1998]. Significant variations with heliographic co-latitude was observed. Since the FLS scanned from the southern to the northern solar pole, the horizontal axis runs from 180° to 0° with time running from left to right. *Ulysses* observed a high solar wind speed from 180° to $\sim 115^\circ$ after which it decreased in the equatorial region to ~ 400 km/s. At $\sim 70^\circ$ the solar wind speed picked up again and maintained ~ 800 km/s up to the northern solar pole.

The Sun's magnetic field dominates the outflow of the solar wind close to the Sun. In the equatorial region, where the radial outflow of the solar wind plasma is perpendicular to the solar magnetic field, the solar wind outflow is inhibited. The field lines form loops which begin and end on the photosphere and stretch around the Sun to form the streamer belts, the most plausible source of the slow solar wind. At the higher latitude regions, the solar magnetic field is directed radially outward and assists the coronal outflow into the heliosphere. The magnetic field lines are carried off by the solar wind plasma to form open magnetic field lines.

In order to simulate the solar wind speed profile, *Hattingh* [1998] developed an expression to

model the latitudinally-dependent solar wind speed,

$$V(\theta) = V_0 \left\{ 1.5 \pm 0.5 \tanh \left[8.0(\theta - \frac{\pi}{2} \mp (\alpha + \beta)) \right] \right\}, \tag{2.4}$$

where $V_0 = 400$ km/s, α the tilt angle, and β in association with α is used to determine at which polar angle the solar wind speed starts to increase from 400 km/s to 800 km/s. The top and bottom signs differentiate between the northern and southern hemispheres of the Sun, respectively (also see *He and Schlickeiser* [2015]). Eq. 2.4 is plotted in Figure 2.9 with $\alpha = \beta = \pi/12$ and indicated by the black dashed line.

2.7 The Heliospheric Magnetic Field

The solar corona is a highly conductive plasma where temperatures increase with height from the corona. The increasing temperatures cause a pressure-driven solar wind outflow [*Parker*, 1958] from the corona and after a few solar radii the flow momentum is comparable to the magnetic pressure [*Owens and Forsyth*, 2013]. Therefore, the solar wind is responsible for the dragged-out coronal magnetic field (CMF) forming the heliospheric magnetic field (HMF), or formally known as the interplanetary magnetic field (IMF). The HMF is a key constituent of the heliosphere.

2.7.1 Potential Field Source Surface

The potential field source surface (PFSS) model describes the magnetic field from the photopshere to the source surface in the mid-corona (see *Schatten et al.* [1969], *Altschuler and Newkirk* [1969]). The PFSS model was developed by *Schatten et al.* [1969] to connect the potential (dipolar) field model near the photopshere to the newly proposed HMF model of *Parker* [1958]. While the CMF is current-free, the HMF is completely governed by currents. Therefore, a virtual surface, called the source surface (SS), is envisaged to separate the CMF from the HMF. Figure 2.10 shows the location of the SS in terms of the Sun and the magnetic field lines. To fit magnetic field and solar wind data from spacecraft, the radius of the SS is typically chosen to be 2 - $2.5 R_\odot$, but it can change depending on the features that are to be described, e.g. CMF and HMF magnitudes and coronal hole sizes and locations (see *Wang and Sheeley* [1992], *Hoeksema et al.* [1996], *Balogh et al.* [1999b]). The HMF model of *Fisk* [1996] only requires a SS radius well below the Alfvén radius of $\sim 10 R_\odot$. Although the PFSS model is the most widely used photospheric extrapolation technique, it does not provide perfect agreement with *in situ* spacecraft observations of the HMF intensity or sector structure.

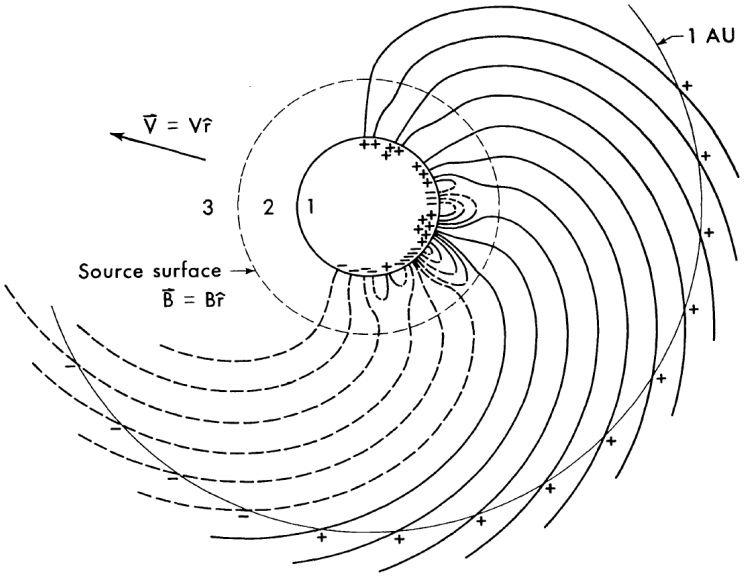

Figure 2.10: Graphical representation of the PFSS model. The CMF is measured in Region 1 while closed filed lines are found in Region 2. Currents flowing near the SS eliminate the transverse components of the magnetic field, and the solar wind extends the SS magnetic field into the heliosphere. The magnetic field is then observed by spacecraft at 1 AU. Figure adapted from *Schatten et al.* [1969].

2.7.2 The Parker Heliospheric Magnetic Field

The Parker model for the HMF was introduced by E.N. Parker in 1958. When he derived the field, he had a specific theoretical mindset where he avoided electric fields $\vec{E}$ and currents $\vec{j}$, and only worked with the plasma velocity $\vec{V}$ and the magnetic field $\vec{B}$ [*Balogh et al.*, 2007]. The photospheric footpoints of the magnetic field lines are assumed to be anchored to the photosphere and hence rotate with the Sun. It is customary to treat the magnetic field as "frozen-into" the highly-conductive solar wind plasma, implying $\vec{V}$ and $\vec{B}$ are parallel in the frame co-rotating with the Sun. Under these conditions, the HMF is wound into a Archimedean spiral in the solar equatorial plane (see *Zurbuchen* [2007], *Balogh and Erdõs* [2013]). Figure 2.11a shows the spiral structure of the Parker model at three different latitudes. The yellow field line is in the equatorial plane, while the blue and green plots show field lines starting at $\theta = 45°$ and $\theta = 5°$ on the photosphere, respectively.

Figure 2.11b shows a schematic of what the steady-state Parker model looks like in the ecliptic plane with the Sun in the center of the figure, rotating in an anti-clockwise direction. Inside the region closest to the Sun, the magnetic field lines undergo super-radial expansion where the magnetic field dominates over the plasma flow. The source surface is indicated by the solid black circle after the Sun where the field becomes purely radial. Inside the heliosphere, the spiral geometry becomes evident due to the azimuthal component of the magnetic field. The HCS is indicated by the green dashed lines and separates the opposite polarities (indicated in red and blue) of the magnetic field.

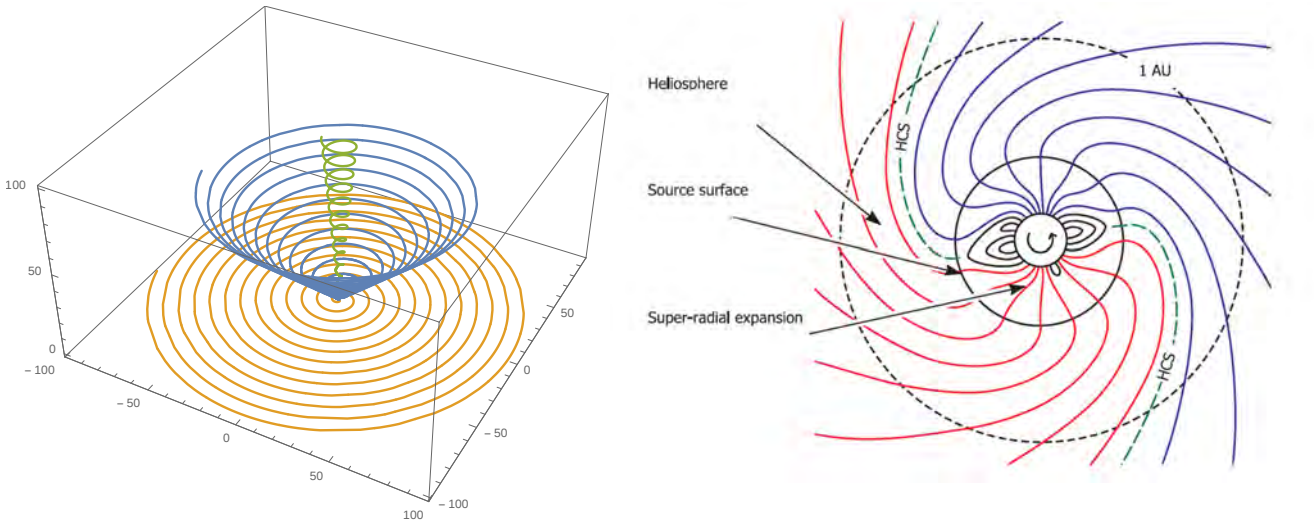

(a) (b)

Figure 2.11: Left: Parker magnetic field lines at three different latitides. See text for details. Right: Steady-state solar magnetic field in the ecliptic plane. Figure adapted from *Owens and Forsyth* [2013].

For a complete derivation of the Parker field equations, see *Krüger* [2005] and *Owens and Forsyth* [2013]. For completeness sake, the key features of the derivation is discussed here. Concerning the geometry, it is assumed that the rotational axis $\vec{\Omega}$ is aligned with the magnetic axis $\vec{M}$, so that heliographic polar coordinates can be used. Furthermore, the Parker field equations are based on three assumptions. Firstly, in a constant solar wind flow, magnetic flux conservation requires the radial component of the HMF to fall off as the inverse square of the heliocentric distance. This assumption is satisfied by Eq. 2.5 in heliocentric spherical coordinates (r,θ,ϕ) where $B_{r,0}$ is the magnetic field magnitude at the Earth and r_0 is the heliocentric distance of the Earth, and r any radial distance:

$$B_r = B_{r,0}\frac{r_0^2}{r^2}. \tag{2.5}$$

Secondly, it is assumed that the solar wind flow is exactly radial with no meridional or azimuthal component,

$$B_\theta = 0. \tag{2.6}$$

Thirdly, in the frame of reference that co-rotates with the Sun, the solar wind plasma and frozen-in field line are parallel, leading to $B_\phi/B_r = V_\phi/V_r = -\Omega r \sin\theta/V_r$ where V_r and V_ϕ are the constant radial solar wind speed and the azimuthal solar wind speed, respectively, resulting from the reference frame rotating at an angular speed of Ω, the mean solar rotation speed. From the relationship between the radial and azimuthal components mentioned above, the azimuthal component of the Parker field is:

$$B_\phi = -B_{\mathrm{r},0}\frac{r_0^2}{r^2}\frac{\Omega}{V_r} r \sin\theta. \tag{2.7}$$

Several different modifications to the standard Parker HMF model have been proposed in the past. Although the standard Parker field equations are still used widely today, observations over the solar poles have suggested that the physical HMF deviates significantly from what

the Parker model predicts [*Forsyth et al.*, 1996]. For an in-depth discussion on several of the modifications, see *Langer* [2004] and *Krüger* [2005]. These modifications include the Jokipii-Kóta modification [*Jokipii and Kota*, 1989], the Moraal modification [*Moraal*, 1990], the Smith-Bieber modification [*Smith and Bieber*, 1991], and the Giacalone modification [*Giacalone*, 1999].

2.7.3 The Fisk Heliospheric Magnetic Field

The Fisk model of the HMF was born from an unexplainable observation made by the *Ulysses* spacecraft mission when it scanned the solar poles during solar minimum conditions. 26-day periodic variations of particle intensities were observed up to the highest latitudes ($\sim 80^\circ$ S) [*Simpson et al.*, 1995], [*Roelof et al.*, 1997]. These periodic variations were only expected in the equatorial plane due to co-rotating interaction regions (CIRs), compressive interaction regions that form when solar wind flows of different speeds become radially aligned [*Gosling and Pizzo*, 1999], [*Balogh et al.*, 2007]. The particles observed at high latitudes could have originated in CIRs and propagated to higher latitudes by some unknown mechanism. *Fisk* [1996] suggested magnetic field lines could be responsible for connecting the lower latitudes at the Sun with higher latitudes further away where the accelerated particles in CIRs follow the field lines into the heliosphere. Therefore, the field lines of the Fisk field exhibit large excursions in heliographic latitude. Variants of this field will be the main subject in two of the following chapters.

2.8 The *Ulysses* Spacecraft Mission

The *Ulysses* spacecraft mission was a collaboration between the European Space Agency (ESA) and the National Aeronautics Space Administration (NASA) intended to increase the knowledge base of natural processes occurring in the inner heliosphere by *in-situ* measurements over the widest possible range of solar latitudes [*Balogh et al.*, 2001]. The mission was scheduled for launch in 1982, but due to financial constrains it was only launched on 6 October 1990. It continued operation far past its expected lifespan and was only decommissioned on 30 June, 2009. The main objectives of the mission included determining the global three-dimensional properties of the heliospheric magnetic field and the solar wind, studying the origin of the solar wind by measuring the composition of the solar-wind plasma at different heliographic latitudes, and increasing knowledge of discontinuities in the solar wind by sampling plasma conditions away from the ecliptic plane [*Balogh et al.*, 2001]. In contrast, several spacecraft have explored the ecliptic region of the heliosphere in the past, e.g. *Pioneer*, *Voyager* 1, and *Helios* (see *Thomas and Smith* [1980], *Burlaga et al.* [1982], *Burlaga and Ness* [1993], and *Bruno and Bavassano* [1997]). The *Ulysses* mission recorded observations up to 80.2° in heliographic latitude for both the southern and northern solar hemispheres.

Figure 2.12 shows the first orbit of Ulysses from a 15° above the ecliptic perspective during approaching solar minimum conditions. After launch, *Ulysses* was put on a near in-ecliptic flight trajectory towards Jupiter. In February 1992, a gravity-assist manoeuvre was initialised to force *Ulysses* into a highly inclined trajectory with respect to the ecliptic towards the Sun. There was no *a priori* scientific reason to explore a given solar hemisphere first, therefore the

slight south of the solar equator position of Jupiter was exploited to send *Ulysses* to proceed with a southern pass first. The orbital period was 6.1 years while its closets approach to the Sun was 1.3 astronomical units (AU) to protect the instruments from thermal damage. Figure 2.13 shows the second orbit of *Ulysses* from a perspective showing its 80° inclination.

Hourly averaged data from the *Ulysses* mission are available at `http://omniweb.gsfc.nasa.gov/coho/form/ulysses.html` in downloadable ASCII file format. These data include, but is not limited to, the heliocentric distance from the Sun in AU, the heliographical inertial latitude of the spacecraft, the solar wind speed, and the magnetic field data in RTN (radial-tangential-normal) coordinates. This coordinate systems is defined by an *R*-axis pointing radially outward from the Sun, a *T*-axis parallel to the solar equatorial plane and positive in the direction of solar rotation, and an *N*-axis which is the vector normal to the *RT*-plane [*Forsyth et al.*, 1996]. Data from the Ulysses mission are used in the current study.

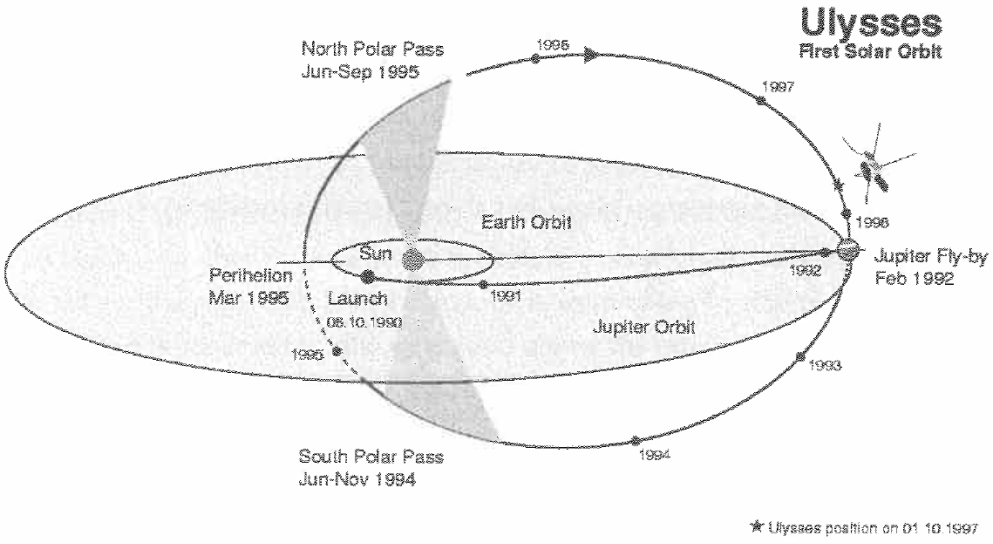

Figure 2.12: Illustration of the first orbit of *Ulysses* around the Sun from a 15° above the ecliptic plane perspective [*Balogh et al.*, 2001].

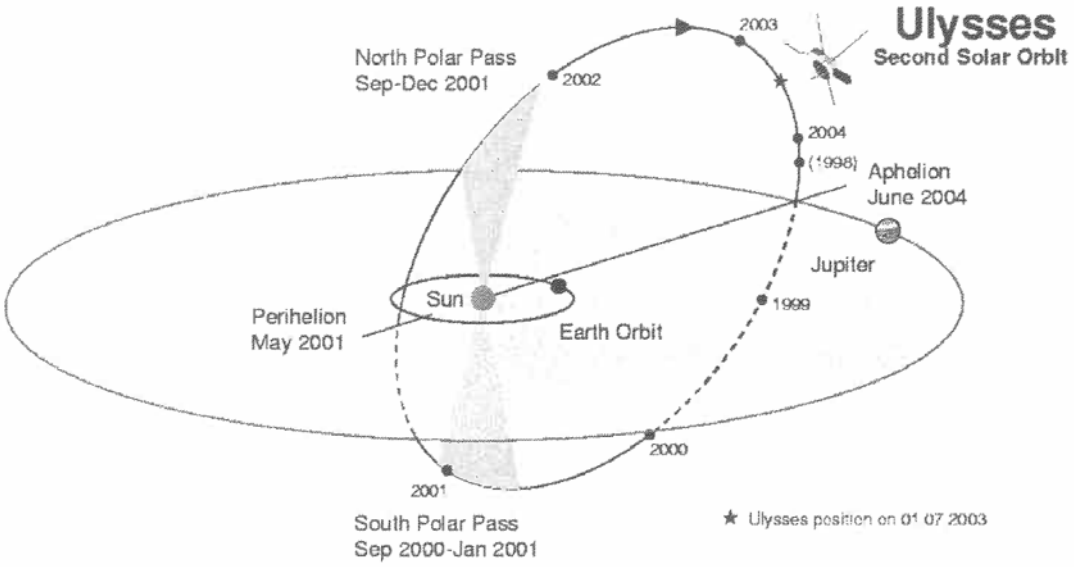

Figure 2.13: Illustration of the second orbit of *Ulysses* from a perspective showing the $80°$ inclination of the orbit with respect to the ecliptic plane [*Balogh et al.*, 2001].

2.9 Cosmic Rays

Cosmic rays (CRs) are highly energetic charged particles that propagate throughout the galaxy (and heliosphere) after being accelerated to very high velocities. CRs have energies in the range of 1 MeV to up to 10^{21} eV which exceed the energy of an average particle in the heliosphere (~ 100 keV) by several orders of magnitude. Its composition is comprised of 99% nuclei deprived of their electron shells and the remaining 1% are mostly beta particles. About 87% of the nuclei are protons, 12% helium nuclei, and finally 1% electrons and hints of heavier nuclei [*Simpson*, 1992].

Cosmic rays are subdivided into galactic cosmic rays (GCRs), solar energetic particles (SEPs), anomalous cosmic rays (ACRs), and Jovian electrons. Galactic cosmic rays have their origins inside our local galaxy and are produced in supernova explosions, supernova remnants, and in the magnetospheres of pulsars. During the early 20th century, scientist provided evidence with a whole range of experiments that the cosmic radiation reaching the top of Earth's atmosphere generated nuclear interactions (see *Simpson* [2000] and references therein). Later on, the observation of disintegration products were confirmed using Ilford emulsions and cloud chambers. By 1946 the atmospheric cascading effect, illustrated in Figure 2.14, was confirmed. See *Ferreira* [2002], *Langer* [2004], and *Strauss* [2010] for further discussions on Jovian electrons, ACRs, and SEPs.

When a GCR (primary cosmic ray) encounter the Earth's atmosphere, it interacts with an air molecule and splits the molecule into smaller high energy components (secondary cosmic rays), as shown in Figure 2.14. The secondary cosmic rays in turn collide with more air molecules and the process continues up until such time the nucleonic components reach the surface of the Earth to be detected by neutron monitors.

Neutron monitors provide an effective way of monitoring the primary cosmic-ray flux (see *Simpson* [1957] and *Stoker et al.* [2000] for historical overviews and improvements of neutron

monitors). Neutron monitors consists of four main components, namely the reflector, producer, moderator, and proportional counter. The reflector is the outer shell of the monitor made of polyethylene which shields the inside of non-cosmic, low-energy neutrons. The producer is made of lead and is responsible for the ~ 10 lower energy neutrons produced inside the monitor when fast neutrons penetrate the reflector and interact with the lead. This amplifies the cosmic-ray signal. The moderator slows the neutrons captured inside the producer down in order for them to be detected. After the neutrons undergo all the aforementioned processes, they encounter a nucleus and disintegrates it to produce charged energetic particles that ionizes a gas (beryllium or helium) in a tube producing an electrical signal which is then quantified to a neutron counts-per-second rate.

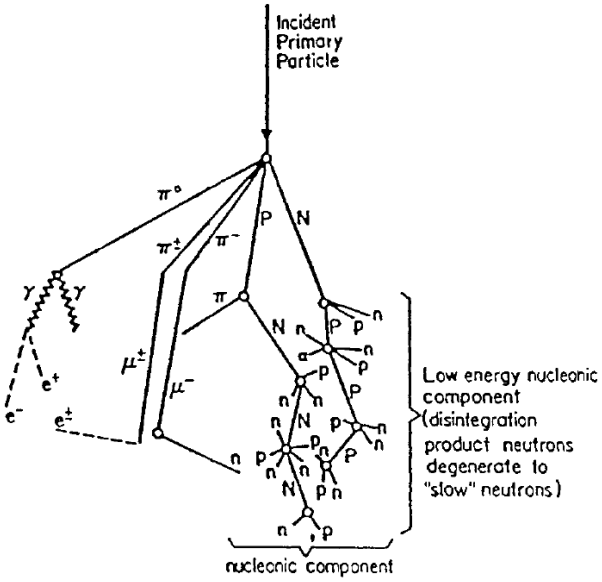

Figure 2.14: Illustration of the typical development of the secondary radiations within the atmosphere arising from the incident primary particle. Figure adapted from *Simpson* [2000].

2.9.1 Solar Modulation of Cosmic Rays

Cosmic rays (CRs) are subject to physical processes that change their distribution and intensity in position, energy and time when they enter the heliosphere and encounter the turbulent heliospheric magnetic field embedded in the outflowing solar wind. During the convection process, the solar wind expands radially outward and cools down adiabatically, resulting in the deceleration of CRs interacting with magnetic scattering centres embedded in the plasma. Due to such turbulent irregularities in the magnetic field the particles are scattered, effectively undergoing a diffusive random walk along and across the magnetic field lines from the outer boundary of the heliosphere with its higher intensity, to the inside of the heliosphere. Also, due to gradients in the magnitude of the magnetic field, the curvature of the field or any abrupt changes in the

field direction cause the particles to experience drift motions.

Parker [1965] combined these major CR modulation processes into one transport equation (TPE):

$$\frac{\partial f}{\partial t} = \nabla \cdot (\vec{K} \cdot \nabla f - \vec{V} f) + \frac{1}{3}(\nabla \cdot \vec{V}) \frac{\partial}{\partial \ln P}(f) + Q. \tag{2.8}$$

Here $f(\vec{r}, p, t)$ is the omnidirectional CR distribution function, with $\vec{r}$ the position and p the momentum of the particle at a time t. $\vec{V}$ is the solar wind velocity in the co-rotating frame, P the rigidity, $\vec{K}$ the diffusion tensor, and Q a source function describing CR sources in the heliosphere. The first term of Eq. 2.8 describes particle diffusion and drift, the second term convection, and finally the third term the adiabatic energy changes.

Variants of this TPE has been used in various studies (e.g. *Kota and Jokipii* [2003], *Krüger* [2005], *Engelbrecht* [2008], *Burger et al.* [2008], *Sternal et al.* [2011]) to determine how a Fisk-type field could affect the modulation of cosmic rays. The results, in a nutshell, suggest that the field should have little effect on large-scale modulation (and thus little effect on energy spectra), but that its effect should be seen in recurrent cosmic-ray variations.

Chapter 3

A Generalised Fisk-Type Heliospheric Magnetic Field

3.1 Introduction

The Parker model [*Parker*, 1958] of the HMF discussed in Chapter 2, is preferred by the cosmic-ray modulation research community due to its uncomplicated Archimedean spiral structure and the observational evidence supporting it (see e.g. the review by *Ness and Burlaga* [2001]). Although the Parker field is easy to implement in a numerical modulation code, the effect of differential rotation in the photosphere (see Chapter 2) is implemented at a much more fundamental - and likely more realistic - level in the the Fisk field [*Fisk*, 1996]. In this chapter a new, generalised Fisk-type field is presented, while in Chapter 4, the published Fisk-Parker hybrid field of Burger and co-workers is revisited.

Differential rotation can be included in Parker-type models, i.e. models without a meridional component, but with the implicit assumption that the differential rotation of the photosphere maps out radially to the source surface so that the footpoints of the magnetic field lines remain at constant heliographic latitudes. Fisk-type fields assume that field lines expand superradially from the photosphere to the source surface, thus introducing a meridional component. All published models to date assume the differential rotation rate to be equal to a constant fraction of the equatorial rotation rate, typically $\omega = \Omega/4$ (see [*Fisk*, 1996],[*Burger et al.*, 2008]). *Snodgrass* [1983] showed experimentally the differential rotation rate of the photosphere to be latitudinally dependent, with a sidereal period of about 35 days and 25 days expected at the poles and equator, respectively.

In this chapter the assumption of a constant differential rotation rate is relaxed, and a generalised Fisk-type model is described that takes into account the latitudinal dependence of the differential rotation rate on the photosphere. The consequence will be that the differential rotation rate on the source surface, beyond which the radial solar wind drags the magnetic field into the heliosphere, will depend on heliographic latitude and longitude. Transformations which uniquely map magnetic field lines from the source surface back to the photosphere are shown. In previous Fisk-type models it was only necessary to map fields outward from the photo-

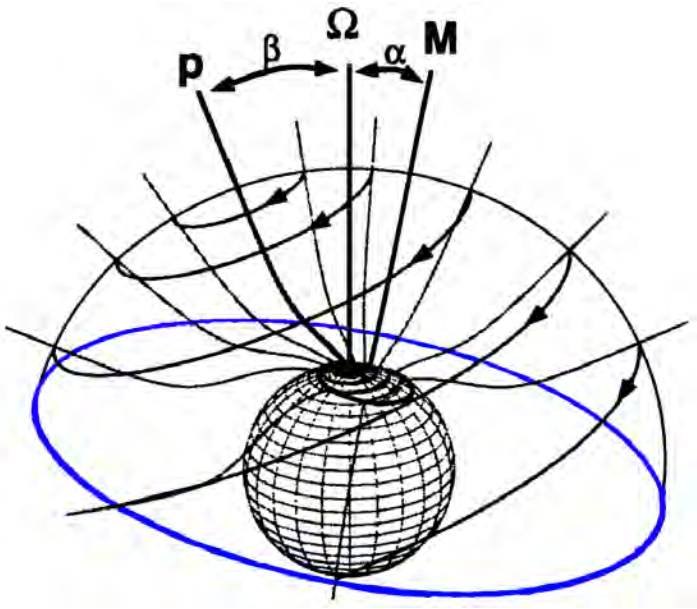

Figure 3.1: Illustration of the supper-radial expansion of the magnetic field lines from a PCH in the northern hemisphere in the co-rotating frame as modelled by the generalised Fisk field. Note that the three axes shown are assumed to be co-planar. Figure adapted form *Zurbuchen et al.* [1997].

sphere to the source surface. The required divergence-free nature of the generalised Fisk field and the velocity field of the magnetic field footpoints on the source surface is verified explicitly.

3.2 Structure of the Generalised Fisk HMF

The global structure of the generalised Fisk field is based on the original model of *Fisk* [1996]. Figure 3.1 shows the rotational axis $\vec{\Omega}$, the magnetic axis $\vec{M}$, and the virtual $\vec{p}$-axis. The magnetic axis is off-set from the rotational axis by an angle α and the $\vec{p}$-axis is off-set by an angle β, also referred to as the Fisk angle. The $\vec{p}$-axis is defined by the magnetic field line originating from the solar pole and expanding super-radially to the source surface. Since no differential rotation is experienced at the pole, this axis intersects the source surface at a fixed location in the co-rotating system. The inner and outer spheres represent the photosphere and the solar wind source surface, respectively. A key assumption is that the generalised Fisk field is symmetrical about the heliomagnetic equator, and that the trajectories do not cross the heliomagnetic equator. Therefore, only the northern hemisphere is shown. It is further assumed that the footpoint trajectories are full or partial circles centered on the $\vec{p}$-axis, as is the case for the original Fisk field [*Fisk*, 1996].

A PCH symmetric about the magnetic axis $\vec{M}$ and rotating at the equatorial rotation rate is shown. The magnetic field lines inside the PCH are open and expand super-radially and symmetrically about $\vec{M}$ from the photosphere out to the source surface. The source surface footpoints trace out circular trajectories symmetric about the $\vec{p}$-axis. The boundary of the PCH maps to the solid blue line on the source surface. When the magnetic field footpoints cross the blue boundary in Figure 3.1, they move by magnetic reconnection (see, e.g., *Fisk et al.* [1999a]).

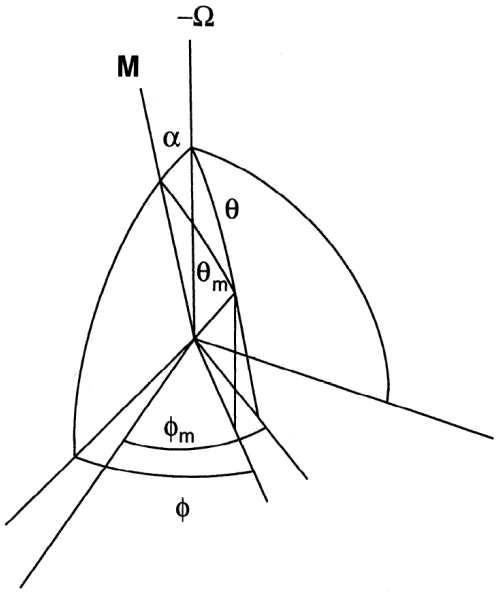

Figure 3.2: Heliographic and -magnetic coordinate systems used to derive the footpoint motion equations. The heliographic coordinate system is centred on the southern heliographic pole, therefore the negative $\vec{\Omega}$. Also note the parallel y- and y_m axes (figure adapted from *Fisk* [1996]).

In this so-called return region, magnetic flux is conserved since while field lines leave the surface where coherent footpoint motion occurs in one hemisphere, others enter this region in the opposite hemisphere.

To explain the consequence, consider a stationary observer scanning the source surface in heliographic longitude as the Sun and source surface rotates about $\vec{\Omega}$. The observer will sample magnetic field lines on the source surface originating from different latitudes and longitudes on the photosphere. In other words, for every degree that the Sun and source surface rotate, the observer samples a different source surface footpoint trajectory which implies sampling different footpoint trajectories on the photosphere.

3.3 Mapping Field Lines From Source Surface to Photosphere

Fisk [1996] derived the equations for mapping magnetic field lines from the photosphere to the source surface (see also *Van Niekerk* [2000]). The generalised Fisk field requires that field lines at a given heliographic position on the source surface be traced back to their heliographic origin on the photosphere in order to determine their original differential rate. In the first part of this section, the mapping from the photosphere to the source surface is repeated, using the current nomenclature (see Table 3.1). The mapping in the opposite direction is then performed. Figure 3.2 shows a reference frame centred on the south heliographic pole co-rotating with the equatorial rotation rate Ω of the Sun. Two spherical coordinate systems are defined, namely heliographic and heliomagnetic. The heliographic coordinate system is centred on the rotation axis of the Sun, while the heliomagnetic coordinate system is centred on the magnetic axis of the Sun which in the co-rotating frame is assumed to be fixed and at an angle α relative to the

south heliographic pole. In heliographic coordinates, points on the photosphere are defined by a polar angle θ, azimuthal angle ϕ and by θ_m and ϕ_m in magnetic coordinates.

The footpoints on the photosphere follow circular trajectories about the rotation axis, defined in heliographic coordinates by

$$\theta = \text{constant} \qquad \text{and} \qquad \phi = \omega t + \phi_0, \tag{3.1}$$

where ϕ_0 is the azimuthal angle at $t = 0$, and ω the angular differential rotation rate defined by *Snodgrass* [1983] in co-latitude as

$$\omega(\theta) = 0.464 \times 10^{-6} \cos^2\theta + 0.328 \times 10^{-6} \cos^4\theta \quad \text{rad/s}. \tag{3.2}$$

Following a field line originating at the photosphere from a position specified in heliographic coordinates, to where it encounters the source surface, with its position again specified in heliographic coordinates, is done in three steps:

- Firstly, a rotation transformation about the angle α from heliographic to heliomagnetic coordinates is performed. This describes the footpoint motion of field lines at the surface of the Sun. Since this is a rotation transformation only the heliocentric radial distance remain unchanged.
- Secondly, the field lines are then assumed to expand super-radially from the photosphere to the source surface subject to Gauss's law. The heliomagnetic longitude to which the field lines expand during this phase is assumed to remain the same.
- Thirdly, another rotation transformation about α from heliomagnetic back to heliographic coordinates is performed to produce the footpoint motion of field lines on the solar wind source surface.

These transformations uniquely identify the path of a magnetic field line originating on the photosphere, to the source surface. The generalised Fisk field assumes a θ and ϕ dependence in heliographic coordinates on the source surface in its expression for the angular differential rotation rate. Now, transformations will be presented uniquely identifying the path of a magnetic field line from the solar wind source surface back to the photosphere. With these transformations, heliographic coordinates on the source surface can be compared to heliographic coordinates on the photosphere. Also, the heliographic magnetic field lines sampled by *Ulysses* originating from the source surface, will now be able to be uniquely placed at their respective positions on the photosphere. The process again involves three steps:

- A rotation transformation from heliographic coordinates on the solar wind source surface to heliomagnetic coordinates on the solar wind source surface is performed about the angle α.
- The field lines are then assumed to uniquely map down to the photosphere in heliomagnetic co-latitude. Again, the heliomagnetic longitude remains the same.

	Heliomagnetic Source Surface	Heliographic Source Surface	Heliomagnetic Photosphere	Heliographic Photosphere
Polar Angle θ	θ^{ss}_{hm}	θ^{ss}_{hg}	θ^{ph}_{hm}	θ^{ph}_{hg}
Azimuthal Angle ϕ	ϕ^{ss}_{hm}	ϕ^{ss}_{hg}	ϕ^{ph}_{hm}	ϕ^{ph}_{hg}

Table 3.1: Nomenclature to differentiate between heliographic and heliomagnetic coordinates on both the source surface and photosphere.

- Finally, a rotation transformation from heliomagnetic coordinates on the photosphere to heliographic coordinates on the photosphere is performed about the angle α.

Now consider the first step. The matrix of Eq. 3.3 shows a rotation about the angle α in heliomagnetic coordinates on the source surface.

$$\begin{bmatrix} x^{ss}_{hm} \\ y^{ss}_{hm} \\ z^{ss}_{hm} \end{bmatrix} = \begin{bmatrix} \cos\alpha & 0 & -\sin\alpha \\ 0 & 1 & 0 \\ \sin\alpha & 0 & \cos\alpha \end{bmatrix} \begin{bmatrix} x^{ss}_{hg} \\ y^{ss}_{hg} \\ z^{ss}_{hg} \end{bmatrix} \tag{3.3}$$

Expanding Eq.3.3 by multiplying the terms out leads to:

$$\begin{aligned} x^{ss}_{hm} &= x^{ss}_{hg}\cos\alpha - z^{ss}_{hg}\sin\alpha \\ y^{ss}_{hm} &= y^{ss}_{hg} \\ z^{ss}_{hm} &= x^{ss}_{hg}\sin\alpha + z^{ss}_{hg}\cos\alpha \end{aligned} \tag{3.4}$$

Eq. 3.4 can be recast when making use of the following standard transformations between Cartesian and spherical coordinates:

$$\begin{aligned} x^{ss}_{hm} &= r\sin\theta^{ss}_{hm}\cos\phi^{ss}_{hm} \quad & x^{ss}_{hg} &= r\sin\theta^{ss}_{hg}\cos\phi^{ss}_{hg} \\ y^{ss}_{hm} &= r\sin\theta^{ss}_{hm}\sin\phi^{ss}_{hm} \quad & y^{ss}_{hg} &= r\sin\theta^{ss}_{hg}\sin\phi^{ss}_{hg} \\ z^{ss}_{hm} &= r\cos\theta^{ss}_{hm} & z^{ss}_{hg} &= r\cos\theta^{ss}_{hg} \end{aligned} \tag{3.5}$$

with $r = \sqrt{\left(x^{ss}_{hm}\right)^2 + \left(y^{ss}_{hm}\right)^2 + \left(z^{ss}_{hm}\right)^2} = \sqrt{\left(x^{ss}_{hg}\right)^2 + \left(y^{ss}_{hg}\right)^2 + \left(z^{ss}_{hg}\right)^2}$, and accordingly Eq. 3.4 becomes:

$$\begin{aligned} \cos\theta^{ss}_{hm} &= \cos\theta^{ss}_{hg}\cos\alpha + \sin\theta^{ss}_{hg}\cos\phi^{ss}_{hg}\sin\alpha \\ \sin\theta^{ss}_{hm}\sin\phi^{ss}_{hm} &= \sin\theta^{ss}_{hg}\sin\phi^{ss}_{hg} \\ \cos\phi^{ss}_{hm} &= \frac{\sin\theta^{ss}_{hg}\cos\phi^{ss}_{hg}\cos\alpha - \cos\theta^{ss}_{hg}\sin\alpha}{\sin\theta^{ss}_{hm}}, (\theta^{ss}_{hm} \neq 0) \end{aligned} \tag{3.6}$$

This expression is in agreement with the results of *Fisk* [1996] and *Van Niekerk* [2000], but see the remark in the latter regarding the typographical error in equation (4) of *Fisk* [1996].

Moving into the next step, the task is to calculate how the field lines will map from the photosphere to the source surface.

The technique used by [*Van Niekerk*, 2000] and *Krüger* [2005] includes ensuring the HMF satisfies Maxwell's equation $\nabla \cdot \vec{B} = 0$ and then using the Divergence Theorem to find the path of the field lines. The Divergence Theorem physically implies that in the absence of the creation or destruction of magnetic field lines, the magnetic density within a region of space can only change by having it flow into or away from the region over the boundary. Or mathematically, if τ is a region in space with a boundary $d\tau$, then the volume integral of the divergence of a magnetic field $\vec{B}$ over τ and the surface integral of $\vec{B}$ over the boundary $d\tau$ of τ are related by the following expression:

$$\int_{volume} (\nabla \cdot \vec{B}) d\tau = \oint_{surface} \vec{B} \cdot d\vec{A} = 0, \tag{3.7}$$

with $d\tau$ the volume element enclosed by the Gaussian surface defined by two spheres with radii $r_\odot$ and r_{ss}, respectively. It is assumed that the heliomagnetic longitude to which the magnetic field expands remain unchanged, thus:

$$\phi_{hm}^{ss} = \phi_{hm}^{ph}. \tag{3.8}$$

Then Eq. 3.7 becomes

$$\oint \vec{B} \cdot d\vec{A} = \int \vec{B_\odot} \cdot d\vec{A_\odot} + \int \vec{B_{ss}} \cdot d\vec{A_{ss}} = 0. \tag{3.9}$$

where $d\vec{A_\odot} = -r_\odot^2 \sin\theta_{hm}^{ph} d\theta_{hm}^{ph} d\phi_{hm}^{ph} \vec{r}_1$ and $d\vec{A_{ss}} = r_{ss}^2 \sin\theta_{hm}^{ph} d\theta_{hm}^{ph} d\phi_{hm}^{ph} \vec{r}_1$ with $\vec{r}_1$ a unit vector in the radial direction. Eq. 3.9 implies that the total flux of the field from the photosphere is equal to the flux through the source surface, independent of what happens to the field lines between the two surfaces.

Furthermore, the magnetic field is assumed to be uniform on the source surface and dipolar on the photosphere and in the low corona [*Fisk*, 1996]. The photospheric and source surface field strengths are then given by $B_r = B_0 \cos\theta_{hm}^{ph}$ and B_{ss}, respectively, where B_0 and B_{ss} are constants. Thus,

$$\int_0^{\theta_{hm}^{ph}} B_0 \cos\theta_{hm}^{ph} r_\odot^2 \sin\theta_{hm}^{ph} d\theta_{hm}^{ph} \int_0^{2\pi} d\phi_{hm}^{ph} = \int_0^{\theta_{hm}^{ss}} B_{ss} r_{ss}^2 \sin\theta_{hm}^{ss} d\theta_{hm}^{ss} \int_0^{2\pi} d\phi_{hm}^{ss}. \tag{3.10}$$

Since the expansion is symmetric about $\vec{M}$, Eq. 3.8 changes Eq. 3.10 to

$$B_0 r_\odot^2 \int_0^{\theta_{hm}^{ph}} \cos\theta_{hm}^{ph} \sin\theta_{hm}^{ph} d\theta_{hm}^{ph} = B_{ss} r_{ss}^2 \int_0^{\theta_0^{\theta_{hm}^{22}}} \sin\theta_{hm}^{ss} d\theta_{hm}^{ss}, \tag{3.11}$$

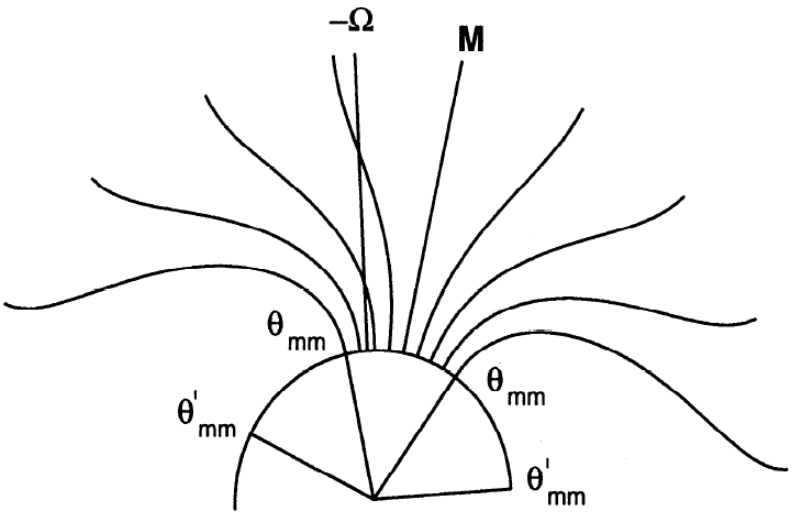

Figure 3.3: Expansion of magnetic field lines from the PCH. θ_{mm} and $\theta_{mm}^{'}$ are the boundary of the CH on the photosphere and the maximum heliomagnetic latitude to which the magnetic field expands on the source surface, respectively (figure adapted from *Fisk* [1996]).

from which it readily follows that

$$\frac{1}{2}B_0 r_\odot^2 \sin^2\theta_{hm}^{ph} = B_{ss} r_{ss}^2 (1 - \cos\theta_{hm}^{ss}). \tag{3.12}$$

It is assumed that magnetic field lines originate in a PCH centred on the magnetic axis, in the form of a circle with its maximum extent denoted by θ_{mm} in Figure 3.3. In other words, θ_{mm} represents the boundary of the PCH. In Figure 3.3, the prime refers to the source surface, but to maintain continuity, the prime will be replaced by the superscript ss. These open magnetic field lines expand symmetrically with respect to the magnetic axis to some maximum expansion boundary in heliomagnetic co-latitude (θ_{mm}^{ss}) on the source surface which means the magnetic field expands over underlying closed magnetic field regions on the photosphere. Therefore, equating θ_{hm}^{ph} to θ_{mm}^{ph} and θ_{hm}^{ss} to θ_{mm}^{ss} in Eq. 3.12 leads to

$$\frac{B_0 r_\odot^2}{2} \sin^2\theta_{mm}^{ph} = B_{ss} r_{ss}^2 (1 - \cos\theta_{mm}^{ss}). \tag{3.13}$$

Now, dividing Eq. 3.12 by Eq. 3.13 gives an expression of the heliomagnetic co-latitude to which a magnetic field line expands from the photosphere to the source surface:

$$\cos\theta_{hm}^{ss} = 1 - (1 - \cos\theta_{mm}^{ss}) \left(\frac{\sin^2\theta_{hm}^{ph}}{\sin^2\theta_{mm}^{ph}} \right). \tag{3.14}$$

Since the field lines expand uniquely from the surface of the Sun to the solar wind source surface, Eq. 3.14 can be used to trace magnetic field lines back from the source surface to the photosphere by only changing the subject of the equation:

$$\sin^2\theta_{hm}^{ph} = \sin^2\theta_{mm}^{ph}\left(\frac{1-\cos\theta_{hm}^{ss}}{1-\cos\theta_{mm}^{ss}}\right). \tag{3.15}$$

The third and final step is performing a rotation transformation about the angle α from heliomagnetic coordinates on the photosphere back to heliographic coordinates on the photosphere. Note, the rotation matrix from Eq. 3.16 is different from Eq. 3.3 since the rotation during this phase is in the opposite direction,

$$\begin{bmatrix} x_{hg}^{ph} \\ y_{hg}^{ph} \\ z_{hg}^{ph} \end{bmatrix} = \begin{bmatrix} \cos\alpha & 0 & \sin\alpha \\ 0 & 1 & 0 \\ -\sin\alpha & 0 & \cos\alpha \end{bmatrix} \begin{bmatrix} x_{hm}^{ph} \\ y_{hm}^{ph} \\ z_{hm}^{ph} \end{bmatrix}. \tag{3.16}$$

Expanding Eq. 3.16 by standard matrix multiplication leads to:

$$\begin{aligned} x_{hg}^{ph} &= x_{hm}^{ph}\cos\alpha + z_{hm}^{ph}\sin\alpha \\ y_{hg}^{ph} &= y_{hm}^{ph} \\ z_{hg}^{ph} &= z_{hm}^{ph}\cos\alpha - x_{hm}^{ph}\sin\alpha. \end{aligned} \tag{3.17}$$

Again, making use of the relationship between Cartesian and spherical coordinates

$$\begin{aligned} x_{hg}^{ph} &= r\sin\theta_{hg}^{ph}\cos\phi_{hg}^{ph} & x_{hm}^{ph} &= r\sin\theta_{hm}^{ph}\cos\phi_{hm}^{ph} \\ y_{hg}^{ph} &= r\sin\theta_{hg}^{ph}\sin\phi_{hg}^{ph} & y_{hm}^{ph} &= r\sin\theta_{hm}^{ph}\sin\phi_{hm}^{ph} \\ z_{hg}^{ph} &= r\cos\theta_{hg}^{ph} & z_{hm}^{ph} &= r\cos\theta_{hm}^{ph}, \end{aligned} \tag{3.18}$$

with $r = \sqrt{\left(x_{hm}^{ph}\right)^2 + \left(y_{hm}^{ph}\right)^2 + \left(z_{hm}^{ph}\right)^2} = \sqrt{\left(x_{hg}^{ph}\right)^2 + \left(y_{hg}^{ph}\right)^2 + \left(z_{hg}^{ph}\right)^2}$. Eqs. 3.17 becomes:

$$\begin{aligned} \cos\theta_{hg}^{ph} &= \cos\theta_{hm}^{ph}\cos\alpha - \sin\theta_{hm}^{ph}\cos\phi_{hm}^{ph}\sin\alpha \\ \sin\theta_{hg}^{ph}\sin\phi_{hg}^{ph} &= \sin\theta_{hm}^{ph}\sin\phi_{hm}^{ph} \\ \cos\phi_{hg}^{ph} &= \frac{\cos\theta_{hm}^{ph}\sin\alpha + \sin\theta_{hm}^{ph}\cos\phi_{hm}^{ph}\cos\alpha}{\sin\theta_{hg}^{ph}}, (\theta_{hg}^{ph} \neq 0), \end{aligned} \tag{3.19}$$

again in agreement with the results of *Fisk* [1996] and *Van Niekerk* [2000].

It is now a simple matter to apply the transformations in reverse order to map a position in heliographic coordinates on the source surface to a position in heliographic coordinates on the photosphere. Eqs. 3.20 to 3.25 summarizes the expressions that are used to trace a magnetic field line from the source surface to the photosphere.

Heliographic to heliomagnetic coordinates on the source surface:

$$\theta_{hm}^{ss} = \cos^{-1}(\cos\theta_{hg}^{ss}\cos\alpha + \sin\theta_{hg}^{ss}\sin\alpha\cos\phi_{hg}^{ss}) \tag{3.20}$$

$$\phi_{hm}^{ss} = \cos^{-1}\left(\frac{\sin\theta_{hg}^{ss}\cos\phi_{hg}^{ss}\cos\alpha - \cos\theta_{hg}^{ss}\sin\alpha}{\sin\theta_{hm}^{ss}}\right) \tag{3.21}$$

Mapping down from source surface to photosphere in heliomagnetic coordinates while heliolongitude remains constant:

$$\theta_{ph}^{hm} = \sin^{-1}\left(\sqrt{\frac{(1-\cos\theta_{hm}^{ss})\sin^2(\theta_m^{ph})}{(1-\cos\theta_{mm}^{ss})}}\right) \tag{3.22}$$

$$\phi_{hm}^{ss} = \phi_{hm}^{ph} \tag{3.23}$$

Heliomagnetic to heliographic coordinates on photosphere:

$$\theta_{hg}^{ph} = \cos^{-1}(\cos\theta_{hm}^{ph}\cos\alpha - \sin\theta_{hm}^{ph}\cos\phi_{hm}^{ph}\sin\alpha) \tag{3.24}$$

$$\phi_{hg}^{ph} = \cos^{-1}\left(\frac{\cos\theta_{hm}^{ph}\sin\alpha + \sin\theta_{hm}^{ph}\cos\phi_{hm}^{ph}\cos\alpha}{\sin\theta_{hg}^{ph}}\right) \tag{3.25}$$

Figures 3.4a through 3.4c show how the transformations from heliographic to heliomagnetic and *vice versa* take place from the source surface to the surface of the Sun. All angles referred to in this section are in co-latitude. For illustrative purposes, the heliomagnetic coordinates of the coronal hole boundary on the photosphere (θ_m^{ph}) and its boundary on the source surface (θ_{mm}^{ph}) is chosen to be 24° and 70°, respectively.

The graphical interpretation of Equation 3.20 is shown in Figure 3.4a which is the rotation transformation about the angle $\alpha = 20^\circ$ from heliographic to heliomagnetic coordinates on the source surface (denoted by a prime). The heliographic longitude on the source surface is arbitrarily chosen to be $\phi_{hg}^{ss} = 180^\circ$, the azimuth of the co-planar axes $\vec{p}$, $\vec{\Omega}$ and $\vec{M}$. The magnetic footpoint at the pole of the source surface is at $\theta_{hm}^{ss} = 20^\circ$ after the rotation transformation. This is confirmed by Figure 3.4a where it can clearly be seen $\theta_{hg}^{ss} = 0^\circ$ maps to $\theta_{hm}^{ss} = 20^\circ$. Note that the relationship between the heliographic polar angle and the heliomagnetic polar angle, both on the source surface, is linear, as expected.

Figure 3.4b shows the graphical interpretation of Eq. 3.22 where the heliomagnetic polar angle on the source surface is mapped to the heliomagnetic polar angle on the photosphere. Firstly note, the horizontal axis of Figure 3.4b is the vertical axis of Figure 3.4a and therefore their scaling are the same. This relationship is not linear and is dictated by the chosen boundaries of the PCH. The vertical and the horizontal dashed lines in Figure 3.4b represent the chosen boundaries of the PCH on the source surface and the photosphere, respectively. Magnetic field lines outside these boundaries, e.g. all $\theta_{hm}^{ss} > 70^\circ$ and all $\theta_{hm}^{ph} > 24^\circ$ do not experience coherent footpoint motion; rather they are transported by means of diffusive reconnection (see e.g. *Fisk et al.* [1999a]). Consequently the field origination in that region are Parker-like.

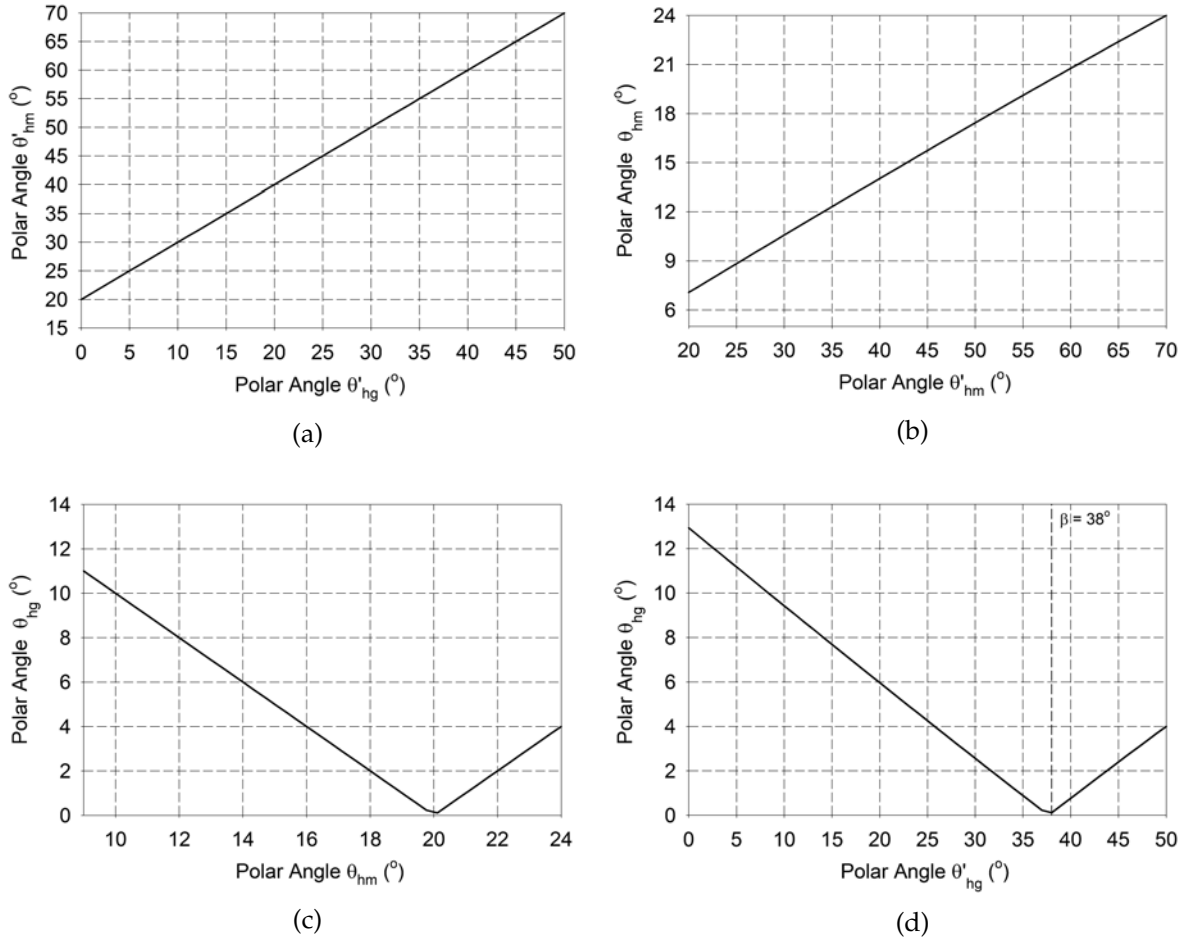

Figure 3.4: Step-by-step graphical representation of the transformations of a traced magnetic field line between heliographic and heliomagnetic coordinates from the source surface to the photosphere. The prime refers to the source surface.

Figure 3.4c follows from Eq. 3.24 where a relationship between the heliomagnetic polar angle and the heliographic polar angle, both on the photosphere, is drawn after a rotation transformation about the angle α. Consequently, the vertical dashed line shows a magnetic field line at $\theta_{hm}^{ph} = 20°$ at the heliographic pole after the rotation transformation of $\alpha = 20°$.

Lastly, to complete the process, it is advantageous to visualise all the transformations on one plot by following a magnetic field line in heliographic coordinates on the source surface down to its heliographic footpoint anchored in the photosphere. Figure 3.4d shows this relationship. Since a magnetic field line originating from the pole of the Sun sets out to the $\vec{p}$-axis, an expression for the heliographic angle β can be derived from Eq. 3.14 by assuming $\theta_m^{ph} = \alpha$, implying $\theta_{mm}^{ss} = \alpha + \beta$ [*Krüger*, 2005]. Therefore,

$$\beta = \cos^{-1}\left[1 - (1 - \cos\theta_{mm}^{ss})\left(\frac{\sin^2\alpha}{\sin^2\theta_m^{ph}}\right)\right] - \alpha \tag{3.26}$$

Note that this is the same expression of Eq. 4.32, but using the nomenclature of the current chapter. Using Eq. 3.26 with $\theta_{mm}^{ss} = 75°$, $\theta_{mm}^{ph} = 24°$, and $\alpha = 20°$ results in a $\beta = 37.7°$ which is shown in Figure 3.4d by the vertical dashed line. Thus, a magnetic field line at $\theta_{hg}^{ss} = \beta = 38°$

on the source surface maps down to the heliographic pole of the Sun.

3.4 Derivation of the Footpoint Velocity Field

This proof starts with the footpoint velocity field, Eqs. 3.29 and 3.30 but with $F_s = \text{constant} = 1$, for the original Fisk field,

$$U_\theta^m = \omega r \sin\beta \sin\phi \tag{3.27}$$

$$U_\phi^m = \omega r \left[\cos\beta \sin\theta + \sin\beta \cos\theta \cos\phi\right], \tag{3.28}$$

assuming that the footpoint trajectories are circles around the $\vec{p}$-axis. Note that these expressions are for a frame co-rotating with the Sun, and the coordinates are heliographic.

Similar to the methodology to derive the footpoint velocity for the Fisk-Parker hybrid field in the next chapter, it is assumed that there is an additional component to the ϕ-component, say $S(\theta, \phi)$. To ensure a divergence-free velocity field, it follows that $d/d\phi(U_\phi + S(\theta,\phi)) + d/d\theta(U_\theta) = 0$. Denoting the components for the generalised Fisk field with a superscript g, it then follows that

$$U_\theta^g = r\omega(\theta,\phi) \sin\beta \sin\phi \tag{3.29}$$

$$\begin{aligned}
U_\phi^g &= r\omega(\theta,\phi) \sin\beta \cos\theta \cos\phi + r\omega(\theta,\phi) \cos\beta \sin\theta \\
&\quad - r \sin\theta \sin\beta \int \sin\phi \frac{\partial}{\partial\theta}\omega(\theta,\phi) d\phi \\
&\quad - r \sin\beta \cos\theta \int \cos\phi \frac{\partial}{\partial\phi}\omega(\theta,\phi) d\phi \\
&\quad - r \sin\theta \cos\beta \int \frac{\partial}{\partial\phi}\omega(\theta,\phi) d\phi \\
&\equiv r\omega(\theta,\phi) \sin\beta \cos\theta \cos\phi - r \sin\theta \sin\beta \int \sin\phi \frac{\partial}{\partial\theta}\omega(\theta,\phi) d\phi \\
&\quad - r \sin\beta \cos\theta \int \cos\phi \frac{\partial}{\partial\phi}\omega(\theta,\phi) d\phi \\
&\quad - r \sin\theta \cos\beta \int \frac{\partial}{\partial\phi}\omega(\theta,\phi) d\phi,
\end{aligned} \tag{3.30}$$

after the second and last terms cancel. The θ-components of the modified Fisk-type field and the generalised Fisk field have the same form. Due to its current integral form, Eq. 3.30 should first be simplified before the magnetic field expressions can be derived. Firstly, the integrand of the first integral in Eq. 3.30 has a term involving the differential of the differential rotation rate with respect to its polar angle, that is, $\frac{\partial\omega(\theta,\phi)}{\partial\theta}$. Secondly, the integrand of the second integral of Eq. 3.30 includes a $\frac{\partial\omega(\theta,\phi)}{\partial\phi}$ term. Finding an expression that relates the change of the polar angle in terms of the azimuthal angle, and *vice versa*, together with an expression relating the change in the differential rotation rate in terms of the polar and azimuthal angle, will significantly simplify Eq. 3.30. In fact, such an expression is readily calculated for the assumed circular trajectories about the p-axis.

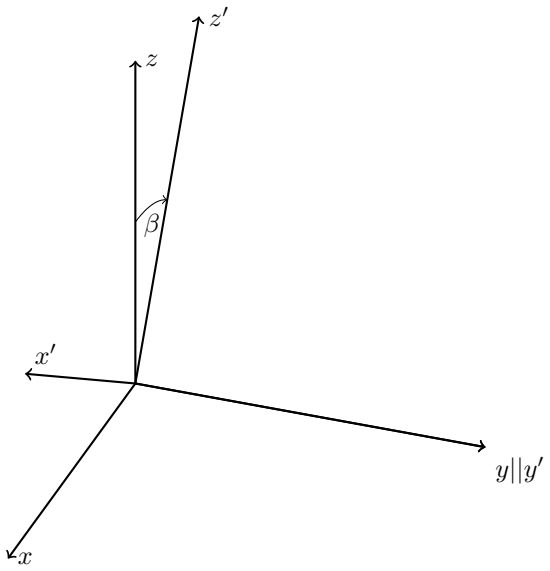

Figure 3.5: Rotation about the y-axis.

Consider Figure 3.5 which shows a three-dimensional Cartesian coordinate system with x, y, and z as its bases, resembling a heliographic coordinate system. The expression for a circle in the primed coordinate system in the $x'y'$ plane is the standard

$$x'^2 + y'^2 = r^2. \tag{3.31}$$

This expression is readily transformed to xyz coordinates,

$$x^2 \cos^2\beta + z^2 \sin^2\beta + 2xz\cos\beta\sin\beta + y^2 = r^2 \tag{3.32}$$

where β is the angle of rotation. Next, the standard transformations are used to transform Eq. 3.32 to spherical coordinates. With R the radius of the source surface, the standard transformations are:

$$\begin{aligned} x &= R\sin\theta\cos\phi \\ y &= R\sin\theta\sin\phi \\ z &= R\cos\theta. \end{aligned} \tag{3.33}$$

Substituting these transformations into Eq: 3.32, gives:

$$\begin{aligned} &\sin^2\theta\cos^2\phi\cos^2\beta + \cos^2\theta\sin^2\beta \\ &+2\sin\theta\cos\phi\cos\theta\cos\beta\sin\beta + \sin^2\theta\sin^2\phi = \frac{r^2}{R^2} \end{aligned} \tag{3.34}$$

By using implicit differentiation, Eq. 3.34 is used to find a relationship between $d\theta/d\phi$ and $d\phi/d\theta$. After rearranging terms, the relationships are found to be

$$\frac{d\theta}{d\phi} = \frac{\sin\phi}{\cot\beta + \cot\theta\cos\phi}, \tag{3.35}$$

$$\frac{d\phi}{d\theta} = \frac{\cot\beta + \cot\theta\cos\phi}{\sin\phi}. \tag{3.36}$$

It is now assumed that the differential rotation remaining constant on a circle trajectory on the source surface, implying that

$$d\omega(\theta,\phi) = \frac{\partial\omega}{\partial\theta}d\theta + \frac{\partial\omega}{\partial\phi}d\phi = 0. \tag{3.37}$$

After rearranging terms, Eq. 3.37 is rewritten in terms of

$$\frac{\partial\omega}{\partial\theta} = -\frac{\partial\omega}{\partial\phi}\frac{d\phi}{d\theta}. \tag{3.38}$$

Substituting Eqs. 3.35, 3.36, and 3.38, into the second and third terms of Eq. 3.30, yields

$$\begin{aligned}
&r\sin\theta\sin\beta\int\sin\phi\frac{d\phi}{d\theta}\frac{\partial\omega}{\partial\phi}d\phi + r\sin\beta\cos\theta\int\cos\phi\frac{\partial\omega}{\partial\theta}d\theta \\
&= r\sin\theta\sin\beta\int(\cot\beta+\cot\theta\cos\phi)\frac{\partial\omega}{\partial\phi}d\phi + r\omega\sin\beta\cos\theta\cos\phi \\
&= r\omega\sin\theta\sin\beta\cot\beta - r\sin\theta\sin\beta\cot\theta\int\cos\phi\frac{\partial\omega}{\partial\theta}d\theta + r\omega\sin\beta\cos\theta\cos\phi \\
&= r\omega\sin\theta\sin\beta\cot\beta - r\omega\cot\theta\sin\theta\sin\beta\cos\phi + r\omega\sin\beta\cos\theta\cos\phi \\
&= r\omega\sin\theta\sin\beta\frac{\cos\beta}{\sin\beta} - r\omega\sin\beta\cos\phi\sin\theta\frac{\cos\theta}{\sin\theta} + r\omega\sin\beta\cos\phi\cos\theta \\
&= r\omega(\theta,\phi)\cos\beta\sin\theta.
\end{aligned} \tag{3.39}$$

Therefore, the final form of the footpoint motion equations of the generalised Fisk HMF in heliographic coordinates is

$$U^g_\theta = r\omega(\theta,\phi)\sin\beta\sin\phi, \tag{3.40}$$

$$U^g_\phi = r\omega(\theta,\phi)\sin\beta\cos\theta\cos\phi + r\omega(\theta,\phi)\cos\beta\sin\theta. \tag{3.41}$$

It should not come as a surprise that the final form of the footpoint velocity equations of the generalised Fisk field has reduced to that of the original Fisk HMF model with the only difference being the former assumes $\omega(\theta,\phi)$ and the latter $\omega = \text{constant}$. In both cases a circular and therefore closed trajectory is assumed; it is necessarily divergence free. However, to prove that the current velocity field with its spatial dependence of ω is indeed divergence free as it is supposed to be by construction, consider

$$
\begin{aligned}
\vec{\nabla}\cdot\vec{U} &= \frac{1}{r\sin\theta}\frac{\partial}{\partial\theta}\left[r\omega(\theta,\phi)\sin\theta\sin\beta\sin\phi\right] \\
&+ \frac{1}{r\sin\theta}\frac{\partial}{\partial\phi}\left[r\omega(\theta,\phi)\sin\beta\cos\theta\cos\phi + r\omega(\theta,\phi)\cos\beta\sin\theta - r\Omega\sin\theta\right] \\
&= \sin\beta\sin\phi\frac{\partial\omega}{\partial\theta} + \omega\sin\beta\sin\phi\frac{\cos\theta}{\sin\theta} \\
&+ \sin\beta\cos\phi\frac{\cos\theta}{\sin\theta}\frac{\partial\omega}{\partial\phi} - \omega\sin\beta\sin\phi\frac{\cos\theta}{\sin\theta} \\
&- \cos\beta\frac{\partial\omega}{\partial\phi}.
\end{aligned}
\tag{3.42}
$$

The second and fourth term of Eq. 3.42 cancel each other and after using appropriate forms of Eqs. 3.35, 3.36, and 3.38, the divergence reduces to:

$$
\begin{aligned}
\vec{\nabla}\cdot\vec{U} &= -\sin\beta\cot\beta - \sin\beta\cot\theta\cos\phi \\
&+ \sin\beta\cot\theta\cos\phi + \cos\beta \\
&= -\sin\beta\frac{\cos\beta}{\sin\beta} + \cos\beta \\
&= 0.
\end{aligned}
\tag{3.43}
$$

3.5 The Visualization of the Footpoint Trajectories

Two coupled first-order differential equations are solved simultaneously in the co-rotating reference frame to graphically represent the footpoint trajectories on the solar wind source surface in heliographic coordinates. These two equations stem from the footpoint velocity equations from Section 3.4:

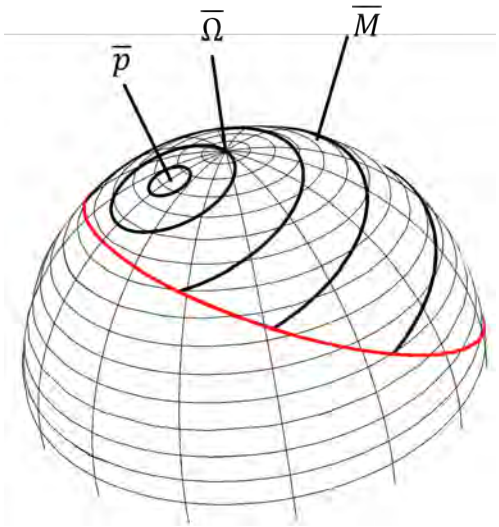

Figure 3.6: Visualisation of the footpoint motion trajectories symmetric about the $\vec{p}$-axis on the source surface. The solid red circle denotes the boundary of the PCH on the source surface beyond which the field is Parker-like. The direction of travel of the footpoints is anti-clockwise.

$$\begin{aligned} \frac{d\theta}{dt} r &= r\omega \sin\beta \sin\phi \\ \therefore \frac{d\theta}{dt} &= \omega \sin\beta \sin\phi. \end{aligned} \tag{3.44}$$

$$\begin{aligned} \frac{d\phi}{dt} r \sin\theta &= r\omega \sin\beta \cos\theta \cos\phi + r\omega \cos\beta \sin\theta \\ \therefore \frac{d\phi}{dt} &= \omega \sin\beta \frac{\cos\theta}{\sin\theta} \cos\phi + \omega \cos\beta. \end{aligned} \tag{3.45}$$

The azimuthal angle ϕ is arbitrarily chosen to be 180° in the plane of the co-planar $\vec{p}$-, rotation- and magnetic axes. The footpoint trajectories above are the same as those of the Fisk field since the same footpoint velocity equations are valid for both magnetic fields. Symmetry about the magnetic equator is assumed in the generalised Fisk HMF model. From the closest footpoint trajectory to the $\vec{p}$-axis to the trajectory closest to the equator, the polar angles are $\theta = 10^\circ$, $\theta = 30^\circ$, $\theta = 45^\circ$, $\theta = 60^\circ$, and $\theta = 80^\circ$, respectively. In reality the trajectories would become less circular and more oval-shaped with increasing co-latitude if the actual mapping of Eqs. 3.18 to 3.23 are used. This was in fact tested and found to have a negligible effect at the latitudes of relevance to the present study (see also Figure 4.6 of *Van Niekerk* [2000] as confirmation). At latitudes below the boundary of the PCH on the source surface the field is assumed to be Parker-like. The second trajectory with $\theta = 30^\circ$, intersects $\vec{\Omega}$ which reflects the Fisk angle of $\beta = 15^\circ$ used to draw these trajectories.

3.6 Derivation of the Field Line Trajectories

The method of deriving the field line trajectories (also referred to as streamlines) for the generalised Fisk HMF model below is standard and also therefore used by *Zurbuchen et al.* [1997] and *Van Niekerk* [2000]. In order to visualise the magnetic field lines of the generalised Fisk HMF model as it expands into the heliosphere from the source surface, the differential equation of a streamline is derived by ensuring $d\vec{l} \times \vec{U} = \vec{0}$, where $d\vec{l} = dr\vec{r} + rd\theta\vec{\theta} + r\sin\theta d\phi\vec{\phi}$ in the time-stationary frame and the components of $\vec{U}$ in the co-rotating frame are:

$$U_r^g = V \tag{3.46}$$

$$U_\theta^g = r\omega(\theta,\phi) \sin\beta \sin\phi \tag{3.47}$$

$$U_\phi^g = r\omega(\theta,\phi) \sin\beta \cos\theta \cos\phi + r\omega(\theta,\phi) \cos\beta \sin\theta - \Omega r \sin\theta \tag{3.48}$$

The term $-\Omega r \sin\theta$ represents the rotation of the Sun as a whole. Calculating $d\vec{l} \times \vec{U} = \vec{0}$ leads to the following relationships:

$$\frac{dr}{U_\theta^g} = \frac{rd\theta}{U_\theta^g} = \frac{r\sin\theta d\phi}{U_\phi^g} \tag{3.49}$$

Substituting Eqs. 3.46 - 3.48 into Eq. 3.49 gives:

$$\frac{d\theta}{dr} = \frac{U_\theta^g}{rU_r^g} = \frac{\omega(\theta,\phi)}{V}\sin\beta\sin\phi, \tag{3.50}$$

$$\frac{d\phi}{dr} = \frac{U_\phi^g}{r\sin\theta U_r^g} = \frac{\omega(\theta,\phi)}{V}\cos\beta + \frac{\omega(\theta,\phi)}{V}\sin\beta\frac{\sin\theta}{\cos\theta}\cos\phi - \frac{\Omega}{V}. \tag{3.51}$$

Before the final form of the streamline equations can be established, the relationship between the time-stationary azimuthal angle ϕ, and the co-rotating azimuthal angle ϕ_s, should be established. Provided the geometry in Figure 3.7 as seen from the northern heliographic pole and projected onto the xy-plane, consider a small region of solar wind plasma at position A. Because the solar wind plasma is transported radially outward into the heliosphere, this region of plasma initially at position A will be observed at position B in the time-stationary reference frame after some time t has passed. Yet, this region of plasma at position B would seem to have originated from position C on the source surface in the co-rotating reference frame since the Sun has rotated through an azimuthal angle Ωt. Assume ϕ_o to be the azimuthal angle between the time-stationary and the co-rotating X-axes, ϕ to be the azimuthal angle of position C, and ϕ_s the azimuthal position of position A (or B). Now, using all the information given in Figure 3.7, a relationship between the time-stationary and the co-rotating azimuthal angle can be established by noting:

$$\phi = \phi_s + \Omega t - \phi_o \tag{3.52}$$

Since the solar wind flows radially away from the Sun, the solar wind speed can be recast in terms of

$$V = \frac{r}{t} \implies t = \frac{r}{V} \tag{3.53}$$

Substituting Eq. 3.53 into Eq. 3.52 gives:

$$\phi = \phi_s + \frac{\Omega r}{V} - \phi_o. \tag{3.54}$$

Replacing ϕ in Eqs. 3.50 and 3.51 with Eq. 3.54 gives the final form of the streamline equations of the generalised Fisk HMF model:

$$\frac{d\theta_s}{dr} = \frac{\omega(\theta,\phi)}{V}\sin\beta\sin\left(\phi_s + \frac{\Omega t}{V} - \phi_o\right), \tag{3.55}$$

$$\frac{d\phi_s}{dr} = \frac{\omega(\theta,\phi)}{V}\cos\beta + \frac{\omega(\theta,\phi)}{V}\sin\beta\frac{\sin\theta}{\cos\theta}\cos\left(\phi_s + \frac{\Omega t}{V} - \phi_o\right) - \frac{\Omega}{V}. \tag{3.56}$$

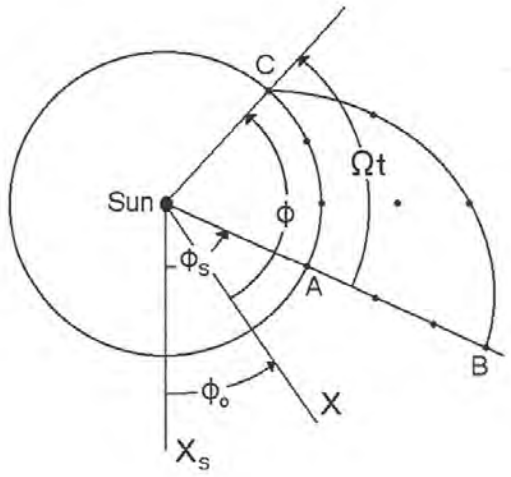

Figure 3.7: Illustration of the relationship between ϕ and ϕ_s from the perspective of the northern heliographic pole. The outer circle represents the solar wind source surface. This figure is adapted form *Van Niekerk* [2000].

3.7 Visualisation of the Magnetic Field Lines of the Generalised Fisk-type HMF

The magnetic field lines of the generalised Fisk HMF model are graphically obtained by simultaneously solving the coupled differential streamline equations from Section 3.6. Figures 3.8 and 3.9 show different viewing perspectives of the magnetic field lines' configurations for $\theta_{hg}^{ss} = 15^\circ, 30^\circ, 40^\circ, 55^\circ$ with a chosen $\alpha = 15^\circ$ and subsequently a $\beta = 27.8^\circ$ from Eq. 3.26. The same PCH size were used for all the configurations, namely $\theta_m^{ph} = 24^\circ$ and $\theta_{mm}^{ss} = 70^\circ$. For this exercise, all θ_{hg}^{ss} values were chosen such that the subsequent θ_{hm}^{ph} values fall within the bounds of the PCH. Implementing all these physical parameters, it is easy to see the maximum extent of the magnetic field lines on the source surface in heliographic coordinates is 55° since $\theta_{hg}^{ss} = 55^\circ$ maps back to $\theta_{hm}^{ph} = 24^\circ$ which defines the chosen boundary of the PCH. Refer to Table 3.2 to see all information regarding the polar and azimuthal angles in both heliographic and heliomagnetic coordinates.

The magnetic field in Figures 3.8 and 3.9 show the typical complex structure that is expected of a Fisk-type magnetic field model. Since the solar wind is dragged out radially and the footpoints traverse latitudinally on the source surface, these entangled patterns are created. Nonetheless, the magnetic field lines of the generalised Fisk field model are quite different from the Fisk *Fisk* [1996] model in the fact that ω is implemented differently.

The first row in Table 3.2 refers to Figure 3.8a. Firstly, a heliographic co-latitude of 15° is chosen, secondly it is transformed to a heliomagnetic co-latitude of 30° after which it is mapped down to the photosphere to 10.6° and then transformed back to a heliographic co-latitude of 4.4°. Therefore, a chosen $\theta_{hg}^{ss} = 15^\circ$ on the source surface maps to $\theta_{hg}^{ph} = 4.4^\circ$ on the photopshere. Using the expression of *Snodgrass* [1983] (Eq. 2.2 of Chapter 2), this then implies $\omega(\theta, \phi) = 0.785$ μ rads/s, or equivalently a period of 92.6 days. The Fisk model of *Fisk* [1996] used a constant fraction of the equatorial rotation rate to express its differential rotation rate, e.g. $\omega = \Omega/4 = 100$

days. Comparing with the other values in Table 3.2, it is evident that the constant value is in fact a reasonable choice. Figure 3.8d shows the most "Fiskness", or equivalently the most significant departure from Parker-like behaviour. Of the four, this field line's trajectory has the largest angular distance with respect to the $\vec{p}$-axis. The field lines of Figures 3.8a and 3.8c appear rather similar; they are at comparable angular distances from the $\vec{p}$-axis. The footpoint of the field line in Figure 3.8b experiences a maximum meridional variation of only about four degrees. It's behaviour is therefore almost Parker-like. Had it originated at the same polar angle as β, it would have been a pure Parker spiral. However, field lines originating at the same polar angle but other azimuthal angles, would be Fisk-like.

Magnetic field lines that fall outside the PCH boundaries, i.e. the magnetic field lines travelling beyond the red footpoint trajectories of Figure 3.6, are assumed to behave Parker-like as stated before. This assumption and its implications will be discussed in Section 3.9.

	θ_{hg}^{ss}	θ_{hm}^{ss}	ϕ_{hm}^{ss}	θ_{hm}^{ph}	θ_{hg}^{ph}	ω μrads/s	Period (Days)
Figure 3.8a	$15°$	$30°$	$180°$	$10.6°$	$4.4°$	0.785	92.6
Figure 3.8b	$30°$	$45°$	$180°$	$15.7°$	$0.7°$	0.791	91.9
Figure 3.8c	$40°$	$55°$	$180°$	$19.1°$	$4.1°$	0.786	92.5
Figure 3.8d	$55°$	$70°$	$180°$	$24°$	$9°$	0.764	95.2

Table 3.2: Polar and azimuthal angles of the mapping down of magnetic field lines from the source surface to the photosphere.

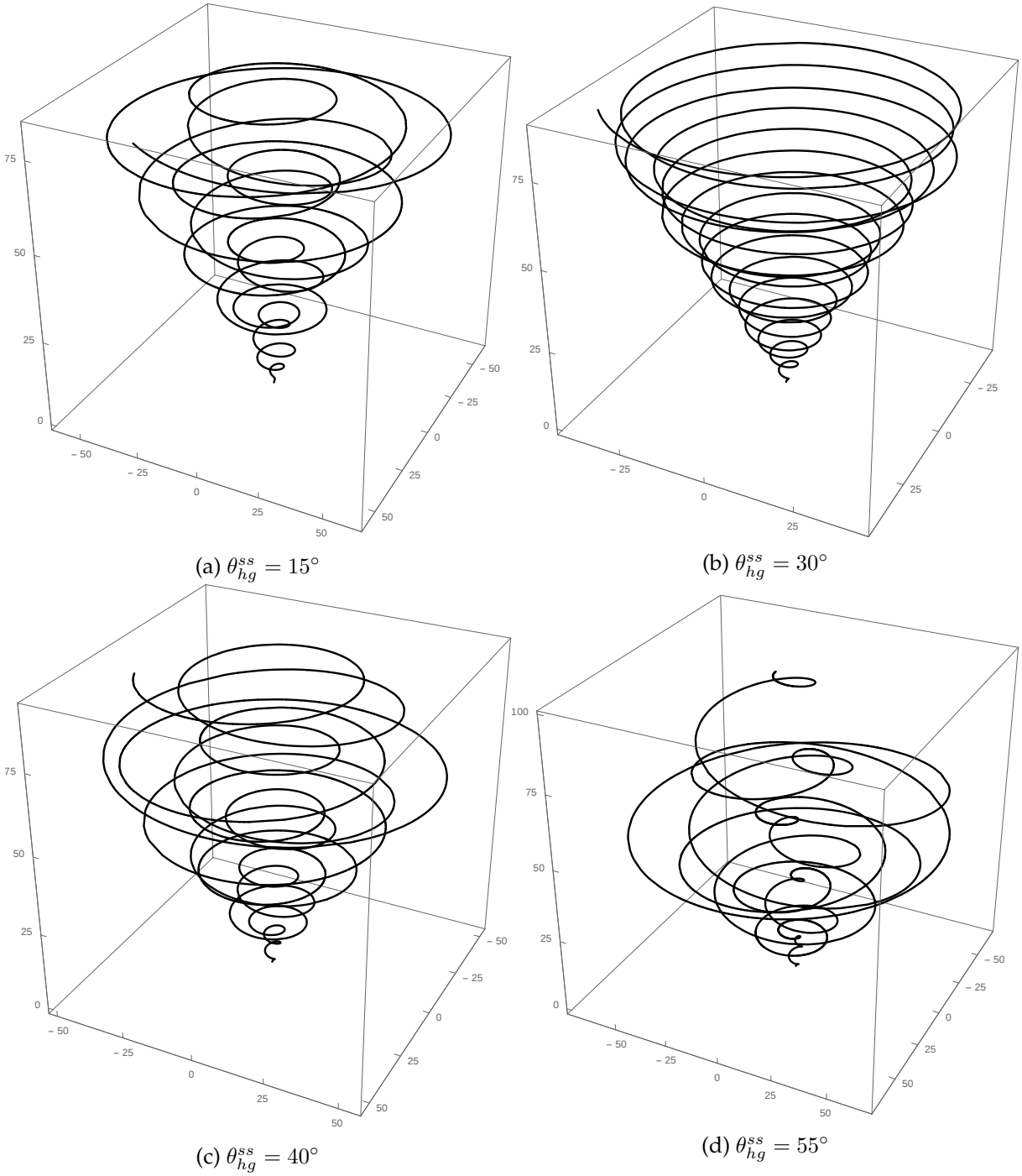

(a) $\theta_{hg}^{ss} = 15°$

(b) $\theta_{hg}^{ss} = 30°$

(c) $\theta_{hg}^{ss} = 40°$

(d) $\theta_{hg}^{ss} = 55°$

Figure 3.8: The configuration of the magnetic field lines of the generalised Fisk HMF emerging from different heliographic co-latitudes on the solar wind source surface seen from above the ecliptic plane. The angular separation between the trajectory and the $\vec{p}$-axis is approximately 13, 2, 10 and 27 degrees, respectively.

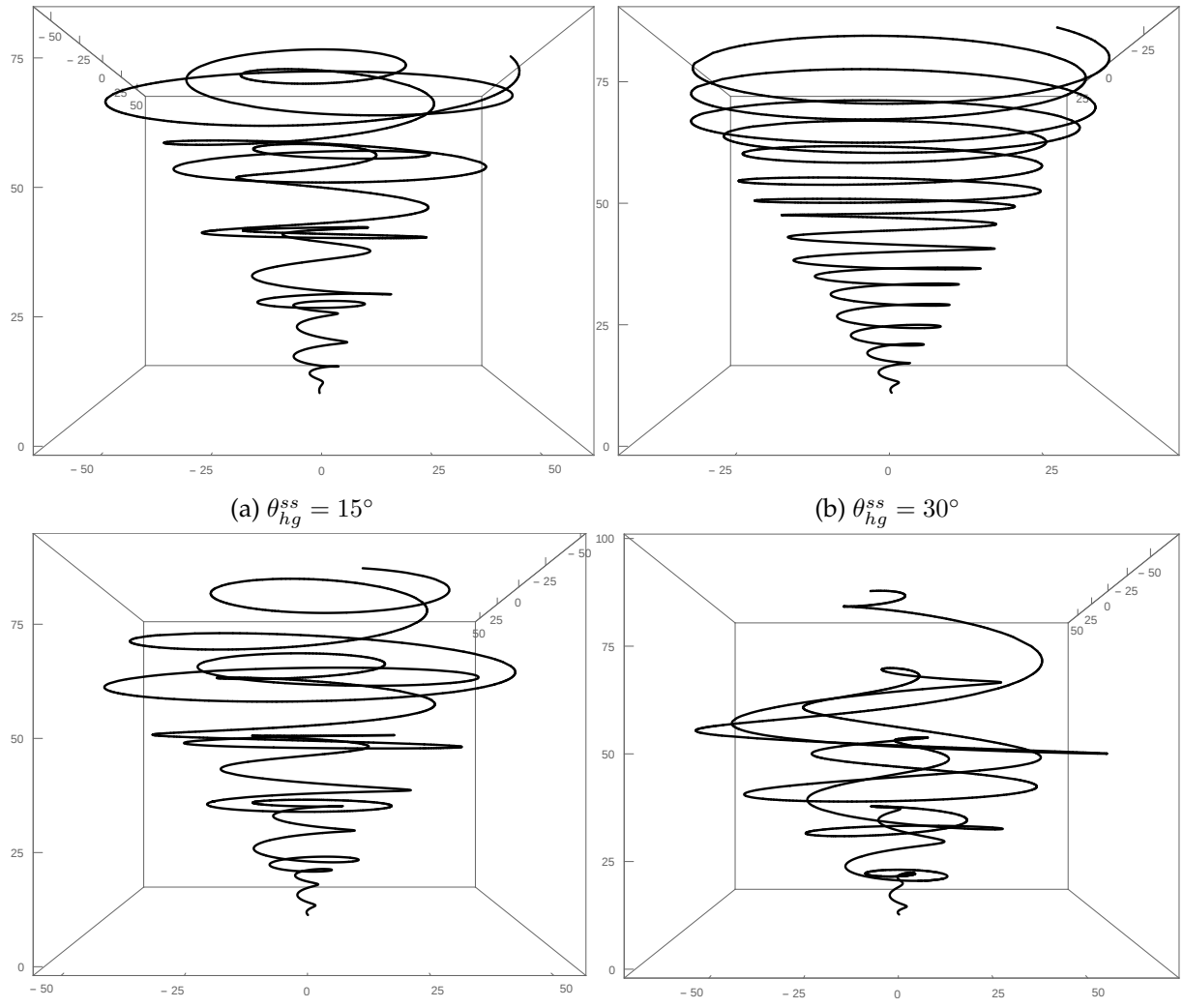

(a) $\theta_{hg}^{ss} = 15°$ (b) $\theta_{hg}^{ss} = 30°$

(c) $\theta_{hg}^{ss} = 40°$ (d) $\theta_{hg}^{ss} = 55°$

Figure 3.9: The configuration of the magnetic field lines in Figure 3.8 as seen from the ecliptic plane.

3.8 Derivation of the Components of the Generalised Fisk Field

Since the solar wind plasma is highly conductive, the frozen-in-field theorem is assumed to be valid [*Alfvén*, 1943]. No perpendicular motion between the solar wind plasma and the magnetic field is allowed and therefore these two vector quantities are parallel. Physically, it means the magnetic field lines are dragged out into the heliosphere by the solar wind plasma, and mathematically it implies the following:

$$\vec{B} \times \vec{U} = \vec{0} \tag{3.57}$$

where $\vec{B}$ and $\vec{U}$ are the magnetic field vector and the plasma velocity vector in the time-stationary frame, respectively. Following the standard rules to calculate a vector product, it follows from Eq. 3.57 that

$$\frac{B_r}{B_\theta} = \frac{U_r}{U_\theta} \implies B_\theta = B_r \frac{U_\theta}{U_r} \tag{3.58}$$

$$\frac{B_r}{B_\phi} = \frac{U_r}{U_\phi} \implies B_\phi = B_r \frac{U_\phi}{U_r} \tag{3.59}$$

By ensuring Maxwell's equation $\vec{\nabla} \cdot \vec{B} = \vec{0}$ is satisfied and using the Divergence Theorem to rewrite Maxwell's equations as in Eq. 3.7, the same process of calculating the radial component of the Fisk field in *Van Niekerk* [2000] and *Zurbuchen et al.* [1997] can be used to calculate the radial component of the generalised Fisk HMF model. Substituting Eqs. 3.47 and 3.48 into Eqs. 3.58 and 3.59 the magnetic field components are given by

$$B_r = A \left(\frac{r_0}{r}\right)^2, \tag{3.60}$$

$$B_\theta = \frac{B_r}{V} \omega(\theta, \phi) r \sin\beta \sin\left(\phi_s + \frac{\Omega r}{V} - \phi_o\right), \tag{3.61}$$

$$B_\phi = \frac{B_r}{V} \left\{ r\omega(\theta, \phi) \left[\sin\beta \cos\theta \cos\left(\phi_s + \frac{\Omega r}{V} - \phi_o\right) + \cos\beta \sin\theta \right] - \Omega r \sin\theta \right\}. \tag{3.62}$$

The magnetic field expressions of the generalised Fisk field are similar to those derived for the original Fisk field in *Zurbuchen et al.* [1997], with the only difference being the spatial dependence of the differential rotation rate ω.

Before the final form of the magnetic field equations are presented, a latitudinally-dependent solar wind velocity is incorporated. This is done by making an appropriate modification to the radial component of the expressions to ensure Maxwell's equation is satisfied. First, Eqs. 3.61 and 3.62 are rewritten as

$$B_\theta = \frac{B_r r}{V(\theta)} \omega(\theta, \phi) \sin\beta \sin\phi^*, \tag{3.63}$$

$$B_\phi = \frac{B_r r}{V(\theta)} \left\{ \omega(\theta, \phi) \left[\sin\beta \cos\theta \cos\phi^* + \cos\beta \sin\theta \right] - \Omega \sin\theta \right\}. \tag{3.64}$$

where $\phi^* = \phi + \frac{\Omega r}{V(\theta)} - \phi_o$ which also includes a latitudinal-dependent solar wind velocity term. Since there is no solar wind speed dependencies in the current form of the radial component, Eq. 3.60 together with Eqs. 3.63 and 3.64 are used to determine the divergence of the magnetic field:

$$\vec{\nabla} \cdot \vec{B} = \overbrace{\frac{1}{r} \frac{\partial}{\partial r}(r^2 B_r)}^{\text{a}} + \underbrace{\frac{1}{r \sin\theta} \frac{\partial}{\partial \theta}(\sin\theta B_\theta)}_{\text{b}} + \overbrace{\frac{1}{r \sin\theta} \frac{\partial B_\phi}{\partial \phi}}^{\text{c}} \tag{3.65}$$

Accordingly,

$$a = 0 \tag{3.66}$$

$$b = \frac{B_r r}{V}\omega \sin\beta \cot\theta \sin\phi^* + \frac{B_r r}{V}\sin\beta \sin\phi^* \frac{\partial \omega}{\partial \theta} - \frac{B_r r}{V^2}\omega \sin\beta \sin\phi^* \frac{\partial V}{\partial \theta} - \frac{B_r r}{V^3}\omega\Omega \sin\beta \cos\phi^* \frac{\partial V}{\partial \theta} \tag{3.67}$$

and

$$c = \frac{B_r r}{V(\theta)\sin\theta}\left(\sin\beta \cos\theta \cos\phi^* \frac{\partial \omega}{\partial \phi} - \omega \sin\beta \cos\theta(\theta,\phi)\sin\phi^* + \cos\beta \sin\theta \frac{\partial \omega}{\partial \phi}\right) \tag{3.68}$$

With the use of Eqs. 3.35, 3.36, and 3.38, the second term of b is rewritten as:

$$\frac{B_r}{V}\sin\beta \sin\phi^* \frac{\partial \omega}{\partial \theta} = -\frac{B_r}{V}\cos\beta \frac{\partial \omega}{\partial \phi} - \frac{B_r}{V}\sin\beta \cot\theta \cos\phi^* \frac{\partial \omega}{\partial \phi} \tag{3.69}$$

resulting in

$$b = \frac{B_r r}{V}\omega \sin\beta \cot\theta \sin\phi^* - \frac{B_r r}{V}\cos\beta \frac{\partial \omega}{\partial \phi} - \frac{B_r r}{V}\sin\beta \cot\theta \cos\phi^* \frac{\partial \omega}{\partial \phi} - \frac{B_r r}{V^2}\omega \sin\beta \sin\phi^* \frac{\partial V}{\partial \theta} - \frac{B_r r}{V^3}\omega\Omega \sin\beta \cos\phi^* \frac{\partial V}{\partial \theta} \tag{3.70}$$

Substituting the results of Eqs. 3.66, 3.69, and 3.68 into Eq. 3.65 leads to a non-zero divergence of:

$$\vec{\nabla} \cdot \vec{B} = -\frac{B_r r}{V^2}\omega \sin\beta \sin\phi^* \frac{\partial V}{\partial \theta} - \frac{B_r r}{V^3}\omega\Omega \sin\beta \cos\phi^* \frac{\partial V}{\partial \theta} \tag{3.71}$$

The solar wind velocity can be approximated to only have a radial component since its azimuthal component is negligibly small [*Forsyth et al.*, 1996]. Therefore, an appropriate modification to the radial component is implemented to accommodate the polar angle dependence of the solar wind velocity. This is done by solving the following equation for ψ.

$$\frac{1}{r^2}\frac{\partial}{\partial r}\left(r^2 \psi\right) = -\left(-\frac{B_r r}{V^2}\omega \sin\beta \sin\phi^* \frac{\partial V}{\partial \theta} - \frac{B_r r}{V^3}\omega\Omega \sin\beta \cos\phi^* \frac{\partial V}{\partial \theta}\right) \tag{3.72}$$

The new radial component of the generalised Fisk HMF model with a latitudinally-dependent solar wind velocity, or ψ in Eq. 3.72, is calculated to be:

$$B_r = B_r\left[1 + \frac{r\omega(\theta,\phi)\sin\beta \sin\phi^*}{V(\theta)^2}\frac{\partial V(\theta)}{\partial \theta}\right] \tag{3.73}$$

Consequently, the final form of the magnetic field equations of the generalised Fisk field, including a latitude and longitude dependence in its expression for the differential rotation rate, as well as a latitude dependence in the solar wind velocity are presented below:

$$B_r = B_r\left[1 + \frac{r\omega(\theta,\phi)\sin\beta \sin\phi^*}{V(\theta)^2}\frac{\partial V(\theta)}{\partial \theta}\right], \tag{3.74}$$

$$B_\theta = \frac{B_r r}{V(\theta)} \omega(\theta, \phi) \sin\beta \sin\phi^*, \tag{3.75}$$

$$B_\phi = \frac{B_r r}{V(\theta)} \left[\omega(\theta, \phi) \sin\beta \cos\theta \cos\phi^* + \omega(\theta, \phi) \cos\beta \sin\theta - \Omega \sin\theta\right]. \tag{3.76}$$

3.9 Spacecraft View of the Generalised Fisk Field

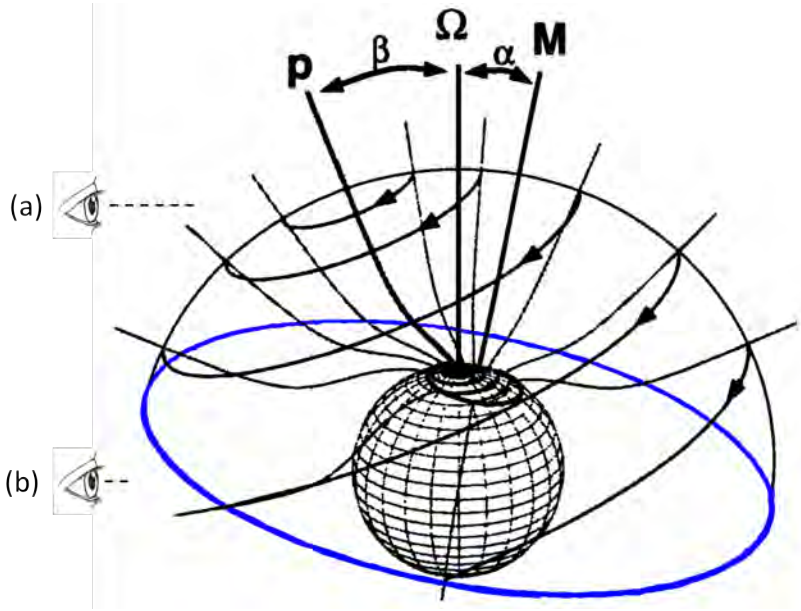

Figure 3.10: Footpoint trajectories on the source surface. Observer (a) is fixed at heliographic polar angle $\theta_{hg}^{ss} = 20°$ and observer (b) at $\theta_{hg}^{ss} = 80°$. Figure adapted from *Zurbuchen et al.* [1997].

Two observers are placed in Figure 3.10, one located at position (a) with $\theta_{hg}^{ss} = 20°$ and the other at position (b) with $\theta_{hg}^{ss} = 80°$. As the Sun rotates about $\vec{\Omega}$, observer (a) will only view the trajectories of the open magnetic field lines. The observer will also continuously detect different differential rotation periods as the Sun rotates, since different footpoint trajectories are intersected during the full $360°$ rotation. Using the transformations of Section 3.3, the magnetic field lines are traced from $\theta_{hg}^{ss} = 20°$ on the source surface to its corresponding θ_{hg}^{ph} on the photosphere where it rotates at its unique differential rotation period. This is shown in Figure 3.11a.

Observer (b) encounters field lines originating from within and from outside of the PCH boundary on the source surface (blue line) during one solar rotation. The generalised Fisk field assumes a pure Parker model for magnetic field lines originating from outside a PCH, implying $\omega(\theta, \phi) = 0$ for these field lines. Figure 3.11b shows the change in differential rotation rate observed by observer (b) when both classes of field lines are encountered.

The implication of this assumption is the generalised Fisk field will exhibit pure Fisk field behaviour only at high latitudes. With decreasing latitude, a mixture of Fisk-like and Parker-like field lines will be detected. When the equator is reached, pure Parker behaviour will be observed.

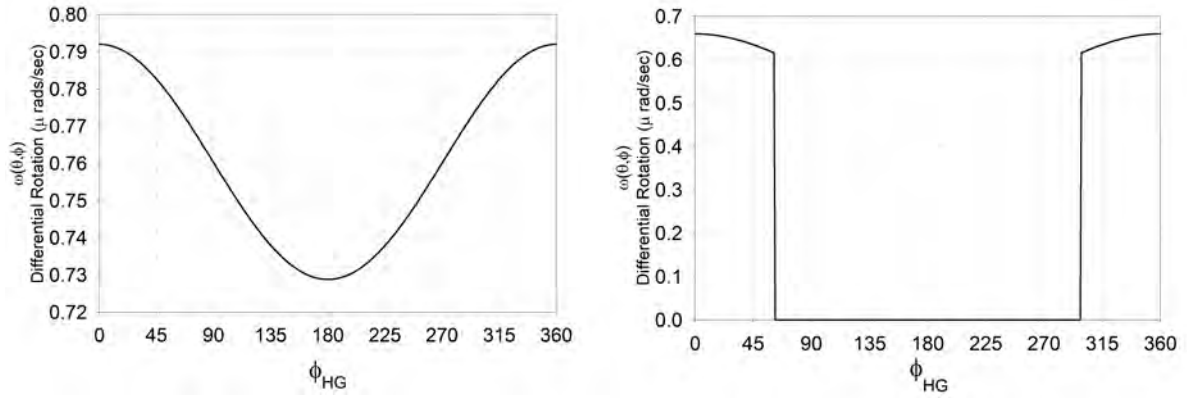

(a) $\theta_{hg}^{ss} = 20°$ (b) $\theta_{hg}^{ss} = 80°$

Figure 3.11: Observed differential rotation rate of the footpoint trajectories on the source surface at a constant heliographic polar angle while scanning through the azimuth.

3.10 Summary

In this chapter, the divergence-free generalised Fisk field model is presented. The assumption of a constant differential rotation rate on the photosphere was relaxed and subsequently this parameter now depends on both heliographic latitude and longitude. Transformations mapping field lines from the solar wind source surface back to the photosphere is presented for the first time. It is also shown that the final form of the generalised Fisk field equations are qualitatively similar to the Fisk field equations of *Zurbuchen et al.* [1997], with the only two differences being the spatial dependence of the differential rotation rate ω of the photosphere, and the latitudinally-dependent solar wind velocity.

Chapter 4

The Fisk-Parker Hybrid Heliospheric Magnetic Field

4.1 Introduction

The Fisk field has been notoriously difficult to implement in three-dimensional numerical cosmic-ray modulation codes due to its complicated mathematical structure compared with the Parker field model (see *Burger* [2005] for an overview). At high latitudes close to the pole of the photosphere where the magnetic field lines have their origins inside a polar coronal hole (PCH) and dragged out by the fast solar wind, the Fisk field equations of *Zurbuchen et al.* [1997] works well, but in the low-latitude and slow solar wind regions these equations break down. *Burger and Hitge* [2004] proposed a novel divergence-free Fisk-Parker hybrid heliospheric magnetic field that is easier to implement in a numerical modulation code while remaining a reasonable approximation to the physical heliospheric magnetic field (HMF). Since the footpoint trajectories of the Fisk-Parker hybrid field lines on the source surface are qualitatively similar to the trajectories discussed by *Fisk et al.* [1999a], the Fisk-Parker hybrid HMF model is a good approximation for both the case when field lines open into the heliosphere in the polar regions and at low latitudes close to the equator [*Burger and Hitge*, 2004].

This chapter addresses the fundamental structures and properties of the Fisk-Parker hybrid HMF model and its implications on the global understanding of the heliosphere. The crucial role of magnetic diffusion in a PCH and its impact on the magnetic footpoint transport processes on the photosphere is explored. A refined hybrid model is then considered to implement this HMF model throughout the entire solar activity cycle after which a short evaluation of its influence on the modulation of cosmic rays throughout the heliosphere is presented. A detailed derivation and validation of the Fisk-Parker heliospheric magnetic field model is shown for the first time. Note that a step-by-step derivation of a Fisk-type field, starting at the photosphere and ending at a point of observation in the heliosphere, is presented. In the current chapter published results are examined and addressed at the level that they were presented.

4.2 Derivation of the Fisk-Parker HMF Model

The Fisk-Parker hybrid heliospheric magnetic field is based on the assumption that such a field can be expressed as some combination of the Parker [*Parker*, 1958] HMF model and the Fisk [*Fisk*, 1996] HMF model. Mathematically, the following is being described:

$$A\vec{B_P} + C\vec{B_F} = \vec{B_H}, \tag{4.1}$$

where A and C are multi-variable functions multiplied with the Parker and Fisk magnetic field expressions, respectively, and $\vec{B_H}$ is the Fisk-Parker hybrid magnetic field expression (B is not a good choice for an undetermined function when dealing with magnetic fields). Accordingly, the following needs to be true:

$$\vec{\nabla} \cdot (A\vec{B_P} + C\vec{B_F}) = 0, \tag{4.2}$$

in order to ensure the divergence-free nature of the hybrid field. Using standard vector identities, Eq. 4.2 can be expanded and leads to the constraint

$$[(\nabla A) \cdot \vec{B_P} + A(\vec{\nabla} \cdot \vec{B_P})] + [(\nabla C) \cdot \vec{B_F} + C(\vec{\nabla} \cdot \vec{B_F})] = 0. \tag{4.3}$$

The standard Parker field has already been proved to be divergence-free and therefore the second term in Eq. 4.3 is equal to zero. The same is true for the Fisk field and thus the last term of Eq. 4.3 is also equal to zero leading to

$$[\vec{B_P} \cdot (\vec{\nabla} A)] + [\vec{B_F} \cdot (\vec{\nabla} C)] = 0. \tag{4.4}$$

The next stage of this proof is to solve functions A and C in terms of each other. This is done by rearranging Eq. 4.4 and using the standard definition of the mathematical del operator in spherical coordinates. Hence, Eq. 4.4 expands to

$$\vec{B_P} \cdot \left(\frac{\partial A}{\partial r}\hat{r} + \frac{1}{r}\frac{\partial A}{\partial \theta}\hat{\theta} + \frac{1}{r\sin\theta}\frac{\partial A}{\partial \phi}\hat{\phi} \right) = -\vec{B_F} \cdot \left(\frac{\partial C}{\partial r}\hat{r} + \frac{1}{r}\frac{\partial C}{\partial \theta}\hat{\theta} + \frac{1}{r\sin\theta}\frac{\partial C}{\partial \phi}\hat{\phi} \right). \tag{4.5}$$

Eq. 4.5 can be greatly simplified by making a few crucial assumptions. Firstly, the radial component of the Fisk-Parker hybrid magnetic field does not distinguish between influences due to the respective radial components of the Fisk and Parker fields. In other words, as a magnetic field line propagate through the heliosphere, the field line will not change from Parker to Fisk behaviour in the radial direction since the same radial magnetic field component is assumed for the Parker, Fisk and Fisk-Parker hybrid magnetic field models. Therefore, any terms involving the rate of change of a function in terms of the radial direction is equal to zero; consequently, the first terms in brackets on both sides of Eq. 4.5 are eliminated. Secondly, the Parker field has no meridional component and accordingly the second term in the first bracket is also equal to zero. These two assumptions bring about the following changes:

$$\left(B_{P_\phi} \cdot \frac{1}{r\sin\theta}\frac{\partial A}{\partial \phi}\right) = -\left[\left(B_{F_\theta} \cdot \frac{1}{r}\frac{\partial C}{\partial \theta}\right) + \left(B_{F_\phi}\frac{1}{r\sin\theta}\frac{\partial C}{\partial \phi}\right)\right] \tag{4.6}$$

where B_{P_ϕ}, B_{F_ϕ}, and B_{F_θ} are the azimuthal components of the Parker and Fisk fields, respectively, and the meridional component of the Fisk field. Substituting the respective magnetic field components into Eq. 4.6 leads to

$$\begin{aligned}\frac{B_r r}{V_{SW}}(-\Omega\sin\theta)\frac{1}{r\sin\theta}\frac{\partial A}{\partial \phi} = &-\frac{B_r r}{V_{SW}}\omega\sin\beta\sin\phi\frac{1}{r}\frac{\partial C}{\partial \theta} \\ &-\frac{B_r r}{V_{SW}}[\omega\sin\beta\cos\theta\cos\phi + \sin\theta(\omega\cos\beta - \Omega)]\frac{1}{r\sin\theta}\frac{\partial C}{\partial \phi}\end{aligned} \tag{4.7}$$

which simplifies to

$$\frac{\partial A}{\partial \phi} = \frac{\omega}{\Omega}\sin\beta\sin\phi\frac{\partial C}{\partial \theta} + \frac{\omega}{\Omega}\sin\beta\frac{\cos\theta}{\sin\theta}\cos\phi\frac{\partial C}{\partial \phi} + \frac{\omega}{\Omega}\cos\beta\frac{\partial C}{\partial \phi} - \frac{\partial C}{\partial \phi}. \tag{4.8}$$

Studying Eq. 4.8 two important features are noted. Firstly, A and C are two unknown functions in one equation which suggests they cannot be solved uniquely if no other information is available. So, secondly, certain assumptions about the form and structure of A and C should be made in order to continue. The first step is to choose their functional dependencies. A few possibilities are presented below after which the validity of each one will be discussed.

1. $A = A(\theta)$ and $C = C(\theta) \implies A \neq A(\phi)$ and $C \neq C(\phi)$
2. $A = A(\phi)$ and $C = C(\phi) \implies A \neq A(\theta)$ and $C \neq C(\theta)$
3. $A = A(\theta)$ and $C = C(\phi) \implies A \neq A(\phi)$ and $C \neq C(\theta)$
4. $A = A(\phi)$ and $C = (\theta) \implies A \neq A(\theta)$ and $C \neq C(\phi)$

More possibilities are available (e.g. $A = A(\theta, \phi)$ etc.), but the implications of the aforementioned will be discussed and altered as needed. Option 1 suggests the left hand side of Eq. 4.8 reduces to zero since $\partial A/\partial\phi = 0$ if A is only polar-angle dependent, while only the first term on the right hand side remains since $\partial C/\partial\phi = 0$ if C is also only polar-angle dependent. Consequently, Eq. 4.8 reduces to

$$0 = \frac{\omega}{\Omega}\sin\beta\sin\left(\phi + \frac{\Omega r}{V_{SW}}\right)\frac{\partial C(\theta)}{\partial \theta} \tag{4.9}$$

At first glance, there are a few challenges with this choice of A and C. Firstly, A has now been eliminated from the equation. Although this implies only one unknown function (C) and one equation, no other information about the structure of A can now be extracted from the expression except for the initial assumption, $A = A(\theta)$. One could then be tempted to assume C has the same structure as A, but this is not mathematically satisfactory. Secondly, in order for Eq. 4.9 to be true, further assumptions need to be made. Either the differential rotation rate

must be switched off ($\omega = 0$), implying a pure Parker field, or $\beta = 0$, implying a zero-valued tilt angle ($\alpha = 0$), again suggesting a pure Parker field during deep solar minimum conditions. Another way is to assume the term in brackets should equal zero. This, in turn, can only be achieved at one azimuthal location, $\phi = 0$, and at $r = 0$, which is not physical. The only option left is to assume $\partial C/\partial\theta = 0$, but this cannot be true since $C = C(\theta)$ was explicitly assumed. Clearly, Option 1 does not aid in the progression of this argument.

Option 2 involves keeping the left hand side of Eq. 4.8 intact and eliminating only the first term on the right hand side. In order to solve A in terms of C, Eq. 4.8 is integrated with respect to ϕ, making the reasonable assumption that ω, Ω and β are all independent of ϕ, leading to

$$\begin{aligned} A(\phi) &= C(\phi)\frac{\omega}{\Omega}\sin\beta\frac{\cos\theta}{\sin\theta}\cos\phi + C(\phi)\frac{\omega}{\Omega}\cos\beta - C(\phi) \\ \implies A(\phi) &= C(\phi)\left[\frac{\omega}{\Omega}(\sin\beta\frac{\cos\theta}{\sin\theta}\cos\phi + \cos\beta) - 1\right]. \end{aligned} \tag{4.10}$$

After first inspection, it should be noted that Eq. 4.10 points to a direct contradiction in terms of the assumptions made. It was assumed that A is a function of ϕ only and not θ. The right hand side of Eq. 4.10 contains meridional terms leading to the contradiction. Therefore, Option 2 is rejected.

Option 3 entails the elimination of the left hand side of Eq. 4.8 together with the first term on the right hand side. Furthermore, integrating with respect to ϕ gives the following form:

$$\begin{aligned} 0 &= \frac{\omega}{\Omega}\sin\beta\frac{\cos\theta}{\sin\theta}\cos\phi\frac{\partial C(\phi)}{\partial\phi} + \frac{\omega}{\Omega}\cos\beta\frac{\partial C(\phi)}{\partial\phi} - \frac{\partial C(\phi)}{\partial\phi} \\ \implies \frac{\partial C(\phi)}{\partial\phi} &= \frac{\omega}{\Omega}\sin\beta\frac{\cos\theta}{\sin\theta}\cos\phi\frac{\partial C(\phi)}{\partial\phi} + \frac{\omega}{\Omega}\cos\beta\frac{\partial C(\phi)}{\partial\phi} \\ \implies C(\phi) &= C(\phi)\frac{\omega}{\Omega}\sin\beta\frac{\cos\theta}{\sin\theta}\cos\phi + C(\phi)\frac{\omega}{\Omega}\cos\beta \\ \implies 0 &= C(\phi)\left[1 - \frac{\omega}{\Omega}(\sin\beta\frac{\cos\theta}{\sin\theta}\cos\phi - \cos\beta)\right] \end{aligned} \tag{4.11}$$

Similar to Option 1, the reduction to zero of the left hand side eliminates A from the expression. Also, the only way for Eq. 4.11 to be true is when either $C = 0$ or the term enclosed within the large brackets equals zero. Both these options do not facilitate the process of finding the relationship between A and C to eventually find the magnetic field expressions of the Fisk-Parker hybrid magnetic field. This leaves only Option 4.

This last option requires the assumption that $A = A(\phi)$ and $C = C(\theta)$ resulting in

$$\frac{\partial A(\phi)}{\partial\phi} = \frac{\omega}{\Omega}\sin\beta\sin\phi\frac{\partial C(\theta)}{\partial\theta} \tag{4.12}$$

Before integrating both sides of Eq. 4.12, consider the function C for a moment. The function C can be described as $C = f(\theta)$ where $f(\theta)$ is a function depending on θ only. To ensure there is no hemispherical discrimination, meaning there is no magnetic field sign (positive or negative)

change when a magnetic field lines crosses the magnetic equator, it would be advantageous to choose $f(\theta)$ to be $C = f(\theta)^2$. Then Eq. 4.12 leads to

$$\frac{\partial A(\phi)}{\partial \phi} = \frac{\omega}{\Omega} \sin\beta \sin\phi \left(2f(\theta) \frac{\partial f(\theta)}{\partial \theta} \right). \tag{4.13}$$

Next, integrating over ϕ gives

$$A(\phi) = -\frac{\omega}{\Omega} \sin\beta \cos\phi \left(2f(\theta) \frac{\partial f(\theta)}{\partial \theta} \right). \tag{4.14}$$

Scrutinising Eq. 4.14, a contradiction is identified. The initial assumption was $A = A(\phi) \neq A(\theta)$ and this is not the case above. Since all the other options have failed, an extension of the initial assumption can be considered, for instance, assume $A = A(\theta, \phi)$. By making this assumption, it opens the door to ask whether all possible options listed above could also work in principle if they were to be dependent on both parameters, θ and ϕ. It can be shown that assuming $A = A(\theta, \phi)$ and $C = C(\theta)$ is the only assumption that does not lead to a contradiction of previous assumptions. Now, assuming A has the form presented in Eq. 4.14 and $C = f(\theta)^2$, all the restrictions put on these two function are fulfilled. To simplify the notation from hence forward, assume the following conventions:

$$\begin{aligned} F_S &= C(\theta) = f(\theta)^2, \\ \frac{\partial F_S}{\partial \theta} &= \frac{\partial f(\theta)^2}{\partial \theta} = 2f(\theta) \frac{\partial f(\theta)}{\partial \theta}, \end{aligned} \tag{4.15}$$

where F_S will from here on forward be referred to as the transition function of the Fisk-Parker hybrid field. This function will dictate the transition from Parker to Fisk behaviour. The next step is to extract the Fisk-Parker hybrid magnetic field equations in spherical coordinates from Eq. 4.2 by using the functional form of A and C and confirming that this new-found field is divergence-free as it should of course be by construction.

As previously mentioned, the Fisk-Parker hybrid HMF model does not discriminate between Parker and Fisk behaviour in the radial direction, therefore its radial component is given by

$$B_r = B_0 \left(\frac{r_0}{r} \right)^2. \tag{4.16}$$

Secondly, using Eq. 4.2, and separating the meridional component from the azimuthal component, the former is calculated as follows:

$$B_\theta = A B_{P_\theta} + C B_{F_\theta}. \tag{4.17}$$

Since the Parker field has no θ-component, the first term of Eq. 4.17 falls away. Substituting $C = F_S$ and the θ-component from the Fisk field leads to

$$B_\theta = B_r r \frac{\omega F_S}{V_{SW}} \sin\beta \sin\phi. \tag{4.18}$$

The calculation of the azimuthal component is similar to the meridional component by using the expression in Eqs. 4.14 and 4.15 together with the ϕ-components of both the Parker and Fisk fields:

$$\begin{aligned} B_\phi &= AB_{P_\phi} + CB_{F_\phi} \\ B_\phi &= -\frac{B_r r}{V_{SW}}\Omega \sin\theta \left(-\frac{\omega}{\Omega}\sin\beta\cos\phi\frac{\partial F_S}{\partial\theta}\right) \\ &\quad + \frac{B_r r}{V_{SW}}\left[\omega\sin\beta\cos\theta\cos\phi + \sin\theta(\omega\cos\beta - \Omega)\right]F_S. \end{aligned} \tag{4.19}$$

After some simplifications, the final form of the azimuthal component of the Fisk-Parker hybrid magnetic field is

$$B_\phi = B_r\frac{r}{V_{SW}}\left[\omega F_S\sin\beta\cos\theta\cos\phi + \sin\theta(\omega F_S\cos\beta - \Omega) + \omega\frac{dF_s}{d\theta}\sin\beta\sin\theta\cos\phi\right]. \tag{4.20}$$

Before Eqs. 4.16, 4.18, and 4.20 can be deemed the final form of the Fisk-Parker hybrid magnetic field equations, its divergence-free nature in spherical coordinates should be confirmed. Accordingly, the following expression should be corroborated:

$$\vec{\nabla}\cdot\vec{B_H} = \frac{1}{r^2}\frac{\partial}{\partial r}(r^2 B_{H_r}) + \frac{1}{r\sin\theta}\frac{\partial}{\partial\theta}(B_{H_\theta}\sin\theta) + \frac{1}{r\sin\theta}\frac{\partial}{\partial\phi}(B_{H_\phi}) = 0, \tag{4.21}$$

where B_{H_r}, B_{H_θ}, and B_{H_ϕ} are the radial, meridional and azimuthal components of the Fisk-Parker hybrid field from Eqs. 4.16, 4.18, and 4.20, respectively. To verify whether Eq. 4.21 is correct, the three terms will be calculated separately. The first term on the right-hand side yields

$$\begin{aligned} \frac{1}{r^2}\frac{\partial}{\partial r}(r^2 B_{H_r}) &= \frac{1}{r^2}\frac{\partial}{\partial r}\left(\frac{r^2 B_0 r_0^2}{r^2}\right) \\ &= \frac{B_0 r_0^2}{r^2}\frac{\partial}{\partial r}(1) \\ &= 0. \end{aligned} \tag{4.22}$$

Now, turning to the meridional component, it follows that

$$\begin{aligned} \frac{1}{r\sin\theta}\frac{\partial}{\partial\theta}(B_{H_\theta}\sin\theta) &= \frac{1}{r\sin\theta}\frac{\partial}{\partial\theta}\left(B_r\frac{\omega F_S}{V_{SW}}\sin\beta\sin\theta\sin\phi\right) \\ &= \frac{B_r r\omega\sin\beta\sin\phi}{V_{SW} r\sin\theta}\frac{\partial}{\partial\theta}(F_S\sin\theta) \\ &= \frac{B_r\omega\sin\beta\sin\phi}{V_{SW}\sin\theta}\left(F_S\cos\theta + \frac{\partial F_S}{\partial\theta}\sin\theta\right) \end{aligned} \tag{4.23}$$

Next, the azimuthal component is checked.

$$\begin{aligned}\frac{1}{r\sin\theta}\frac{\partial}{\partial\phi}(B_{H_\phi}) &= \frac{1}{r\sin\theta}\frac{\partial}{\partial\phi}\Bigg\{B_r\frac{r}{V_{SW}}\big[\omega F_S\sin\beta\cos\theta\cos\phi \\ &\qquad + \sin\theta(\omega F_S\cos\beta-\Omega)+\omega\frac{dF_s}{d\theta}\sin\beta\sin\theta\cos\phi\big]\Bigg\} \\ &= \frac{B_r r}{r\sin\theta V_{SW}}\Bigg[\omega F_S\sin\beta\cos\theta\left(\frac{\partial}{\partial\phi}\cos\phi\right) \\ &\qquad + \omega\frac{dF_S}{d\theta}\sin\beta\sin\theta\left(\frac{\partial}{\partial\phi}\cos\phi\right)\Bigg] \\ &= \frac{B_r}{\sin\theta V_{SW}}\left[-\omega F_S\sin\beta\cos\theta\sin\phi-\omega\frac{dF_S}{d\theta}\sin\beta\sin\theta\sin\phi\right]\end{aligned} \tag{4.24}$$

Substituting the calculated values of Eqs. 4.22, 4.23, and 4.24 into Eq. 4.21 proves the divergence-free nature of the Fisk-Parker hybrid heliospheric magnetic field. Not only has the divergence-free nature of the field been verified, but the uniqueness of the magnetic field equations have also been established for the first time. The only way to uniquely solve the unknown functions A and C is to assume $A = A(\theta,\phi)$ and $C = C(\theta)$. It has been shown here that any other combination results in either the trivial or a non-physical solution.

4.3 The Structure of the Fisk-Parker Hybrid HMF

Typical numerical cosmic-ray modulation codes prefer spherical heliographic coordinates. Consequently, the PCHs in the Fisk-Parker hybrid HMF model are assumed to be symmetric about the rotational axis $\vec{\Omega}$ and not about the magnetic axis $\vec{M}$, as proposed by the original Fisk field (see *Fisk* [1996], *Hattingh* [1998], *Burger and Hitge* [2004]). Due to this change in symmetry, the footpoint velocity equations of the Fisk field are now described in terms of heliographic instead of heliomagnetic coordinates, advantageous for numerical models in spherical coordinates.

The photospheric origin of the hybrid field includes the considerations of the position of PCHs and the expected field-type at the solar equator and poles. PCHs do not traverse far into the slow solar wind speed regions on the photosphere, since its origin is past the boundary of the PCH itself where the plasma can escape the confining effect of coronal loop structures [*Krüger*, 2005]. Outside of the PCH, closer to the lower-latitude, equatorial regions, the photosphere rotate rigidly at an near-equatorial rotation period and thus a Parker field is a justifiable assumption in this region [*Burger and Hitge*, 2004]. This forms the foundation of assuming a Parker field at the solar equator for the hybrid field. Whether the solar poles rotate differentially is a contested issue. *Fisk* [1996] suggested that it is not clear whether differential rotation is valid up to the highest latitudes and model results should not be trusted in this region [*Schou et al.*, 1998]. Hence, it is assumed the polar regions of the photosphere also rotate rigidly and for this reason a Parker field can be assumed to originate from this zone as well.

The Fisk-Parker hybrid field, therefore, is a HMF model that exhibits Parker-like behaviour in the low-latitudes equatorial region, then transitions to Fisk-like behaviour during the mid- to high-latitudes region where the PCHs are situated, and finally a transition back to Parker-like

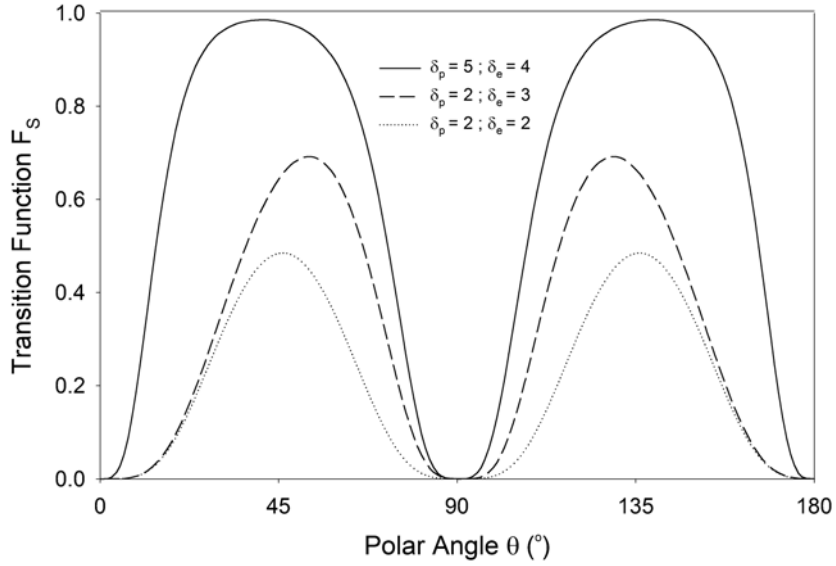

Figure 4.1: Transition function which is multiplied into the Fisk HMF to simplify its implementation into a numerical modulation code. At the solar poles ($\theta = 0°, 180°$) and at the equator ($\theta = 90°$) the function equals zero where it also reduces to a pure Parker field. The different chosen values for δ_p and δ_e determines how fast or how slow the transition from Parker to Fisk takes place.

behaviour is expected at the solar poles. To force the transitions from the one HMF model to the other, a latitude-dependent transition function is incorporated in the magnetic field expressions for the Fisk-Parker hybrid field. This transition function is given by ([*Krüger*, 2005], [*Burger et al.*, 2008])

$$F_S = \tanh[\delta_p \theta] + \tanh[\delta_p(\theta - \pi)] - \tanh[\delta_e(\theta - \pi/2)]^4 \tag{4.25}$$

where the constants δ_p and δ_e determine how fast the transition from Fisk to Parker is made at the pole and equator, respectively, while θ denotes the polar angle. The first term of Eq. 4.25 describes the behaviour at the northern solar pole, the second term the southern solar pole, and the last term the behaviour at the equator. Figure 4.1 shows the profile of the transition function for different chosen values for δ_p and δ_e. At the equator and at both the northern and southern solar poles the transition function equals zero to mimic the expected Parker field.

When δ_p is greater than δ_e, as in the case of the solid line in Figure 4.1, the transition from Parker to Fisk happens closer to the poles. For this case, the maximum Fisk effect is seen at $\theta = 41°$ for the northern solar hemisphere, and again at $\theta = 139°$ for the southern solar hemisphere. In general, with decreasing δ values, the total Fisk-field effect on the Fisk-Parker hybrid field is diminished. For the case when $\delta_e > \delta_p$, the latitude position of maximum Fisk effect is delayed and occurs closer to the equator, and when $\delta_e = \delta_p$, this happens exactly halfway between the solar pole and equator.

Finally, after including the transition function F_S, the components of the divergence-free Fisk-Parker hybrid HMF model in heliographic spherical coordinates (r,θ,ϕ), as derived in Section 4.2, are then given by

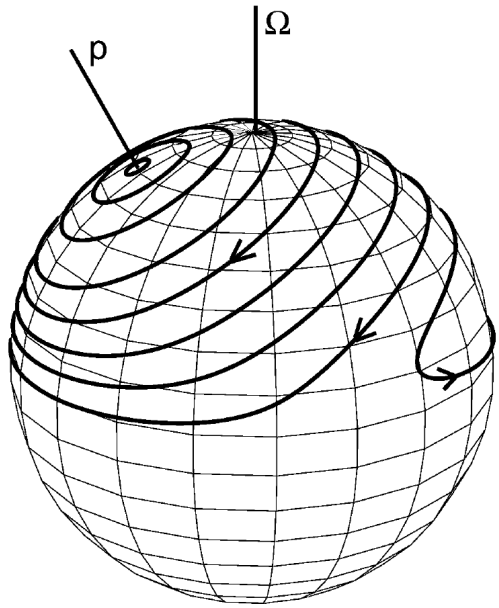

Figure 4.2: Footpoint trajectories on the solar wind source surface in the co-rotating frame at the equatorial rotation period of the Sun. The angle between the rotational axis $\vec{\Omega}$ and the virtual $\vec{p}$-axis is set at $\beta = 30°$. Note that the trajectories symmetric about the $\vec{p}$-axis have the same clockwise direction of travel, while the trajectory in the so-called return region on the far right has the opposite direction of travel. This figure is adapted from [*Burger and Hitge*, 2004].

$$
\begin{aligned}
B_r &= A\left(\frac{r_0}{r}\right)^2 \\
B_\theta &= B_r \frac{r\omega F_S}{V_{SW}} \sin\beta \sin\phi \\
B_\phi &= B_r \frac{r}{V_{SW}} \left[\omega F_S \sin\beta \cos\theta \cos\phi + \sin\theta(\omega F_S \cos\beta - \Omega) + \omega \frac{dF_s}{d\theta} \sin\beta \sin\theta \cos\phi\right]
\end{aligned}
\tag{4.26}
$$

where all symbols have their usual meaning as first presented in [*Burger and Hitge*, 2004]. These magnetic field equations can easily be generalised for a latitudinally-dependent solar wind speed [*Schwadron*, 2002]. Considering Figure 4.1 together with the hybrid magnetic field expressions, it is clear when $F_S \approx 1$ at mid-latitudes, the magnetic field reduces to those presented by *Zurbuchen et al.* [1997], and when $F_S \approx 0$ at the poles and the equator, the field reduces to the standard Parker field [*Parker*, 1958]. Note the only constraint put on the transition function to keep the Fisk-Parker hybrid field divergence-free, is that should depend only on latitude [*Burger and Hitge*, 2004]. Also, note when the differential rotation ω is set equal to zero and $\beta = 0$, as in the case of the Parker field, the hybrid field does indeed reduces to the standard Parker field. The polar and azimuthal components of the divergence-free footpoint velocity field in the co-rotating frame giving rise to the Fisk-Parker hybrid HMF are [*Burger and Hitge*, 2004]

$$
\begin{aligned}
u_\theta &= r\omega F_S \sin\beta \sin\phi \\
u_\phi &= r\omega \left(F_S \sin\beta \cos\theta \cos\phi + F_S \cos\beta \sin\theta + \frac{dF_S}{d\theta} \sin\beta \sin\theta \cos\phi\right).
\end{aligned}
\tag{4.27}
$$

A graphical illustration of the footpoint velocity field on the source surface shown in Figure 4.2 with $\beta = 30°$, $\omega = \frac{\Omega}{4}$, $\delta_p = 5.0$, and $\delta_e = 4.0$. The resultant β value was calculated utilising the geometry of a PCH with $\theta_{mm} = 24°$, $\theta'_{mm} = 75°$ and a tilt angle $\alpha = 15°$, just as the setup of *Fisk* [1996]. A few important points are worth mentioning before continuing.

Firstly, note the symmetry about the rotational equator in Figure 4.2. The footpoint trajectories will not cross the rotational equator because the transition function causes the field to behave purely Parker-like in the equatorial region. Secondly, the footpoint trajectories will become very distorted at the poles due to the slowing rotation rate of the source surface due to the transition function causing the field to become Parker-like again. Therefore, a Fisk field is assumed at the poles; returning a $F_S = 1$ value when only the last term of Eq. 4.25 is used in the polar region. Thus, the footpoint velocity field put forward by *Fisk et al.* [1999a] is qualitatively similar to that of the hybrid field in Figure 4.2 with the only geometrical difference being the symmetry of the PCHs. When the polar angle θ approaches the solar equator, the transition function F_S tends to zero rendering the influence of u_θ negligible while u_ϕ dominates since $dF/d\theta$ increases. At the solar equator $dF/d\theta = F_S = 0$ and the footpoint velocity becomes zero.

The so-called return region on the right of Figure 4.2 is due to diffusive reconnection. The direction of travel of the footpoints are anti-clockwise in the return region which is opposite to that of the near-circular trajectories outside the return region. This region is characterised by a distorted trajectory where magnetic field footpoints return to the other side of the Sun. The trajectories in the return region are closer spaced than the other trajectories, but this should not be confused with a higher magnetic field density. In order to maintain a constant magnetic field density, the rotation period of the magnetic field lines in this region are much slower.

4.4 Magnetic Diffusion and Different Transport Processes

Since the Fisk-Parker hybrid field deals with both open and closed magnetic field lines, special care needs to be taken when a magnetic field line crosses a PCH boundary. Magnetic diffusion plays an important role in Fisk-type fields when approaching the boundary and inside of a PCH. Several different transport processes are responsible for this magnetic diffusion and a few will be discussed in this section. *Krüger* [2005] shows a complete study concerning several different transport and diffusion mechanisms present on the photosphere and a few of these processes and their implications will be highlighted here.

Supergranulation and the emergence of new magnetic flux are the two dominant convection-related diffusion processes inside a PCH with an estimated diffusion speed of $\sim 0.2-0.3$ km/s. The former is independent of solar activity to a good first approximation and materializes everywhere on the photosphere except inside sunspots. The latter is a diffusion process suggested by *Fisk et al.* [1999b] that is connected to supergranulation, but dominates the actual supergranular diffusion. This process is characterized by magnetic footpoints travelling from the centre of a supergranule to its edge where magnetic tension is increased. The magnetic footpoint then reconnects with an open field line after the tension is released. Once magnetic footpoints leave the polar coronal hole, reconnection diffusion becomes the leading transport process with an

estimated diffusion speed of ~ 0.7 km/s. Differential rotation, a virtually stable transport process on the photosphere, plays a key role as an overshadowing diffusion process on large time and length scales.

Polar coronal holes are extremely dynamic photopsheric phenomena and their boundaries cannot be pinned down or predicted to a reasonable level. One would expect smooth transition of an open magnetic field line inside a PCH to the outside and subsequently observe a transition from Fisk to Parker behaviour. But, because of the ragged boundaries of the PCHs, a rather rapid and random reconnection is expected to be present over a range of latitudes in the vicinity of the boundary. Therefore, a stationary observer monitoring this range of latitudes will see a mixture of turbulent Fisk- and Parker fields.

After considering the influence of several diffusion and transport processes on the photosphere, the next step is to investigate its implications on the solar wind source surface. Consider the area around the $\vec{p}$-axis on the source surface of Figure 4.2. Magnetic field lines in this area map back to the polar region on the photosphere where random convection diffusion prevails and hence a Parker magnetic field is expected. Now, consider an area around the rotational axis $\vec{\Omega}$ on the photosphere. Again, a Parker magnetic field is expected in this region due to the slow moving footpoints close to the pole ($\omega \to 0$). Now evaluate the corresponding footpoint trajectories on the source surface such that $\vec{\Omega}$ is enclosed in the trajectories. Since a stationary observer will see a small area around $\vec{\Omega}$ to still remain Parker-like, it is reasonable to assume that the field becomes more Parker-like towards $\vec{\Omega}$ on the source surface. Moving away from $\vec{p}$ and $\vec{\Omega}$ where differential rotation dominates on large scale as a diffusion process inside the PCH, significant Fisk-like behaviour is expected on the source surface where the trajectories have a larger polar component. When approaching the boundary of the polar coronal hole, reconnection diffusion overtakes differential rotation as the dominant diffusion process resulting in a mixture of Parker and Fisk behaviour where the trajectories on the source surface show less meridional motion. As the magnetic footpoint leaves the PCH, reconnective diffusion increases. Here the azimuthal component of the field becomes Parker-like. At the rotational equator, the motion on the source surface can only be diffusive and the field Parker-like.

During solar maximum conditions, PCHs are known to be become much smaller and the boundaries highly irregular in time and position. The amount of diffusion is expected to increases during these conditions due to the amount of active regions also increasing and only a small amount of Fisk-like behaviour is expected.

Krüger [2005] discusses the divergence-free nature of the footpoint velocity field of the Fisk-Parker hybrid field and asks the valid question whether this velocity field could really be divergence-free especially when considering the return region where trajectories are not closed over the entire source surface. *Krüger* [2005] goes on to motivate the divergence-free nature of the velocity field by comparing the footpoints to water droplets flowing in a container (random diffusive motion) and flowing through a pipe connected to the container (coherent motion) and draws the conclusion that magnetic flux will always be conserved (see *Krüger* [2005] Section 5.2.3 and *Figure* 5.1). In other words, just as one water droplet enters the pipe at the one end and another water droplet leaves the pipe on its opposite end, a magnetic footpoint leaving the PCH will be replaced by another footpoint from another location such that magnetic flux is

conserved. Note that conservation of flux does not imply that every magnetic footpoint traces out a closed trajectory, but rather describes the condition that as one enters, another exits.

4.5 An Advancement Towards an Improved Hybrid HMF Model

The Fisk-Parker hybrid field discussed in Section 4.3 is based on the assumption that ordered magnetic field footpoint motions on the solar wind source surface continue up to the solar rotational equator resulting in a Fisk-Parker hybrid heliospheric field at all latitudes [*Burger et al.*, 2008]. Improving the hybrid model involves assuming ordered footpoint motion only occurs at higher latitudes and diffusive reconnection of magnetic field lines dominate close to the rotational equator. Consider Figure 4.3a. As previously mentioned, the PCHs are assumed to be symmetric about the rotational axis $\vec{\Omega}$ in the original hybrid field and not the magnetic axis $\vec{M}$ as is the case in the Fisk field. This assumption still applies in the refined hybrid field and the PCH is indicated on the photosphere (shaded region) in Figure 4.3a. Due to the superradial expansion of the magnetic field, the mapped region will not be symmetric about $\vec{\Omega}$ on the source surface. The dashed line labelled III indicates the minimum latitude at which ordered footpoint motion can occur and leads to a Parker-type field. Between III and the rotational equator, a Parker field is also assumed. Between labels II and III, one would expect a mixture of diffusive reconnection and ordered footpoint motion which leads to a Fisk-type field [*Kobylinski*, 2001]. Considering the high-latitude regions, no differential rotation is assumed to occur close to the poles (see *Schou et al.* [1998] for a full discussion of the validity of this assumption). The PCH on the photosphere maps out to the source surface in a region where one would expect footpoint motion to occur mainly via diffusive reconnection, and to another region where ordered motion prevails. This region is indicated by the dashed line labelled I in Figure 4.3a. Therefore, magnetic field lines originating from the pole of the Sun to latitude I have a mixture of Parker and Fisk-type fields after which a pure Fisk field is expected between I and II.

In order to include the effects of the aforementioned diffusion at different latitudes effectively, a new, refined transition function is necessary. Eq. 4.28 shows the new transition function to model this complicated meridional dependent situation and is graphically illustrated in Figure 4.3b where, as previously, δ_p and δ_e are the parameters used to control the transition from predominantly Fisk-type to Parker type fields at the poles and equator, respectively. Also, θ_b' denotes the minimum latitude where ordered footpoint motion can occur. Field lines originating from within the polar coronal hole are Fisk-like, and therefore the transition function will be greater than zero. Approaching either the solar- pole or equator, the field becomes more Parker-like and the transition function becomes zero. Furthermore, the transition from Parker to Fisk behaviour is much more gradual since the transition from differential rotation to diffusion as transport process is not abrupt:

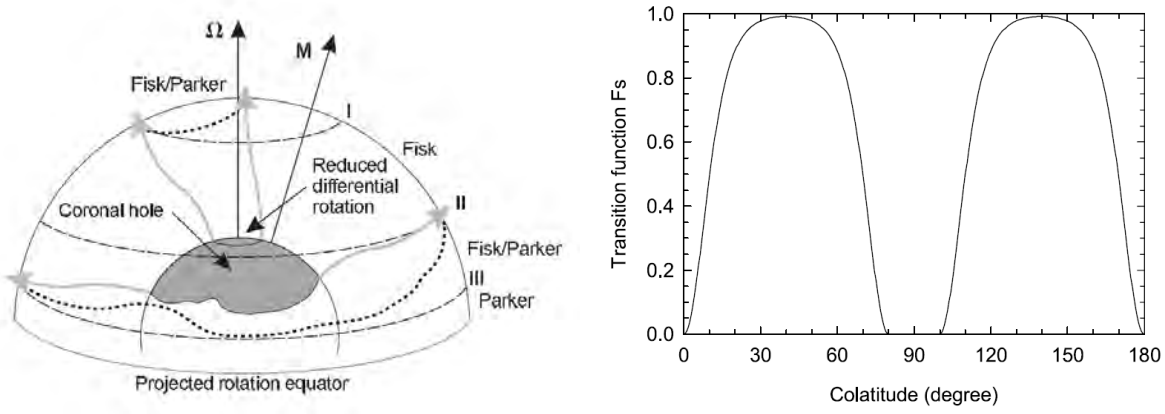

(a) (b)

Figure 4.3: (a): Graphical illustration of magnetic field lines mapping from the photosphere to the source surface. The dotted line on the source surface close to the pole is the region with little to no differential rotation. The dotted line in the equatorial region of the source surface shows the actual boundary of the edge of the PCH mapped from the photosphere. The different latitude regions are described in the text. (b): The new transition function of the refined hybrid HMF model as a function of colatitude. In this scenario, $\theta_b' = 80^\circ$ which is the maximum colatitude to where the Fisk field influence occurs. See *Krüger* [2005] for a transition function with $\theta_b' = 60^\circ$ (both figures adapted from *Burger et al.* [2008]).

$$F_s = \begin{cases} \{\tanh[\delta_p\theta] + \tanh[\delta_p(\theta-\pi)] - \tanh[\delta_e(\theta-\theta_b')]\}^2 & \text{if } 0 \le \theta < \theta_b' \\ 0 & \text{if } \theta_b' \le \theta \le \pi - \theta_b' \\ \{\tanh[\delta_p\theta] + \tanh[\delta_p(\theta-\pi)] - \tanh[\delta_e(\theta-\pi+\theta_b')]\}^2 & \text{if } \pi - \theta_b' < \theta \le \pi \end{cases} \tag{4.28}$$

For this improvement of the transition function to be reflected in the velocity field of *Burger and Hitge* [2004], a few modifications are in order. Firstly, it is assumed that the Parker field is not influenced by differential rotation. Accordingly, the angle β and ω should scale with F_S in order to ensure both these parameters equal zero at the solar equator and poles. Therefore, they are multiplied by F_S to give the following latitude-dependent functions:

$$\begin{aligned} \beta^*(\theta) &= \beta F_S(\theta) \\ \omega^*(\theta) &= \omega F_S(\theta) \end{aligned} \tag{4.29}$$

where β is calculated using the tilt angle α together with the size of the PCH, and $\omega = \Omega/4$. Both α and β are treated as constant values. The exact relationship between β and α will be shown and discussed later in this section. The new divergence-free velocity field equations of the refined hybrid HMF model in the co-rotating frame are given by the following expressions with θ and ϕ denoting the heliographic colatitude and azimuth, respectively, while r_0 expresses the radius of the source surface, and ω the differential rotation rate:

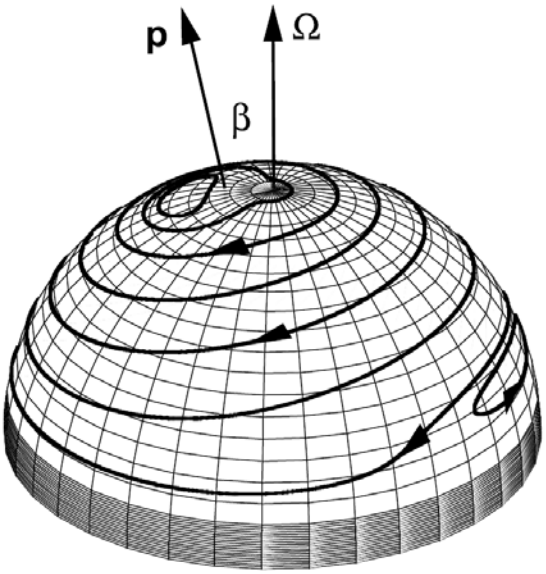

Figure 4.4: Footpoint trajectories on the source surface in the co-rotating frame of the refined hybrid HMF model. The clockwise direction of travel of the footpoints is indicated by arrows, while the counterclockwise direction of travel is indicated in the return region. The angle (β) between the rotational axis $\vec{\Omega}$ and the virtual $\vec{p}$-axis is also shown. In the shaded region bordering the solar equator only random motion of the footpoints are present (figure adapted from *Burger et al.* [2008]).

$$\begin{aligned} u_\theta &= r_0\omega^* \sin\beta^* \sin\phi \\ u_\phi &= r_0(\omega^* \sin\beta^* \cos\theta\cos\phi + \omega^* \cos\beta^* \sin\theta + \frac{d\omega^*}{d\theta}\sin\beta^* \sin\theta\cos\phi \\ &\quad + \omega^* \frac{d\beta^*}{d\theta}\cos\beta^* \sin\theta\cos\phi) \end{aligned} \tag{4.30}$$

Note, in order for the velocity field to remain divergence-free, the transition function F_S should only depend on θ which will also ensure the divergence-free nature of the subsequent magnetic field equations derived from the velocity field. Figure 4.4 is a graphical illustration of the trajectories of the magnetic footpoints on the source surface using $\alpha = 12°$, $\omega = \Omega/4$, and $\delta_p = \delta_e = 5.0$ from the velocity field equations. Diffusive reconnection of magnetic field footpoints is not shown in Figure 4.4, but is rather superimposed on the trajectories and is also the only kind of footpoint motion occurring in the shaded region bordering the solar equator. From the velocity field equations, the refined Fisk-Parker hybrid field expressions are presented in Eq. 4.31 where all the symbols have their usual meaning.

$$\begin{aligned} B_r &= A\left(\frac{r_0}{r}\right)^2 \\ B_\theta &= B_r \frac{r\omega^*}{V_{SW}}\sin\beta^* \sin\phi \\ B_\phi &= B_r \frac{r}{V_{SW}}[\omega^* \sin\beta^* \cos\theta\cos\phi + \sin\theta(\omega^* \cos\beta^* - \Omega) + \frac{d\omega^*}{d\theta}\sin\beta^* \sin\theta\cos\phi \\ &\quad + \omega^* \frac{d\beta^*}{d\theta}\cos\beta^* \sin\theta\cos\phi] \end{aligned} \tag{4.31}$$

As is the case with the original hybrid field, Eq. 4.31 can be modified to include a latitudinally-

dependent solar wind velocity [*Schwadron*, 2002]. When $F_S = 1$, Eq. 4.31 reduces to the Fisk field presented in *Zurbuchen et al.* [1997], and when $F_S = 0$ it reduces to the standard Parker field presented in *Parker* [1958].

4.6 Modelling a Solar-Cycle Dependence

As first shown by *Fisk* [1996], the relationship between the so-called Fisk angle β and the tilt angle α is given by

$$\beta = \cos^{-1}\left[1 - (1 - \cos\theta'_{mm})\left(\frac{\sin^2\alpha}{\sin^2\theta_{mm}}\right)\right] - \alpha \tag{4.32}$$

where θ_{mm} and θ'_{mm} are the heliomagnetic boundaries of the PCH on the photosphere and the source surface, respectively (see also [*Van Niekerk*, 2000], [*Krüger*, 2005], [*Burger et al.*, 2008]), although PCHs are assumed to be symmetric about $\vec{\Omega}$ and not $\vec{M}$ in the hybrid field approach as mentioned previously. An average value of the maximum extent of the boundary of a PCH on the photosphere (θ_b) and on the source surface (θ'_b) is $\sim 30^\circ$ and $\sim 75^\circ$, respectively, in heliographic coordinates. Therefore, the connection between the heliomagnetic parameters of Eq. 4.32 and the necessary heliographic parameters of the hybrid field is given by:

$$\begin{aligned} \theta_{mm} &= \theta_b + \alpha \\ \theta'_{mm} &= \theta'_b + \alpha. \end{aligned} \tag{4.33}$$

Studying the refined transition function F_S (Eq. 4.28), its relationship with β and ω (Eq. 4.29), together with the refined hybrid magnetic field expressions (Eq. 4.31), one realises it is possible to include a solar-cycle dependence into the refined hybrid model since the PCH sizes depend explicitly on solar activity and influences all the aforementioned equations. In order to include the solar-cycle dependence, two main ideas need to be implemented. Firstly, a time-dependent tilt angle must be modelled, and secondly, the latitudinal maximum extent of the polar coronal hole boundaries, both on the photosphere and source surface, should increase and decrease according to solar activity. This was done by *Burger et al.* [2008] after an in-depth investigation concerning the phases and evolution of PCHs presented in *Krüger* [2005]. Also, to a first approximation, a sinusoidal function should be fitted to the tilt angle data from J.T. Hoeksema in order to simulate the time-dependence of solar activity. This was done and the tilt angle can, therefore, be modelled during an 11-year cycle by use of the following expression [*Burger et al.*, 2008]:

$$\alpha = \alpha_{min} + \left(\frac{\pi}{4} - \frac{\alpha_{min}}{2}\right) \times \begin{cases} 1 - \cos\left(\frac{\pi}{4}T\right) & \text{if } 0 \leq T \leq 4, \\ 1 - \cos\left[\frac{\pi}{7}(T-11)\right] & \text{if } 4 < T \leq 11, \end{cases} \tag{4.34}$$

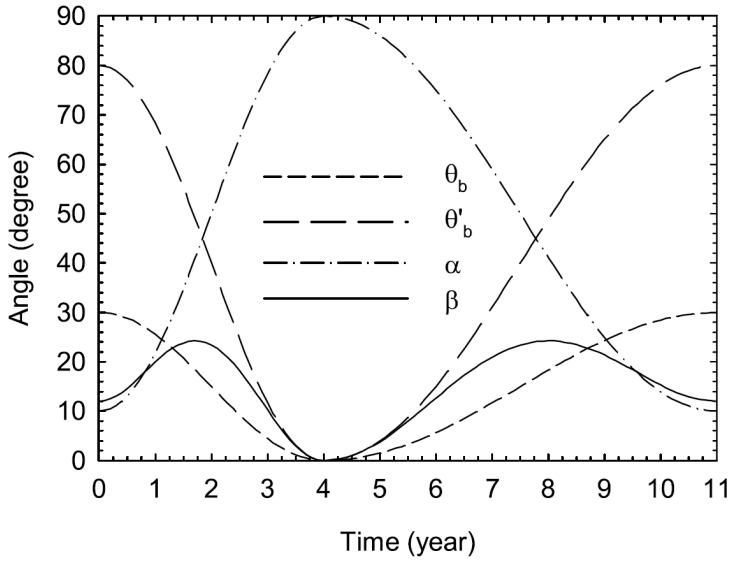

Figure 4.5: Time evolution of the maximum latitudinal extent of the PCH on the photosphere (θ_b - *short dashed line*), on the source surface (θ_b' - *long dashed line*), the tilt angle of the heliospheric current sheet (α - *dot-dashed line*), and the Fisk angle (β - *solid line*) with T the amount of years after solar minimum (figure adapted from *Burger et al.* [2008]).

with the angles defined in terms of radians and T the time in years after solar minimum. The minimum tilt angle is assumed to be $\alpha_{min} = 10^\circ$ or $\pi/18$ rads, while the maximum is assumed to be 90°. Note, for this model it is assumed that it takes 4 ± 1 years to progress from solar minimum conditions to solar maximum conditions, while the remaining 7 ± 1 years of the 11-year cycle is used to reduce back to solar minimum conditions.

Next, a suitable model for the the PCH sizes during the solar activity cycle is presented. Assuming that a PCH disappears during solar maximum conditions, and has the same time evolution as the tilt angle, the following expressions show how the boundaries of the PCHs change with solar activity.

$$\theta_b = \frac{\theta_{b,min}}{2} \begin{cases} 1 + \cos\left(\frac{\pi}{4}T\right) & \text{if } 0 \leq T \leq 4, \\ 1 + \cos\left[\frac{\pi}{7}(T-11)\right] & \text{if } 4 < T \leq 11, \end{cases} \tag{4.35}$$

$$\theta_b' = \frac{\theta_{b,min}'}{2} \begin{cases} 1 + \cos\left(\frac{\pi}{4}T\right) & \text{if } 0 \leq T \leq 4, \\ 1 + \cos\left[\frac{\pi}{7}(T-11)\right] & \text{if } 4 < T \leq 11, \end{cases} \tag{4.36}$$

where θ_b and θ_b' are the latitudinal extent of the PCH on the photosphere and the source surface, respectively. *Burger et al.* [2008] shows how α, β, $\theta_b = 30^\circ$, and $\theta_b' = 80^\circ$ will evolve during an 11-year cycle after solar minimum, shown in Figure 4.5. Note how the PCH disappears ($\theta_b = \theta_b' = 0^\circ$) during solar maximum conditions ($\alpha = 90^\circ$), together with the Fisk angle β. Obviously, the sole use of Eqs. 4.34, 4.35, and 4.36 represents an oversimplification of the time evolution of the tilt angle, but it is sufficient to illuminate the likely behaviour of a Fisk-type field over the course of a solar cycle.

4.7 The Existence of a Fisk-type Field

The Fisk field and Fisk-type fields have been notoriously difficult to prove by searching for its signature in magnetic field data. Although a lot of time has been spent searching for this signature, the results are unsatisfactory since neither a definitive signature is pinned down, nor can the field be ruled out due to some considerations (see [*Zurbuchen et al.*, 1997], [*Forsyth et al.*, 2002], and [*Roberts et al.*, 2007]). Two possible sigatures, namely periodicities and amplitudes of such periodicities, will now be discussed. It is believed periodicities can be further subdivided into two categories. Firstly, the Fisk-Parker hybrid field equations predict that a stationary observer should encounter a periodicity in the magnetic field data equal to that of the sidereal solar equatorial rotation rate. Secondly, as suggested by *Zurbuchen et al.* [1997] and further investigated by *Van Niekerk* [2000], a periodicity is expected when the transit time of a magnetic feature along a footpoint trajectory matches the transit time of the spacecraft in its orbit between two points of intersection (see Figure 5 of *Burger et al.* [2008]). *Zurbuchen et al.* [1997] reports a period of 7 days at 10° co-latitude and 25 days at 30° and with a small Fisk angle $\beta = 12^\circ$ and a differential rotation rate of $\omega \leq \Omega/4$ the period becomes identical to the equatorial rotation rate even at high latitudes. The next consideration is the amplitude of the periodicities. *Roberts et al.* [2007] reports that a Fisk angle of less than 15° would support observations, but it will be very difficult to separate the amplitude of a magnetic feature from noise such as random magnetic field turbulence. Therefore, *Burger et al.* [2008] concludes that a Fisk-Parker hybrid field will not be observable in magnetic field data for $\beta = 12^\circ$.

A periodicity of 27 days was reported by *Roberts et al.* [2007], not in magnetic field data, but rather in the radial component of the solar wind velocity. Since the radial components of both the Parker and Fisk (and Fisk-type) fields depend inversely on the solar wind velocity, it is reasonable to expect a similar significant periodicity in their respective radial directions. *Roberts et al.* [2007] show this is not always the case in the well-established Parker field, which begs the question whether it will be observable in Fisk-type fields. *Burger et al.* [2008] argue that two possibilities are at play here. Firstly, maybe the periodicities are disguised by temporal changes in the field, or secondly, the lack of a definitive period in the magnetic field data from the solar wind velocity is due to footpoint motion masking it. Hence, the heliospheric magnetic field could be Fisk-like after all.

4.7.1 Effect of Fisk-type Fields on Cosmic-Ray Modulation

Fisk-type fields can easily be camouflaged when using magnetic field data on short time and distance scales due to the influence of coronal magnetic diffusion. Another method for searching for a signature of a Fisk-type field is by investigating how cosmic rays will react to this field. Fisk-type fields have a meridional component that is periodic in ϕ. It therefore seems likely that a Fisk-type field will introduce periodicities into cosmic-ray intensities, but will not necessarily have much of an effect on absolute values of cosmic-ray intensities. As en example, *Paizis et al.* [1999] who studied co-rotating interaction regions and the amplitude evolution of the 26-day recurrent cosmic-ray decreases, did not reject the Fisk-field and considered it as

a possible cause of the high-latitude recurrent particle variations. *Zhang* [1997], on the other hand, does not even consider the Fisk field in its investigation of the linear relationship between the latitude gradient and the 26-day recurrent variations of galactic cosmic rays. The current study does not consider cosmic-ray modulation, and the effect of Fisk-type field on the modulation of cosmic-rays can be found in *Burger* [2005],*Kota and Jokipii* [2003], and *Engelbrecht* [2008].

4.8 Summary

The Fisk-Parker hybrid heliospheric magnetic field model of *Burger and Hitge* [2004] was introduced in this chapter. A detailed derivation of this field was given here for the first time. It was also shown that the construction of *Burger and Hitge* [2004] is unique; an issue not considered or at least reported by these authors. Since the original Fisk field of *Fisk* [1996] is difficult to implement in three-dimensional cosmic-ray modulation codes compared to the Parker model [*Parker*, 1958], the divergence-free Fisk-Parker hybrid HMF model was introduced as a good approximation for when field lines open into the heliosphere in the polar regions (Fisk behaviour) and at low latitudes close to the equator (Parker behaviour). A refined Fisk-Parker hybrid model [*Burger et al.*, 2008] which is valid during all solar activity conditions and at all latitudes was also presented. The full derivation of the Fisk-Parker hybrid HMF model was presented in this chapter for the first time, and it was shown that the published equations for this field is unique in its choice of meridional and azimuthal dependencies for the two linearly dependent functions from which the expressions follow. Finally, the existence of a Fisk-type field was discussed by considering magnetic field periodicities and the conclusion is that a Fisk-type field is possible [*Burger et al.*, 2008].

Chapter 5

Magnetic Field Data Analysis

5.1 The Azimuth Angle of the HMF

The azimuth angle ϕ_p of the heliospheric magnetic field is the angle between an anti-sunward directed magnetic field and the radial direction [*Forsyth et al.*, 2002]. It has a larger range and the opposite sign from the typically used winding (or spiral) angle. Since some results of the current analysis will be directly compared with results published by *Forsyth et al.* [2002], their definition is used and not the standard definition of the spiral angle. The spiral angle is a convenient way to quantify how tightly wound the HMF is at different radial distances from the Sun. The azimuth angle from observations or for a model is defined as

$$\phi_B = \tan^{-1}\left(\frac{B_\phi}{B_r}\right), \tag{5.1}$$

and for the Parker model, this becomes

$$\phi_P = \tan^{-1}\left(-\frac{\Omega}{V} r \sin\theta\right), \tag{5.2}$$

for a purely radial solar wind, V. In the equations above, B_r and B_ϕ are the radial and azimuthal components of the heliospheric magnetic field, observed or modelled. The equatorial rotation rate of the Sun is Ω corresponding to a sidereal period of 25.38 days, r is the radial distance from the Sun in AU, and θ is the heliographic polar angle or co-latitude. Hourly averaged magnetic field data from *Ulysses* are used to calculate the Parker model prediction for the spiral angle of the HMF from 25 October, 1990, to 30 June, 2009, shown in Figure 5.1, using Eq. 5.2.

At position (a), the spacecraft was at a radial distance 1.02 AU (and increasing) away from the Sun, at a latitude of $5.3°$ N and a spiral angle of approximately $45°$ following from the Parker prediction, in agreement with previous measurements near Earth (see, e.g., *Smith and Bieber* [1991]). As the radial distance increased to 5.38 AU at position (b), and the latitude to $10.3°$ S, the spiral angle also increased greatly to $81.5°$.

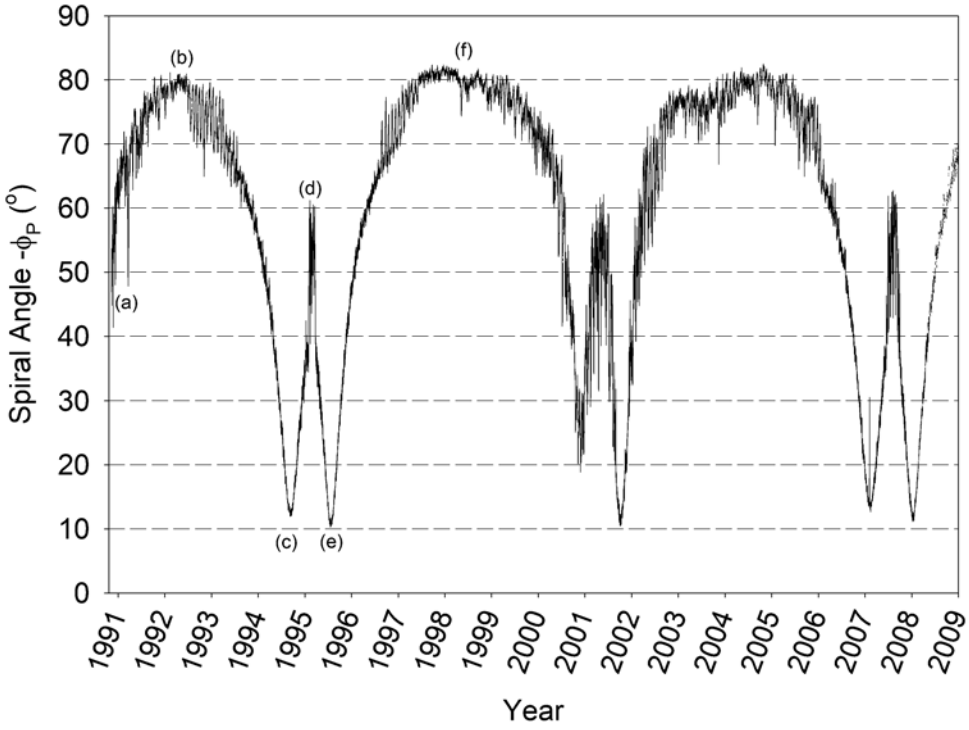

Figure 5.1: Hourly-averaged spiral angles predicted by the Parker HMF model calculated from the magnetic field data of the *Ulysses* mission from 25 October, 1990, to 30 June, 2009.

The effect of the fast solar wind speed on the spiral angle can be seen in the region just after position (b) where the spiral angle is seen to vary dramatically in the turbulent magnetic field. The drop in spiral angle after position (b) is attributed to the decreasing radial distance from the Sun and the increasing latitude. At position (c), the radial distance is 2.3 AU at a latitude of $80.2°$ S after which the fast latitude scan (FLS) (between position (c) and (e)) commenced. After position (c), *Ulysses* travelled back towards the solar equatorial region and a sharp increase in spiral angle is observed due to the sharp decrease in latitude. The radial distance at position (d) is 1.3 AU and is its closest approach to the Sun.

The radial distance at position (e) is 2.0 AU with an observed spiral angle of $10°$ at $80.1°$ N latitude. Again, a sharp spiral angle increase is observed towards position (f) where the radial distance increases to 5.3 AU and a spiral angle increases to $80.1°$. This completes the first full orbit of *Ulysses* around the Sun after which the same behaviour is observed.

The orbit of *Ulysses* is sub-divided into 10 specific scanning sectors as suggested by *Forsyth et al.* [2002]. The ten intervals are based on solar wind and magnetic field properties observed during the orbit. The following list states the heliographic latitudes of each sector and the main reasons why these sectors were specifically chosen by Forsyth and co-workers. Here the observed tilt angles (courtesy of The Wilcox Solar Observatory, see `http://wso.stanford.edu/Tilts.html`) in a specific hemisphere North or South are added to give an indication of whether Ulysses should have observed two polarities or just one. Tilt angles computed with the radial boundary condition at the photosphere are used in this study. Figure 5.2 shows a schematic illustration of the different intervals in which the magnetic field data are subdivided into for analyses.

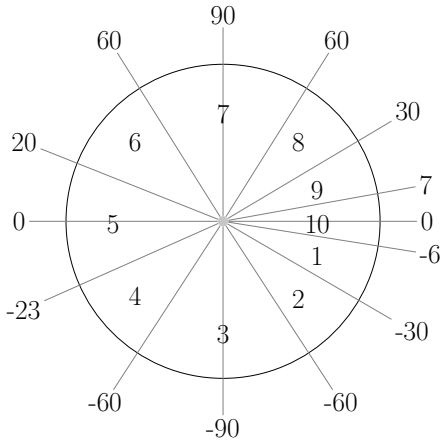

Figure 5.2: Illustration of the different sectors scanned by *Ulysses* during its first solar orbit. Each sector is labelled according to the list below, while the latitudes are also shown. Note that negative values indicate latitude values for the southern solar hemisphere.

1. 6°S - 30°S: Both positive and negative magnetic field polarities were present in this region swept by the wavy current sheet and co-rotating interaction regions were dominant. This region was scanned from 3 January 1992 to 3 May 1993. Tilt angles were between 17° and 38°.

2. 30°S - 60°S: Only inward polarity magnetic field lines were observed due to no current sheet interference. This region was scanned from 3 May 1993 to 17 April 1994. Tilt angles were between 17° and 27°.

3. 60°S - 60°S: Unexpected azimuthal angle changes in the magnetic field were previously reported in this region, scanned from 17 April 1994 to 21 December 1994. Tilt angles were between 11° and 27°.

4. 60°S - 23°S: An even and fast solar wind speed spread were detected here, as well as only inward polarity magnetic field lines. This region was scanned from 21 December 1994 to 2 February 1995. Tilt angles were between 11° and 15°.

5. 23°S - 20°N: Both positive and negative magnetic field polarities were measured during the FLS from 2 February 1995 to 31 March 1995. Tilt angle were between 16° (south) and 8° (north).

6. 20°N - 60°N: Only outward magnetic field line polarities were detected. This region was scanned from 31 March 1995 to 31 May 1995. Tilt angles were between 7° and 8°.

7. 60°N - 60°N: To group the most northern latitudes in the same bin size as the most southern latitudes. This region was scanned from 31 May 1995 to 19 November 1995. Tilt angles were between 3° and 7°.

8. 60°N - 30°N: A reliable and homogeneous fast solar wind speed spread were observed together with magnetic field lines with only an outward polarity, scanned from 19 November 1995 to 3 August 1996. Tilt angles were between 3° and 16°.

9. 30°N - 7°N: Co-rotating interactions regions and both magnetic field lines polarities were detected during this scan from 3 August 1996 to 30 July 1997. Tilt angles were between 2° and 16°.

10. 7°N - 7°S: This is where *Ulysses* crossed the equatorial regions to complete the first orbit from 30 July 1997 to 25 May 1998. Tilt angles were between 7° (north) and 43° (south).

It turns out to be problematic to compare spiral angles predicted by a model for the HMF with observed values using the azimuthal and the radial components of the magnetic field. Figure 5.3 shows hourly-averaged spiral angles observed by *Ulysses* (small black circles) compared with the spiral angles modelled by the Parker model (solid black line) during 6° S - 30° S as a function of time. It is clear large fluctuations obscure the comparison. Therefore, magnetic field lines are first separated into two classes: sunward and anti-sunward directed field lines (see Section 2.4.3).

Presenting and analysing magnetic field data when the field can be away from the Sun or toward it, can be a challenge. Figure 5.4a from *Smith and Bieber* [1991] shows a polar histogram presenting the hourly magnetic field orientation at the Earth as recorded on the NSSDC omnitape data set in 1980. The spiral angles calculated with the magnetic field lines directed towards the Sun are represented in the lower left hand quadrant of Figure 5.4a, while those calculated with the magnetic field lines directed away from the Sun are observed in the upper right hand quadrant. Although there is significant scatter in the data, this kind of representation shows that the observed magnetic field is on average in reasonable – but not prefect – agreement with the prediction of the Parker field.

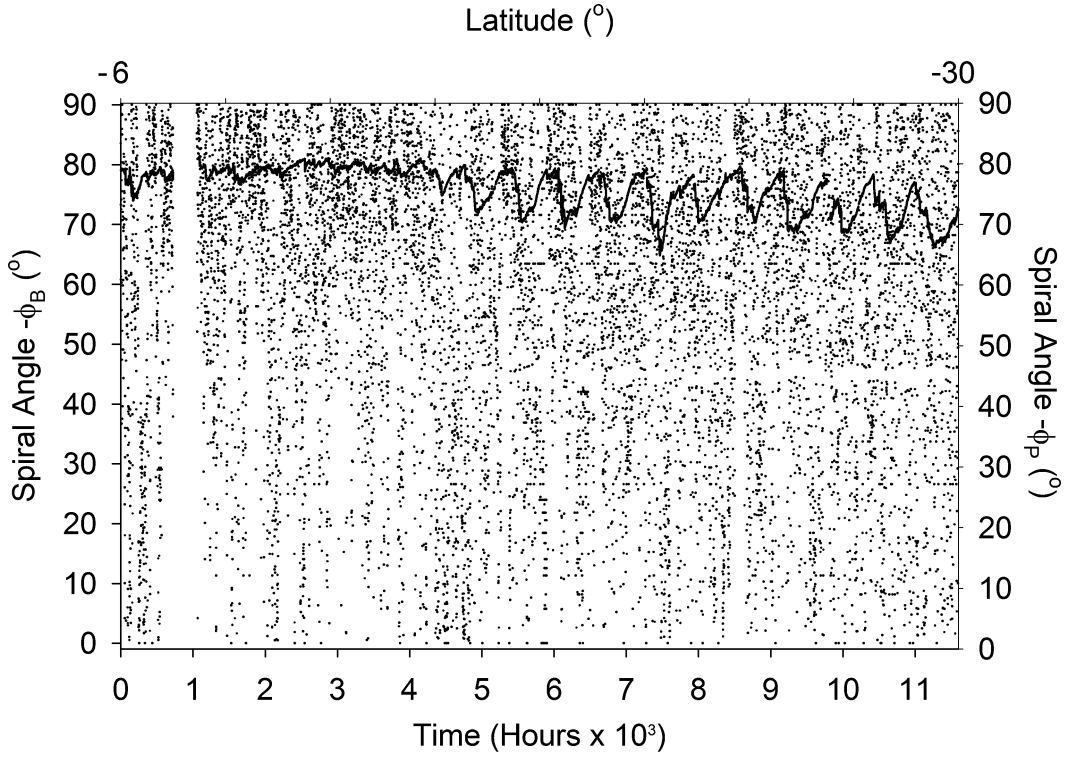

Figure 5.3: Spiral angles observed by *Ulysses* ($-\phi_B$) during the 6° S - 30° S interval. The solid black line represents the spiral angles modelled by the Parker model ($-\phi_P$).

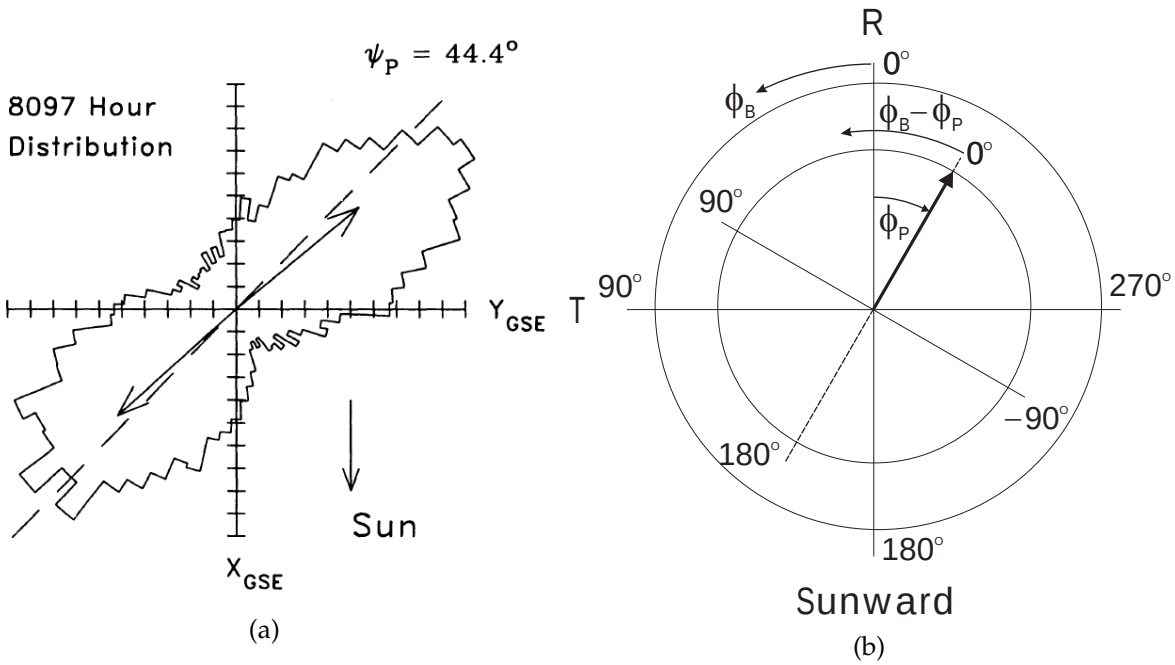

Figure 5.4: Left: Polar histogram showing the two-sector structure of the heliospheric magnetic field as reported by *Smith and Bieber* [1991]. Right: Dial plot illustrating the geometrical definitions of ϕ_B, ϕ_P, and $\phi_B - \phi_P$.

A polar plot is therefore a useful tool to judge the distribution of magnetic fields. The methodology of *Forsyth et al.* [2002] will be followed to analyse the *Ulysses* magnetic field data, and also their nomenclature. Figure 5.4b shows how ϕ_B and ϕ_P are defined; the meridional angle will not be used in the present study. The authors state that ϕ_B can vary from 0 to 360 degrees, measured anti-clockwise from the radial direction; ϕ_P is measured clockwise from the same axis and is always negative. The direction of the magnetic field is always calculated with respect to the direction of the Parker (or other) model in the direction away from the Sun. This can be confusing, especially since negative values occur in the histograms involving the azimuth angle. For more clarity, Figure 5.4b shows ϕ_B, ϕ_P , and $\phi_B - \phi_P$ on a dial plot. Note that values of $\phi_B - \phi_P$ between $270°$ and $360°$ are replaced by values from $-90°$ to 0. This choice does not alter the results in any way and it simplifies the interpretation of the histograms. Note that fields with vector orientated clockwise with respect to the Parker field direction, are more tightly wound than that field, and fields with vector orientated anti-clockwise with respect to the Parker field direction, less tightly. The difference between the observed field direction and the Parker (or other model) direction, is used to create the histograms of Section 5.3.

5.2 Polar Plots

Focussing on only the intervals of the southern pass of *Ulysses* and one interval covering the northern polar pass, Figure 5.5 shows the five polar plots representing the field direction predicted for the Parker HMF model and the directions observed by *Ulysses*. The horizontal and vertical axes are the radial and tangential directions in nano Tesla (nT), respectively, while the outer-circle marks the field direction (see Fig. 5.4b) relative to the radial direction in degrees.

The filled black circles indicate values observed by *Ulysses* while the blue filled circles are values predicted by the Parker HMF model. Following the same interval divisions as described in Section 5.1, Figures 5.5a to 5.5e show the observed and predicted field direction between 6° S - 30° S, 30° S - 60° S, $> 60^\circ$ S, 60° S - 23° S, $> 60^\circ$ N, respectively.

Figure 5.5a shows a more or less even distribution of fields toward the Sun and away from it, indicative of *Ulysses* being immersed in the region swept by the current sheet. If it is above the current sheet, it samples one polarity and below it, the other polarity. The spread in values predicted by the Parker model, is of course due to changes in radial distance, latitude and solar wind speed.

As expected from $A < 0$ conditions, the fast majority of magnetic field lines are directed inward when *Ulysses* crossed near the southern heliographic pole (Figure 5.5c), and directed outward when *Ulysses* crossed near the northern heliographic pole (Figure 5.5e). The dominant inward directed field lines are seen in Figure 5.5d suggests that the maximum extend of the current sheet in the southern hemisphere was less than 23°. The tilt angle value of the current sheet for this period was in fact between 11° and 15°.

Although polar plots are visually appealing representations of magnetic field directions and consequently spiral (or azimuth) angles, it does not lend itself to quantitatively compare predicted and observed spiral angles. Polar plots give a birds-eye view of data and an indication, for example, of how well the Parker model predicts the magnetic field direction. They do not give a time-step by time-step comparison and are by and large a statistical description of data, highlighting average behaviour. The same is true for the histograms shown in the next section.

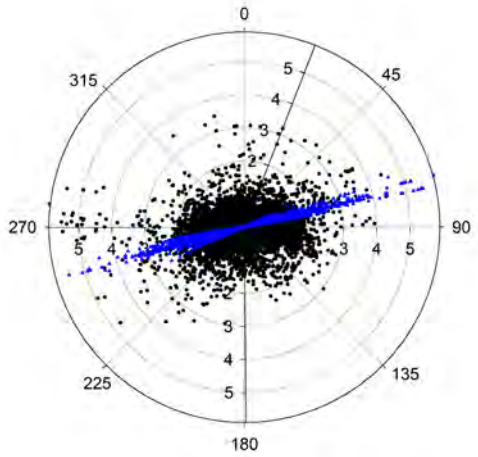

(a) 6° - 30° S

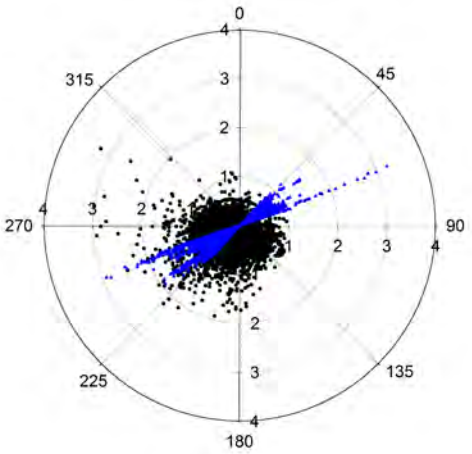

(b) 30° - 60° S

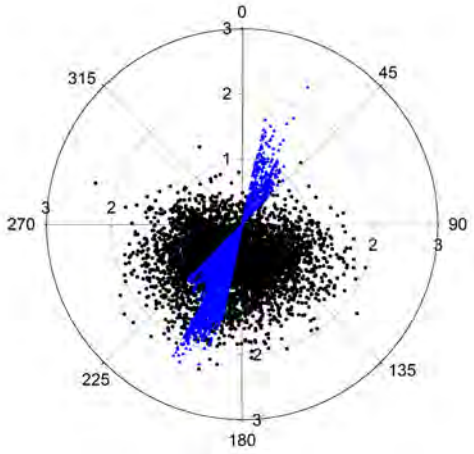

(c) > 60° S

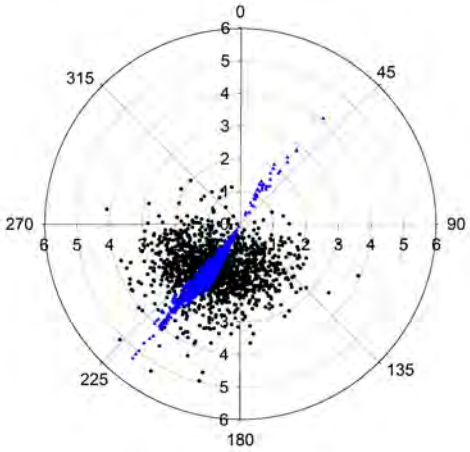

(d) 60° - 23° S

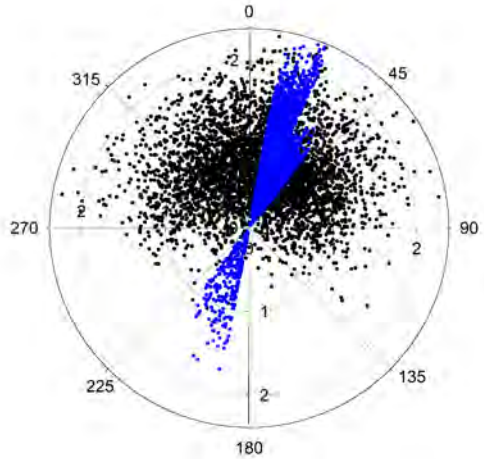

(e) > 60° N

Figure 5.5: Polar plots of five different sectors scanned by *Ulysses*. The filled black circles are values observed by *Ulysses* while the blue filled circles are values predicted by the Parker HMF model.

5.3 Histograms

Histograms are useful in the analysis of magnetic field data (see e.g. [*Thomas and Smith*, 1980], [*Burlaga et al.*, 1982], [*Forsyth et al.*, 1996], [*Balogh et al.*, 1999a], [*Forsyth et al.*, 2002]). The current study follows the analysis of *Forsyth et al.* [2002] and will compare the observed (ϕ_B) and predicted Parker (ϕ_P) azimuth angles of the HMF by calculating the difference between the two angles. The observed and the predicted azimuth angle are calculated using Eqs. 5.1 and 5.2, respectively, where the tangential (*T*) and radial (*R*) magnetic field components are used instead of B_ϕ and B_r for the observed spiral angles. If $\phi_B - \phi_P = 0^\circ$ or $\phi_B - \phi_p = 180^\circ$, then there is a perfect agreement between observed and predicted azimuth angles (see Fig. 5.4b). If the difference is within 90° of 0°, the field is directed away from the Sun, and if the difference is within 90° of 180°, the field is directed towards the Sun. With respect to the expected peaks at 0° and at 180°, the observed field is more tightly wound than the Parker prediction if the difference has a value less than 0° or less than 180°, and it is more tightly wound if the value is larger than 0° or larger than 180°. This is also shown in Fig. 5.4b.

Hourly averaged magnetic field data from *Ulysses* are used to calculate the observed and predicted azimuth angles and binned into 10° wide bins in the histograms of the following few subsections. It must be emphasized that this is a statistical treatment that yields the likelihood that a model of the HMF agrees with observations. The time line of the measurements in a chosen range of latitudes no longer play a role.

5.3.1 Comparison with Parker Model

Figures 5.6 and 5.7 show the deviations between the predicted Parker and observed azimuth angles for the 10 latitude-intervals during the first orbit of *Ulysses*. The deviations ($\phi_B - \phi_P$) are on the horizontal axis and run from -90° to 270°. Dashed lines are drawn at $\phi_B - \phi_P = 0^\circ, 90^\circ, 180^\circ$ to guide the eye, while the frequency (number of observations in a particular bin) is on the vertical axis. The range of the tilt angle α is also shown. All of the results shown in Figs. 5.6 and 5.7 are also presented in *Forsyth et al.* [2002]. The agreement with their results is excellent.

Figures 5.6a, 5.6e, and 5.7d show intervals where both magnetic polarities are present. This is due to the fact that intervals close to the ecliptic plane sample different sectors of the heliospheric current sheet (HCS). A greater number of *inward* directed magnetic field lines are present during the $6^\circ S - 30^\circ$ S interval which is expected when scanning from the ecliptic towards the southern heliographic pole in $A > 0$ conditions. From all the histograms it is clear the deviations are not symmetric about the expected values, 0° and 180°, implying over- and underwinding. To quantify the level of over- and underwinding of magnetic field lines during each interval, the percentage of spiral angles in the intervals $\pm 90^\circ$ around 0° and 180° are calculated and shown in Table 5.1.

In general, the observed and predicted spiral angles are in good agreement to a first approximation. If, however, a perfect agreement between the two is found, a $50\% - 50\%$ distribution symmetric about the central values is expected.

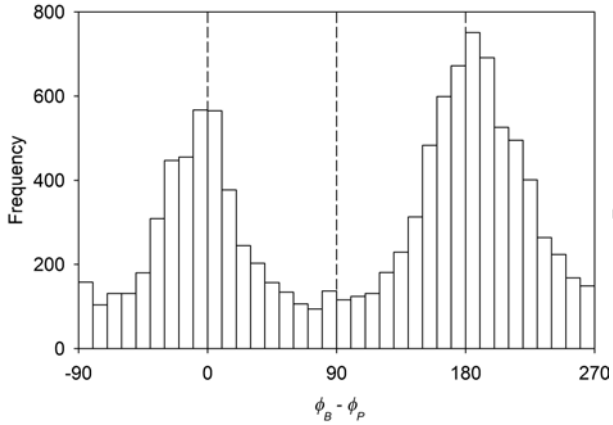

(a) Parker 6° S - 30° S $\alpha = 17° - 38°$

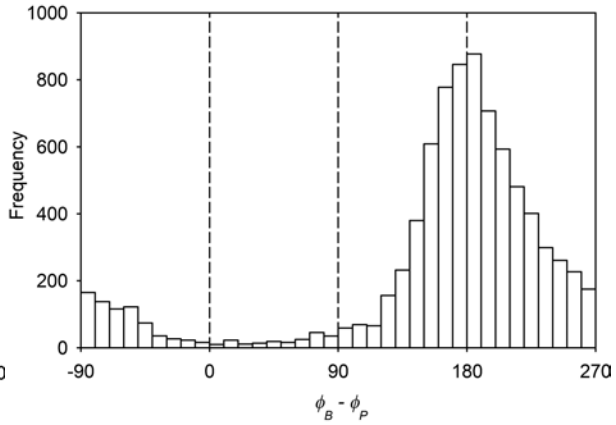

(b) Parker 30° S - 60° S $\alpha = 17° - 27°$

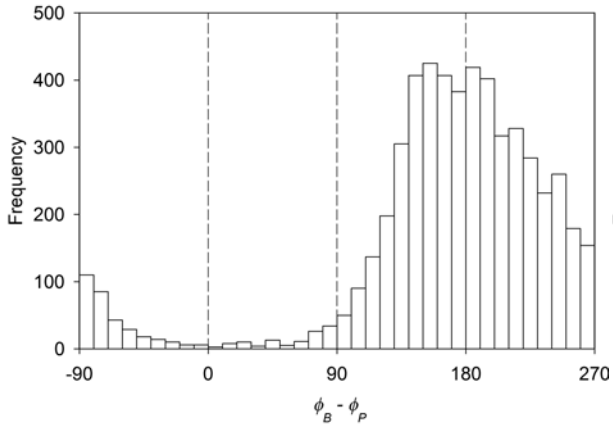

(c) Parker $> 60°$ S $\alpha = 11° - 27°$

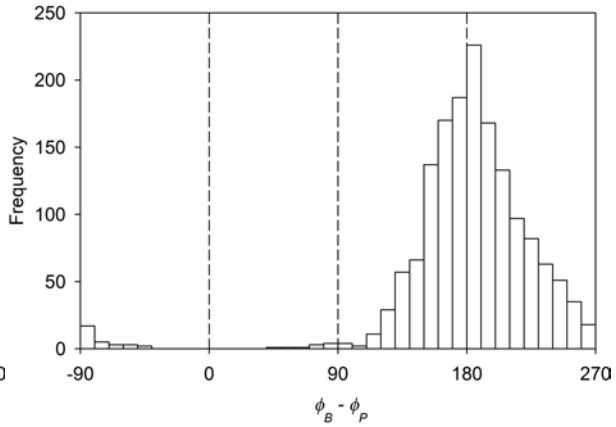

(d) Parker 60° S - 23° S $\alpha = 11° - 15°$

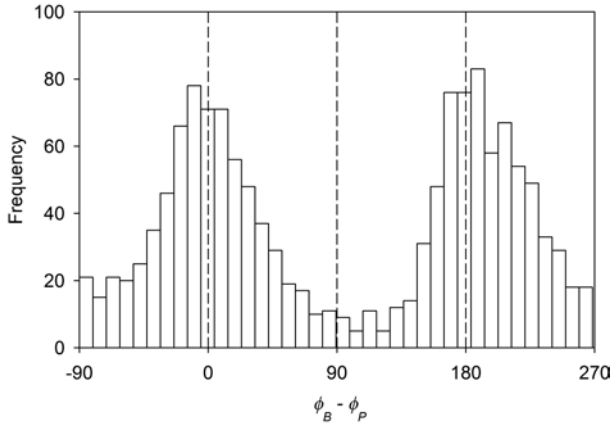

(e) Parker 23° S - 20° N $\alpha = 16°$ S - 8° N

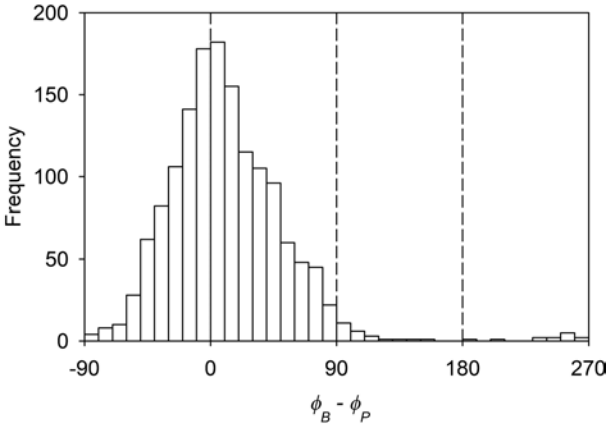

(f) Parker 20° N - 60° N $\alpha = 7° - 8°$

Figure 5.6: Deviation of the predicted Parker from the observed azimuth angles during the first orbit of *Ulysses* for the first six intervals as discussed in Section 5.1.

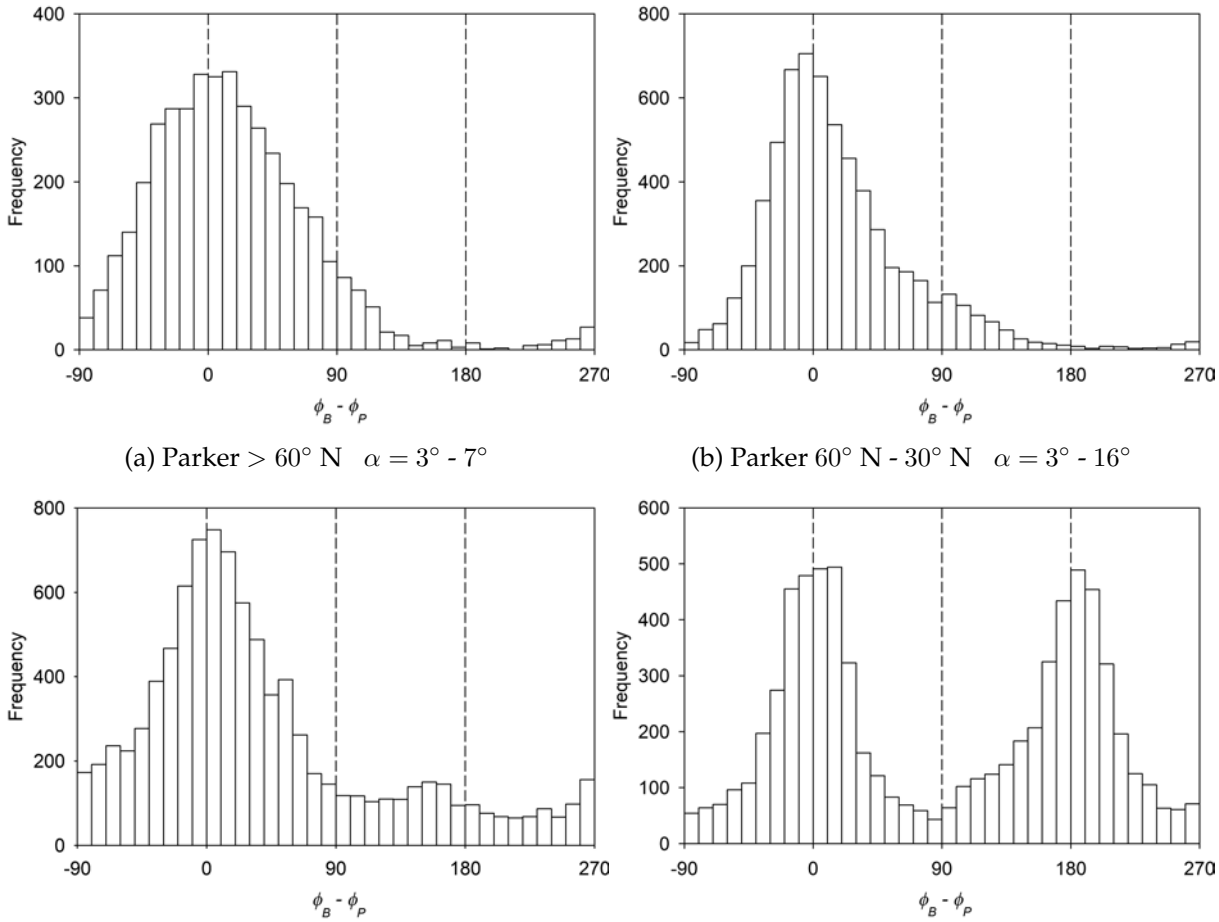

(a) Parker $> 60°$ N $\alpha = 3°$ - $7°$

(b) Parker $60°$ N - $30°$ N $\alpha = 3°$ - $16°$

(c) Parker $30°$ N - $7°$ N $\alpha = 2°$ - $16°$

(d) Parker $7°$ N - $7°$ S $\alpha = 7°$ N - $43°$ S

Figure 5.7: Same as Fig. 5.6 but for the last four intervals as discussed in Section 5.1.

Figure 5.6a shows more tightly wound magnetic field lines for anti-sunward directed field lines, while less tightly magnetic field lines are observed for sunward directed field lines. Similar behaviour is observed in the two remaining dual-polarity histograms. A strong signature for *inward* directed magnetic field lines is found during the southern solar hemisphere pass (see Figures 5.6b, 5.6c, and 5.6d). In all three cases, overwinding of the sunward magnetic field lines are noted. Interestingly, when *Ulysses* scanned the most southerly latitudes, as shown in Figure 5.6c, a double peak is observed which involves two populations of preferred angles. The frequency of the peak in the bin centred around $155°$ is greater than the frequency of the secondary peak that is closer to the expected $180°$. *Forsyth et al.* [2002] reports that the most probable value is $24°$ more tightly wound than expected which is a significant deviation from the predicted Parker spiral angles.

Finally, Figures 5.6f, 5.7a, 5.7b, 5.7c, and 5.7d all have *outward* directed magnetic field lines in accordance with magnetic field lines originating from the northern solar hemisphere. Predominantly less tightly wound magnetic field lines are observed in these four regions. When comparing spiral angles from $> 60°$ S and its corresponding interval, $> 60°$ N, no clear similarities are seen as the double peak of Figure 5.6c is not reproduced in Figure 5.7a.

Surprisingly, Figure 5.7c shows the return of *inward* magnetic field lines, although much less

than the dominant *outward* directed field lines. This can be explained by the presence of a warp in the HCS at one localised longitude region that led to the return of a sector structure in the *Ulysses* data at higher latitudes than expected [*Forsyth et al.*, 1997]. The strong unipolar behaviour in both hemispheres, respectively, is consistent with the near solar minimum HMF configuration. Another feature of this analysis worth noting is that whenever a single polarity region was sampled, the azimuth angles are biased towards an underwound direction, independent of position (southern or northern hemisphere) and polarity (towards or away). *Forsyth et al.* [2002] suggest this behaviour can be attributed to the presence of Alfvén waves in the fast solar wind due to the fact they propagate radially rather than along the field.

5.3.2 Comparison with the Generalised Fisk Model

This section presents the deviation of the azimuth angles of the generalised Fisk field in histogram form. Eqs. 5.3 and 5.4 (repeated here for ease of reference) below are used to calculate the azimuthal angles by making use of the exact same analysing method of section 5.3.1 for comparability reasons.

$$B_r = B_r \left[1 + \frac{r\omega(\theta,\phi)\sin\beta\sin\phi^*}{V(\theta)^2}\frac{\partial V(\theta)}{\partial\theta}\right] \tag{5.3}$$

$$B_\phi = \frac{B_r r}{V(\theta)}\left[\omega(\theta,\phi)\sin\beta\cos\theta\cos\phi^* + \omega(\theta,\phi)\cos\beta\sin\theta - \Omega\sin\theta\right] \tag{5.4}$$

Since the generalised Fisk field has more parameters to take into consideration, care is taken to implement the correct values for these different dependencies. Firstly, the differential rotation rate $\omega(\theta,\phi)$ is calculated using the transformations from Section 3.3. Secondly, the Fisk angle β is calculated by making use of Eq. 3.26 with $\theta_{mm}^{ph} = 24^\circ$ and $\theta_{mm}^{ss} = 70^\circ$, the boundaries of the polar coronal hole on the photosphere and the source surface, respectively. Thirdly, the tilt angle α used during each scanned sector depends on the heliocentric radial distance of *Ulysses*. The angle reported by the WSO is the angle observed at close proximity to the Sun. The angle observed by *Ulysses* at say, ~ 5 AU during the 6° S - 30° S scan, propagated from the Sun through the heliosphere for ~ 23 days. The propagation speed is taken as the mean solar wind speed during the interval which was 536 km/s for the above-mentioned case. Therefore, this study incorporates a tilt-angle delay to ensure the most probable tilt angle observed by *Ulysses* is used when calculating the azimuthal angles. Furthermore, the $\partial V(\theta)/\partial\theta$ term is calculated by using the following definition of a derivative:

$$\frac{\partial V(\theta)}{\partial\theta} = \frac{V(\theta+h) - V(\theta)}{h}, \tag{5.5}$$

where $h = 0.1$ since the smallest latitude increment is 0.1°.

Figure 5.8 and 5.9 show the deviations between the predicted generalised Fisk and observed azimuth angles for the 10 latitude-intervals during the first orbit of *Ulysses*. The same nomenclature and definitions of section 5.3.1 are used.

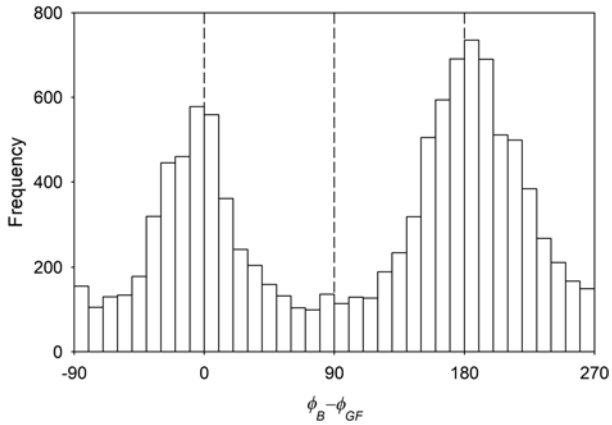

(a) Gen. Fisk 6° S - 30° S $\alpha = 17°$ - 38°

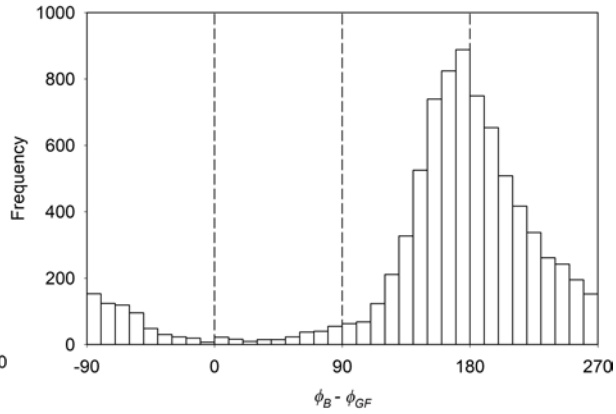

(b) Gen. Fisk 30° S - 60° S $\alpha = 17°$ - 27°

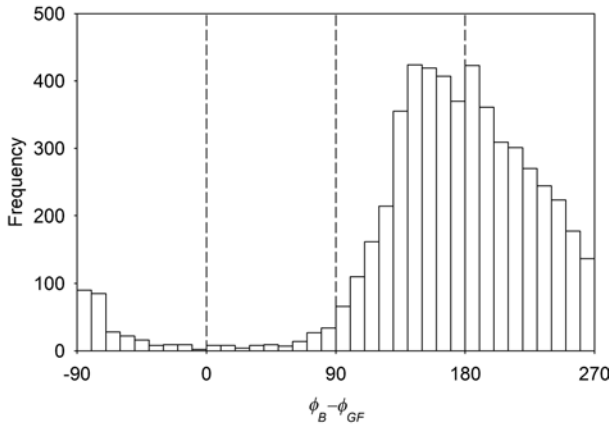

(c) Gen. Fisk $> 60°$ S $\alpha = 11°$ - 27°

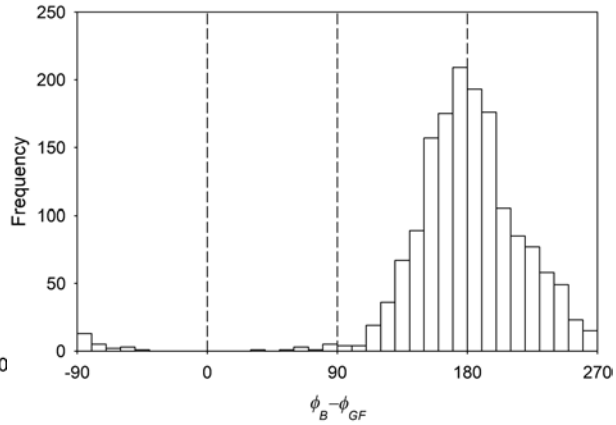

(d) Gen. Fisk 60° S - 23° S $\alpha = 11°$ - 15°

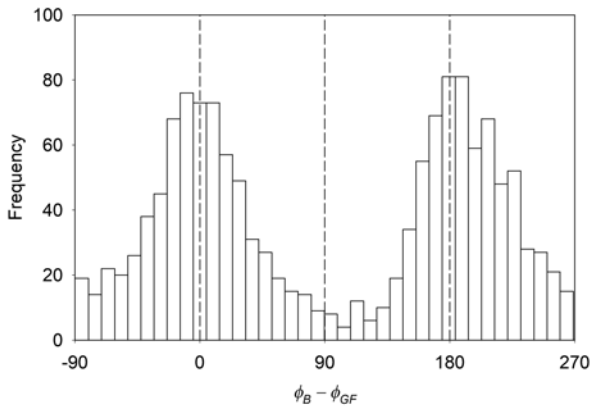

(e) Gen. Fisk 23° S - 20° N $\alpha = 16°$ S - 8° N

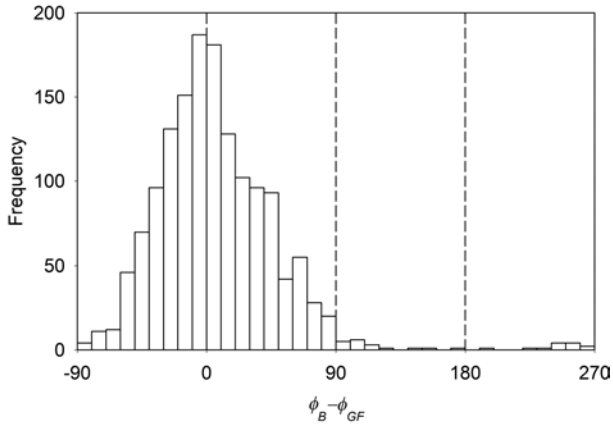

(f) Gen. Fisk 20° N - 60° N $\alpha = 7°$ - 8°

Figure 5.8: Deviation of the predicted generalised Fisk from the observed azimuth angles during the first orbit of *Ulysses* for the first six intervals as discussed in Section 5.1.

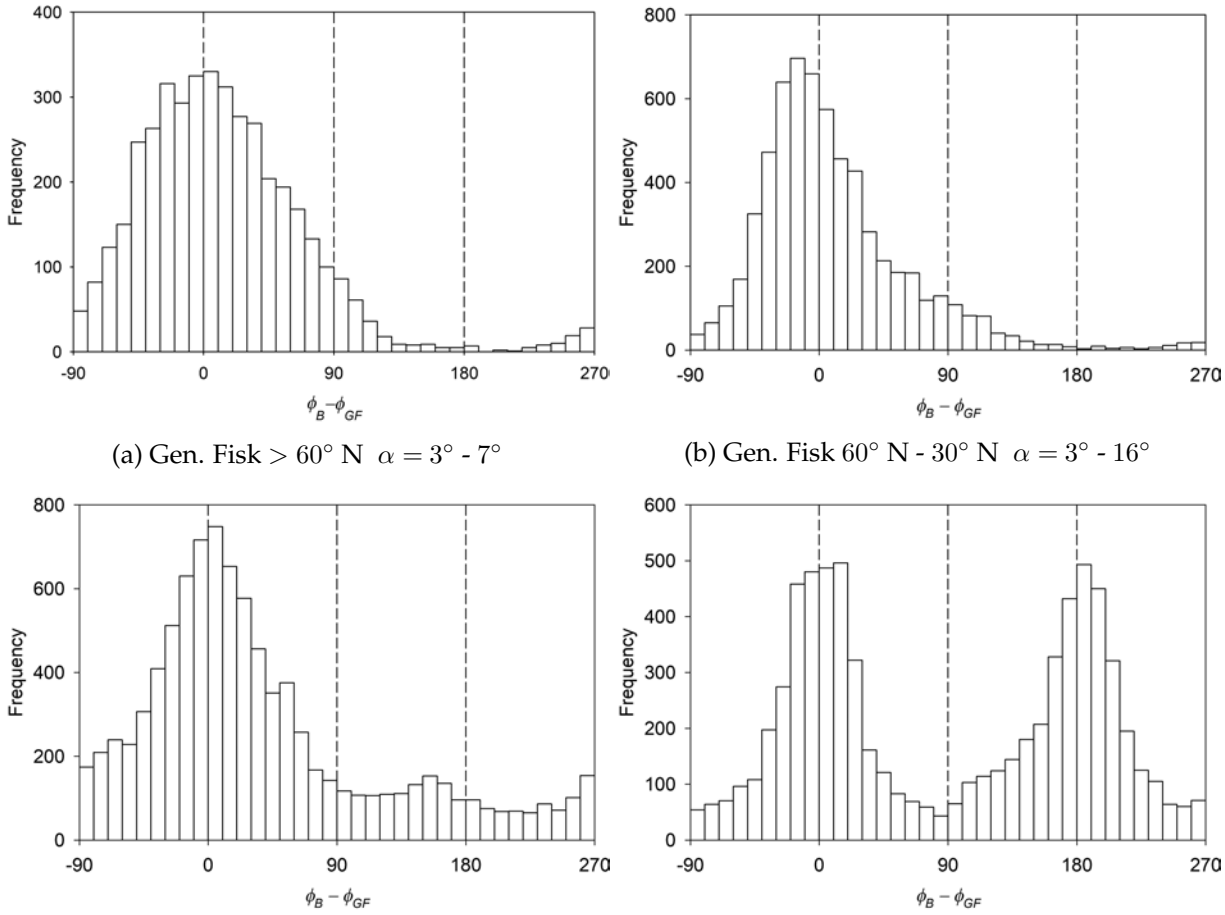

(a) Gen. Fisk $> 60°$ N $\alpha = 3°$ - $7°$

(b) Gen. Fisk $60°$ N - $30°$ N $\alpha = 3°$ - $16°$

(c) Gen. Fisk $30°$ N - $7°$ N $\alpha = 2°$ - $16°$

(d) Gen. Fisk $7°$ N - $7°$ S $\alpha = 7°$ N - $43°$ S

Figure 5.9: Same as Fig. 5.8 but for the last four intervals as discussed in Section 5.1.

Figures 5.8a, 5.8e, and 5.9d show intervals where both magnetic polarities are present since these three intervals are close to the equatorial plane and sample different sectors of the HCS. Figures 5.8b, 5.8c, and 5.8d show intervals where only *inward* directed field lines are present, while the *outward* directed field lines are seen in Figures 5.8f, 5.9a, 5.9b, and 5.9c. Qualitatively, these results are similar to the results of section 5.3.1, except for the amount of overwinding and underwinding during each interval.

Forsyth et al. [2002] used the Fisk field equations of *Zurbuchen et al.* [1997] and investigated magnetic field data from *Ulysses* during its high southern latitude scan ($> 66°$ S) and observed the same double-peaked histogram observed with the Parker model (see Figure 5.6c). Figure 5.8c shows the same double-peak behaviour. *Forsyth et al.* [1996] first suggested that this double peak can be due to large amplitude Alfvén waves. Since Alfvén waves have periods of more than a few hours, this assumption was tested by taking daily, instead of hourly, magnetic field averages to calculate the deviation of the spiral angles in this region. By doing this, the double-peak was eliminated. Applying the same method to the generalised Fisk field also eliminated the double peak. Therefore, the hypothesis that Alfvén waves can be responsible for the double-peak cannot be ruled out.

Figure 5.8d shows no overwinding or underwinding for the *inward* directed field lines during the $60°$ S - $23°$ S interval (see Table 5.1). Interestingly, the given tilt angle range for this interval

Statistics of Azimuth Angle Distributions						
HMF Model	Latitude Range	No. of obs.	$\% < 0°$	$\% > 0°$	$\% < 180°$	$\% > 180°$
Parker	6°S - 30°S	11664	55%	45%	44%	56%
Gen. Fisk	6°S - 30°S	11664	56%	44%	45%	55%
Parker	30°S - 60°S	8412			45%	55%
Gen. Fisk	30°S - 60°S	8412			52%	48%
Parker	$> 60°$S	5487			49%	51%
Gen. Fisk	$> 60°$S	5487			51%	49%
Parker	60°S - 23°S	1578			44%	56%
Gen. Fisk	60°S - 23°S	1578			50%	50%
Parker	23°S - 20°N	1397	54%	46%	38%	62%
Gen. Fisk	23°S - 20°N	1397	52%	48%	38%	62%
Parker	20°N - 60°N	1488	44%	56%		
Gen. Fisk	20°N - 60°N	1488	49%	51%		
Parker	$> 60°$N	4192	46%	54%		
Gen. Fisk	$> 60°$N	4192	48%	52%		
Parker	60°N - 30°N	6174	48%	52%		
Gen. Fisk	60°N - 30°N	6174	55%	45%		
Parker	30°N - 7°N	9000	46%	54%		
Gen. Fisk	30°N - 7°N	9000	48%	52%		
Parker	7°N - 7°S	7223	49%	51%	47%	53%
Gen. Fisk	7°N - 7°S	7223	49%	51%	47%	53%

Table 5.1: The statistics of the azimuth angle distributions of the Parker and generalised Fisk HMF models in the ten intervals scanned by *Ulysses*.

results in a β value that falls within this scanned interval, that is, the $\vec{p}$-axis is in this interval. It is the author's assertion that the location of the $\vec{p}$-axis plays a more important role than previously thought since no over- or underwinding is found close to this axis when implementing the generalised Fisk field. Furthermore, the location of the $\vec{p}$-axis on the opposite side of the Sun falls inside the $20°$ N - $60°$ N (Figure 5.8f) interval and only 1% underwinding is observed, compared to the 6% overwinding predicted by the Parker model (Figure 5.6f).

Figure 5.9b shows the *outward* directed field lines are overwound by 5%, while Figure 5.7b shows the same directed field lines, but overwound by only 2%. This is an unexpected result. Based on all the percentage values in Table 5.1, the generalised Fisk field predicts the azimuth angles better than the Parker model for all intervals except in this one case. This result will be further investigated in the next section.

5.4 Comparing Radial and Azimuthal Field Components

The azimuthal (or spiral) angle depends on the ratio of the azimuthal and the radial field components. Obviously if a model predicts a correct ratio, it does not necessarily follow that the individual components are correct. It is therefore necessary to compare these two components with data as well.

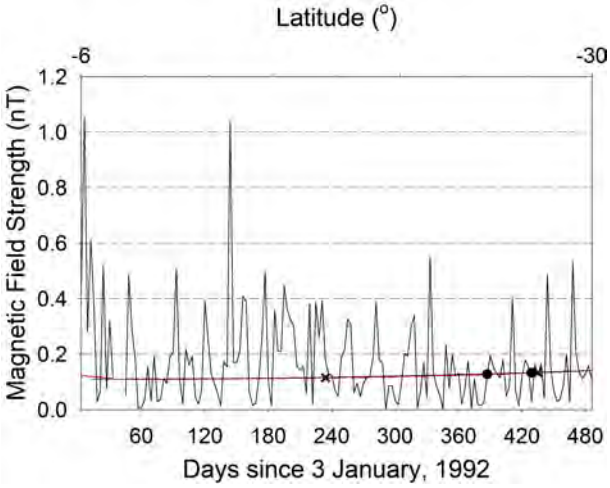

(a) Radial Component $6°$ S - $30°$ S

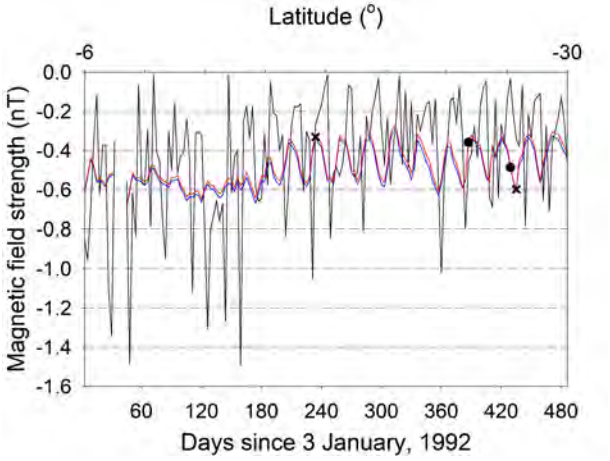

(b) Azimuthal Component $6°$ S - $30°$ S

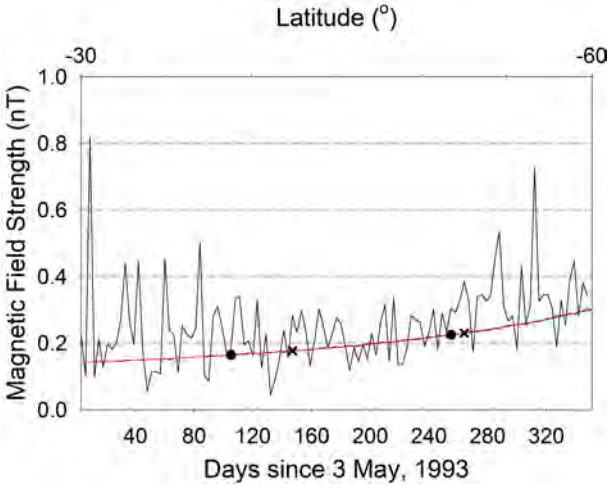

(c) Radial Component $30°$ S - $60°$ S

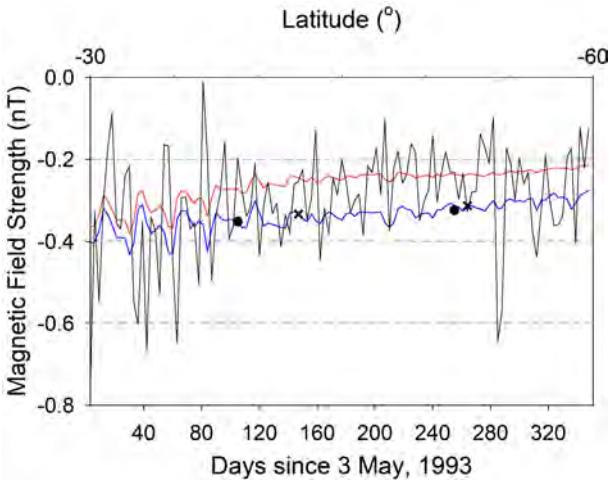

(d) Azimuthal Component $30°$ S - $60°$ S

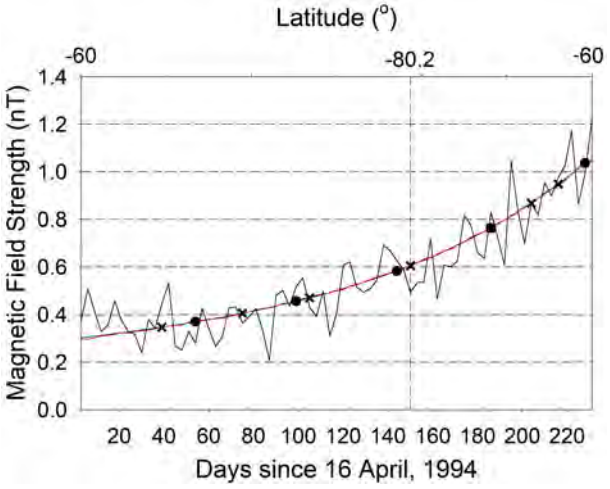

(e) Radial Component $> 60°$ S

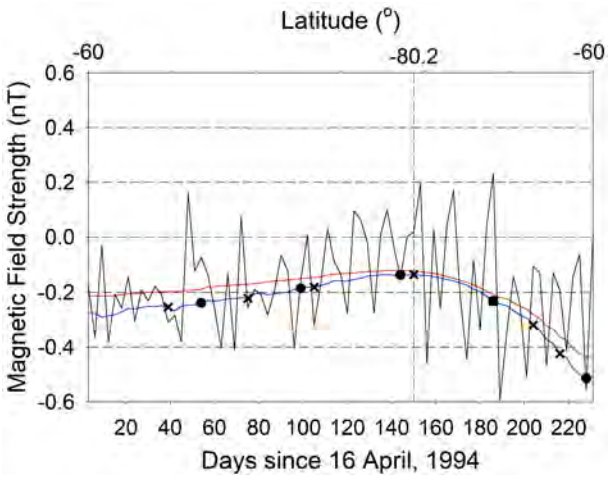

(f) Azimuthal Component $> 60°$ S

Figure 5.10: Three-day averaged comparison of the radial (left column) and azimuthal (right column) components of the magnetic field, the Parker model and the generalised Fisk model for the first three intervals scanned by *Ulysses*. The solid black crosses represent time tickers placed every $10°$ scanned for the first four panels, and $5°$ scanned for the last two. The solid black circles represent time tickers placed every 0.1 AU travelled for the first two panels, 0.5 AU for the middle two panels, and 0.3 AU for the last two panels. The vertical dashed line in Figures 5.10e and 5.10f shows the maximum southern latitude reached by *Ulysses*.

Figures 5.10, 5.11, and 5.12 show the radial and azimuthal components of the magnetic field observed by *Ulysses* and the predictions of both the Parker and generalised Fisk models for each interval as defined in section 5.1. In the following plots, the black, blue, and red lines represent the three-day averaged magnetic field, and the three-day averaged predictions of the Parker and generalised Fisk models, respectively.

Figure 5.10a shows an almost perfect agreement between the Parker model and generalised Fisk model radial component predictions for the 6° S - 30° S interval. The results of the models follow the trend of the observed magnetic field which oscillates around the predictions. Figure 5.10b also shows a good agreement between models and experimental data. Close to the equatorial region, the two models overlap significantly, after which a small separation is seen with increasing latitude. This phenomena is best observed in the azimuthal component of the 30° S - 60° S interval presented in Figure 5.10d. The generalised Fisk field also fits the observed magnetic field better than the Parker for this interval. The radial component of this interval (Figure 5.10c) is well-predicted by the two models and follow the increasing magnetic field strength trend with increasing latitude (and decreasing heliocentric radial distance). During the near southern pole crossing, shown in Figures 5.10e and 5.10f, the azimuthal components of the two models are very similar since the heliocentric radial distance is relatively small, of the order 2.3 AU, and a high-latitude position. The solid circles and crosses superimposed on the plots are to give an indication of how fast (or slow) the heliocentric radial distance and the latitude of the spacecraft changed during an interval since these two parameters did not change linearly with time. It is clear from the first three intervals that generalised Fisk field agrees very well with the observed magnetic field.

The radial components of the Parker and generalised Fisk models seen in Figures 5.11a, 5.11c, and 5.11e agree very well with each other. In all three instances, the radial component of the models also follow the trend of the magnetic field. The effect of the decreasing latitude is seen in both Figures 5.11b and 5.11d where the separation between the two models again reduces to zero when crossing the equator on day 33 in Figure 5.11d. The azimuthal components of the generalised Fisk model follows the magnetic field better than the Parker model in these two intervals and the next interval (Figure 5.11f).

Figures 5.12a, 5.12c, and 5.12e show excellent agreement between both HMF models and the observed magnetic field. Figure 5.11b show the azimuthal components during the near northern pole crossing and, again, there is a better agreement between the generalised Fisk field predictions and the field data than the predictions of the Parker model. Up to this point, it has been showed the generalised Fisk field fares better than the Parker model, but according to Table 5.1, the 60° N - 30° N interval proofs to be the exception. The histograms of this interval (see section 5.3.1 and 5.3.2) showed the Parker model predicts a 48% - 52% distribution and 55% - 45% for the generalised Fisk field. In stark contrast, Figure 5.12d shows the generalised Fisk field fits the data significantly better. This could be the result of the histograms having an hourly-averaged resolution, binned statistically independent of time, and Figure 5.12d has three-day averaged resolution calculating the azimuthal component chronologically. Figure 5.12f shows the decreasing magnetic field strength with decreasing latitude, together with predictions of the two models merging when approaching the equator.

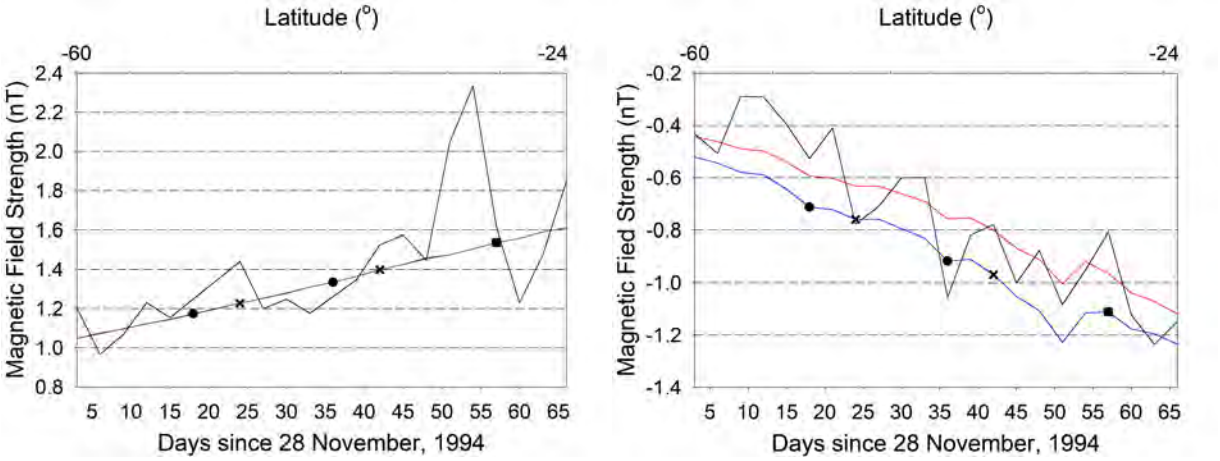

(a) Radial Component 60° S - 23° S

(b) Azimuthal Component 60° S - 23° S

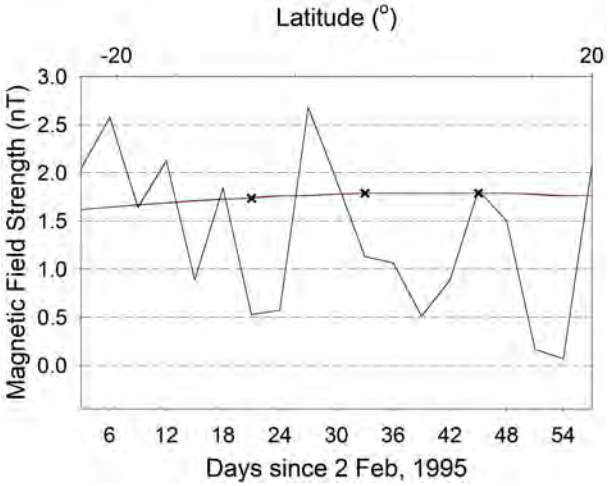

(c) Radial Component 23° S - 20° N

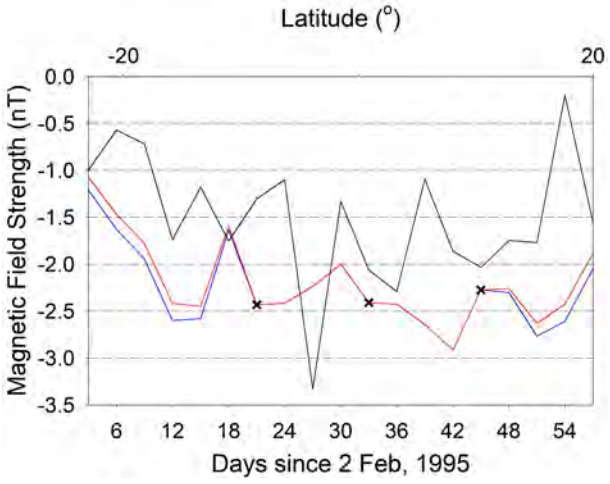

(d) Azimuthal Component 23° S - 20° N

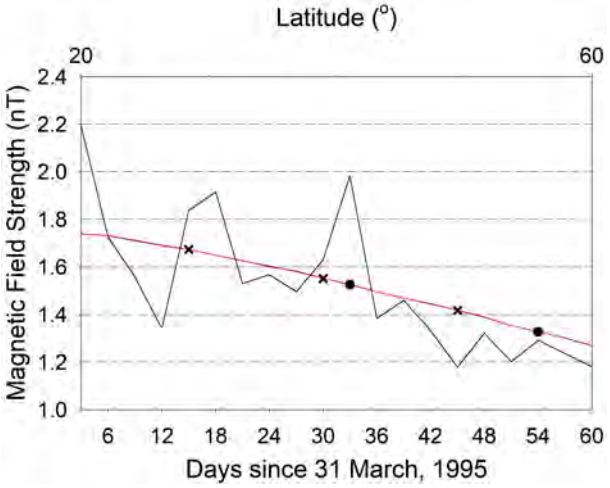

(e) Radial Component 20° N - 60° N

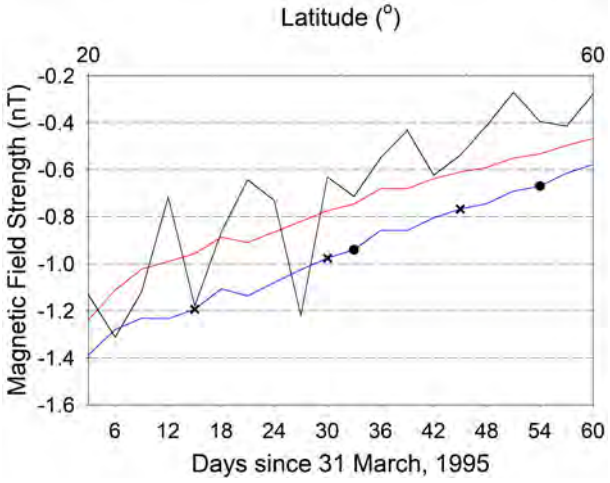

(f) Azimuthal Component 20° N - 60° N

Figure 5.11: Same as Figure 5.10 for the next three intervals. The solid black crosses represent time tickers placed every 10° scanned for all three intervals. The solid black circles represent time tickers placed every 0.1 AU travelled for the first two and last two panels. *Ulysses* only travelled 0.05 AU during the 23° S - 20° N interval.

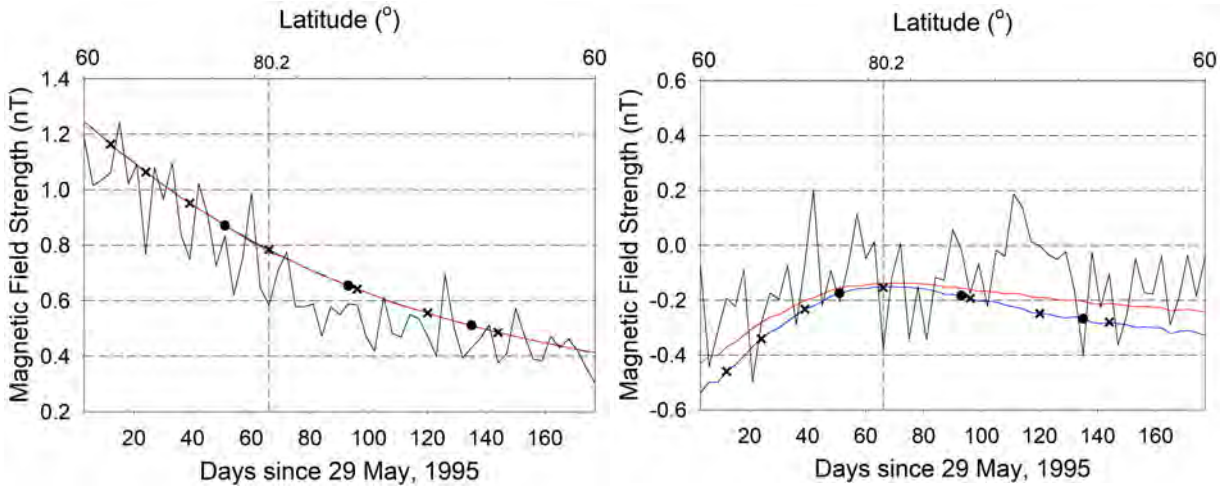

(a) Radial Component > 60° N

(b) Azimuthal Component > 60° N

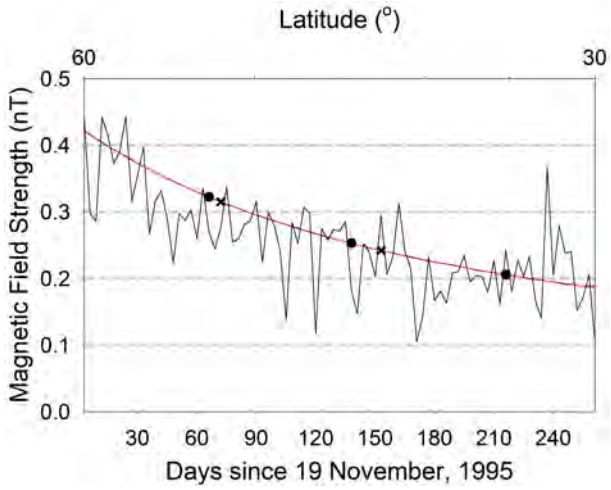

(c) Radial Component 60° N - 30° N

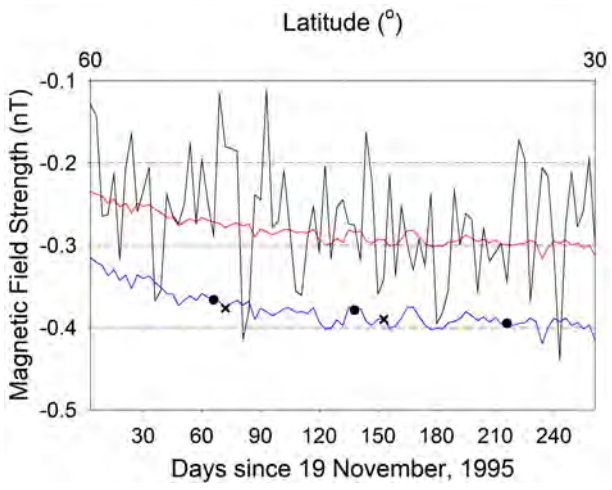

(d) Azimuthal Component 60° N - 30° N

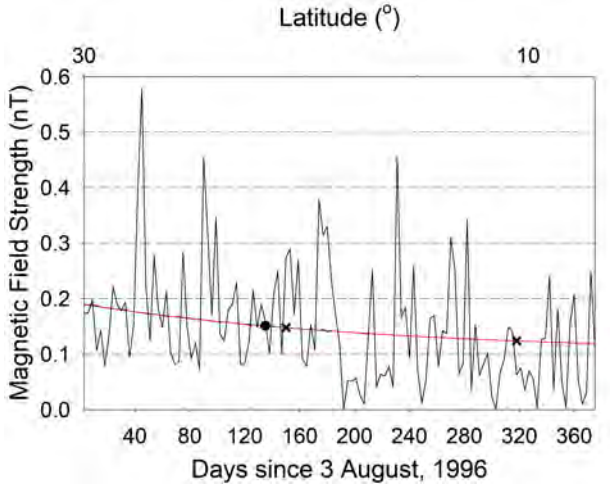

(e) Radial Component 30° N - 7° N

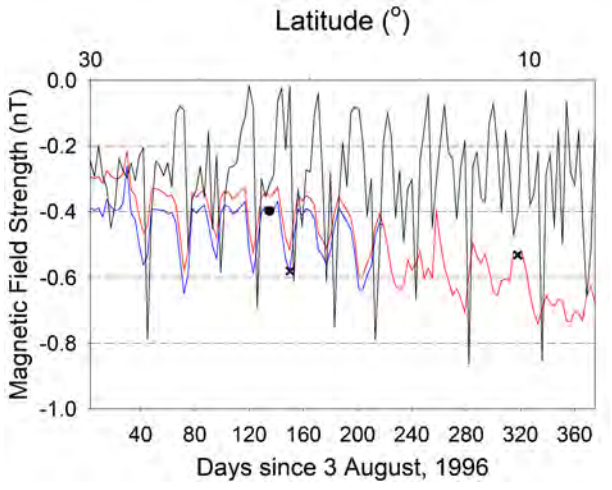

(f) Azimuthal Component 30° N - 7° N

Figure 5.12: Same as Figure 5.10 for the next three intervals. The solid black crosses represent time tickers placed every 10° scanned for all three intervals. The solid black circles represent time tickers placed every 0.1 AU travelled for the first two panels, 0.4 AU for the middle two panels, and 0.5 AU for the last two panels.

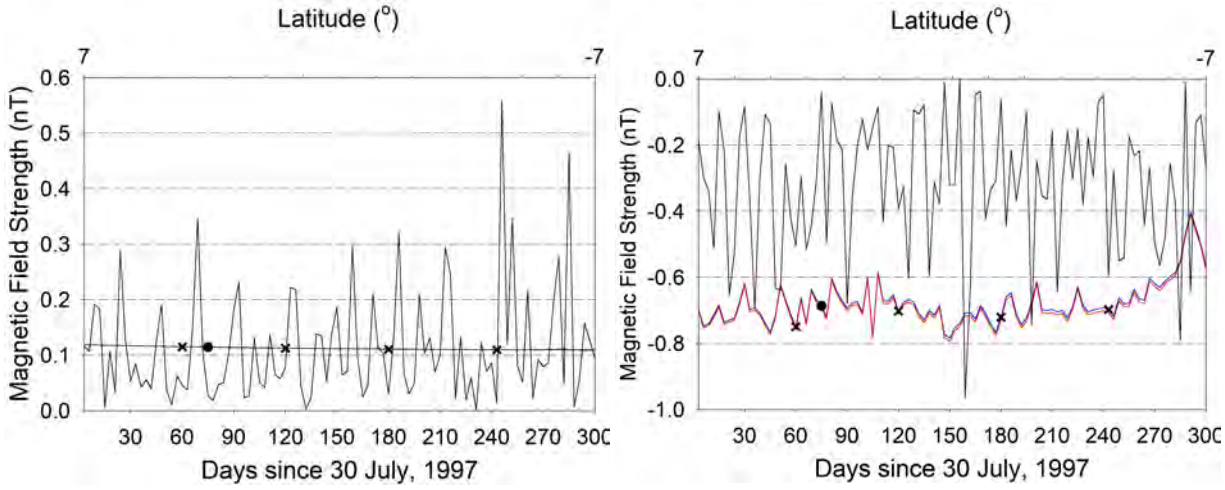

(a) Radial Component 7° N - 7° S

(b) Azimuthal Component 7° N - 7° S

Figure 5.13: Same as 5.10 for the last interval *Ulysses* scanned during its first orbit. The solid black crosses represent time tickers placed every 3° scanned while the solid black circles represent time tickers placed every 0.1 AU travelled.

Figure 5.13a shows the radial components of the Parker and generalised Fisk models agree very well with the observed magnetic field. Surprisingly, the azimuthal components of both models do not agree well with the observed field, although they agree well with each other as expected when crossing the equator. Table 5.1 echoes this result for this interval. This unexpected result can also be attributed to the statistical vs. chronological method of analyses described earlier.

5.5 Summary

In this chapter, magnetic field data from the *Ulysses* spacecraft mission was used to introduce magnetic field directions and subsequently the azimuth angles of the HMF. Comparisons between the observed azimuth angles and the modelled azimuth angles predicted by both the Parker and generalised Fisk models were shown in the form of polar plots and histograms. The polar plots gave a bird's-eye view of the data and an indication of how well the models fit. The histograms quantified the amount of over- and underwinding with a statistical description of the data.

Comparing the histograms of the two HMF models, it was clearly shown that the generalised Fisk model fits the data from *Ulysses* better than the Parker model for all intervals except one, namely the 60° N - 30° N interval. Furthermore, the magnetic field components, B_r and B_ϕ, of the observed magnetic field and the two HMF models were also compared as a function of time. The generalised Fisk model is better than the Parker model in predicting the observed magnetic field components, including the interval mentioned above. It is important to note that the histograms are independent of time and statistical in nature, while the comparison of field components are chronological in time.

Chapter 6

Neutron Monitor Data Analysis

6.1 Searching for a Signature

Chapter 3 mentions that if a Fisk-type field exists, its signature should be observable directly in magnetic field data and indirectly in the behaviour of cosmic rays being influenced by the field. Neutron monitors are used to observe cosmic-ray intensities, as well as the variations thereof, during the 11-year sunspot cycle and the 22-year solar magnetic cycle. Since the HMF is stable and well defined during solar minimum conditions, the effects of galactic cosmic rays (GCR) drifts due to gradients and curvature of the HMF may be revealed during this time, especially GCR variations with relatively small amplitudes [*Alania et al.*, 2008]. The subsequent sections in this chapter are devoted to the search for a Fisk-type field, in the variation of cosmic-ray intensities through both $A > 0$ and $A < 0$ solar magnetic epochs using neutron monitor data from several stations across the globe.

The question is what signature is expected? Since the solar wind drags the magnetic field lines out into the heliosphere with cosmic rays gyrating around it, the information of magnetic features on the photosphere will reach the Earth periodically as the Sun rotates (assuming this magnetic feature has a time scale longer than one solar rotation period). The sidereal period of the Sun is ~ 25 days. This is the period a stationary viewer will observe when tracking a feature on the surface of the Sun, while the synodic period is ~ 27 days. Therefore, neutron monitors stationed on the Earth should in principle detect recurrent cosmic-ray intensity variations close to 27 days (see *Richardson et al.* [1999], *Alania et al.* [2001], *Sabbah* [2007], and *Alania et al.* [2008]). Cosmic rays that are observed by neutron monitors have interacted with the HMF in their journey to Earth.

Firstly, Fisk-type fields occur because of well-developed polar coronal holes. The extend of these coronal holes follow the solar activity cycle (see, e.g. *Balogh and Erdõs* [2013], *Owens and Forsyth* [2013]) being the largest during solar minimum conditions. During such times it can be expected that the HMF would carry the imprint of periodicities longer than 27 days because the field lines originate at high latitudes on the photosphere. However, the field-line footpoints circling the imaginary $\vec{p}$-axis (see Figure 3.1) are all subjected to the rotation rate of this axis, which is the equatorial rotation rate. As was pointed out by *Burger et al.* [2008], the question of periodicities may be more complicated than previously thought. If there is a change in

periodicities, it should be more pronounced during solar minimum conditions. Here it should be kept in mind that it takes a finite time for cosmic rays to reach Earth. Particles that reach Earth after solar minimum, have actually experienced more of this solar minimum conditions in their journey to Earth than particles that reach Earth exactly at solar minimum.

By looking at neutron monitor data before, during and after solar minimum, it could therefore be expected that the imprint of a possible Fisk-type field would be more pronounced in cosmic rays observed after solar minimum.

Secondly, the theory predicts that Fisk-type fields are more pronounced at higher solar heliographic latitudes and the field is more Parker-like in the equatorial regions. In a drift picture of cosmic-ray modulation, protons that reach Earth during $A > 0$ cycles (e.g. 1977, 1997) would have travelled through the solar polar regions, and could carry some imprint of a Fisk-type field. On the other hand, during $A < 0$ cycles, such positively charged particles reach Earth through equatorial regions and would therefore be less likely to have interacted with the Fisk-like part of the HMF.

It could therefore be expected that the imprint of a possible Fisk-type field would be more pronounced in cosmic-ray protons during $A > 0$ cycles in the period following solar minimum at Earth. In this chapter recurrent cosmic-ray intensity variations and periodicities from four different solar minima periods, 1977, 1987, 1997, and 2009 are investigated.

6.2 Neutron Monitor Data Analysis

Based on their long-term reliability and data availability, seven neutron monitor stations were selected for the analyses to follow. These stations (with cut-off rigidity in brackets) are McMurdo (0.01 GV), Oulu (0.81 GV), Newark (1.97 GV), Kiel (2.32 GV), Moscow (2.46 GV), Hermanus (4.90 GV), and Potchefstroom (6.98 GV) in order of increasing cut-off rigidity [*Oh et al.*, 2013]. Hourly-averaged, pressure-corrected cosmic-ray counts from the Neutron Monitor Database (`nmdb.eu`) were used to calculate the daily averaged values at each neutron monitor station. For this study, the absolute value of the cosmic-ray intensities (counts per second) are not of importance, but rather their variation with time. The amplitude of CR intensity variations is calculated as a percentage with the use of the following expression:

$$\text{Amplitude} = \left| \frac{\text{Daily Mean} - \text{Running Average}}{\text{Daily Mean} + \text{Running Average}} \right| \times 100\% \tag{6.1}$$

The daily mean is calculated using the hourly-averaged data after which it is detrended by subtracting a running average of 27 days as suggested by *Richardson et al.* [1999]. During solar minimum conditions, infrequent occurrences of solar flares, coronal mass ejections (CMEs), or any other type of solar particle event is expected. That said, some events still occurred during this time and subsequently these events were removed from the data sets in order to find the quiet-time form of the HMF. In this study, the start of solar minimum is defined as when the tilt angle α reaches its minimum value. The neutron monitor data sets were subdivided such

that solar minimum occurred in the middle of a data set, that is, on day 45 for three months of data (~ 3 solar rotations). The reason for this subdivision is explained in section 6.1.

The data analyses involve the following processes: Firstly, the amplitude of the variation of a data set is calculated using Eq. 6.1. Secondly, a sinusoidal fit is superimposed to find both the amplitude and the period of a variation. Thirdly, this periodicity is then verified with a second software package, which identifies the dominant periodicity of a data set by using a Lomb periodogram (see *Lomb* [1976]). Lomb periodograms are very useful when trying to identify a periodicity, or periodicities, in either unevenly spaced data or when dealing with data gaps (see *Scargle* [1982] and *Horne and Baliunas* [1986]). If the two periodicities identified by the two separate software packages differ significantly, the results from the Lomb periodogram were used.

In the next two sections, detailed calculations for Hermanus and Oulu are shown, after which the results from the other stations are collectively presented.

6.2.1 Hermanus NM Station

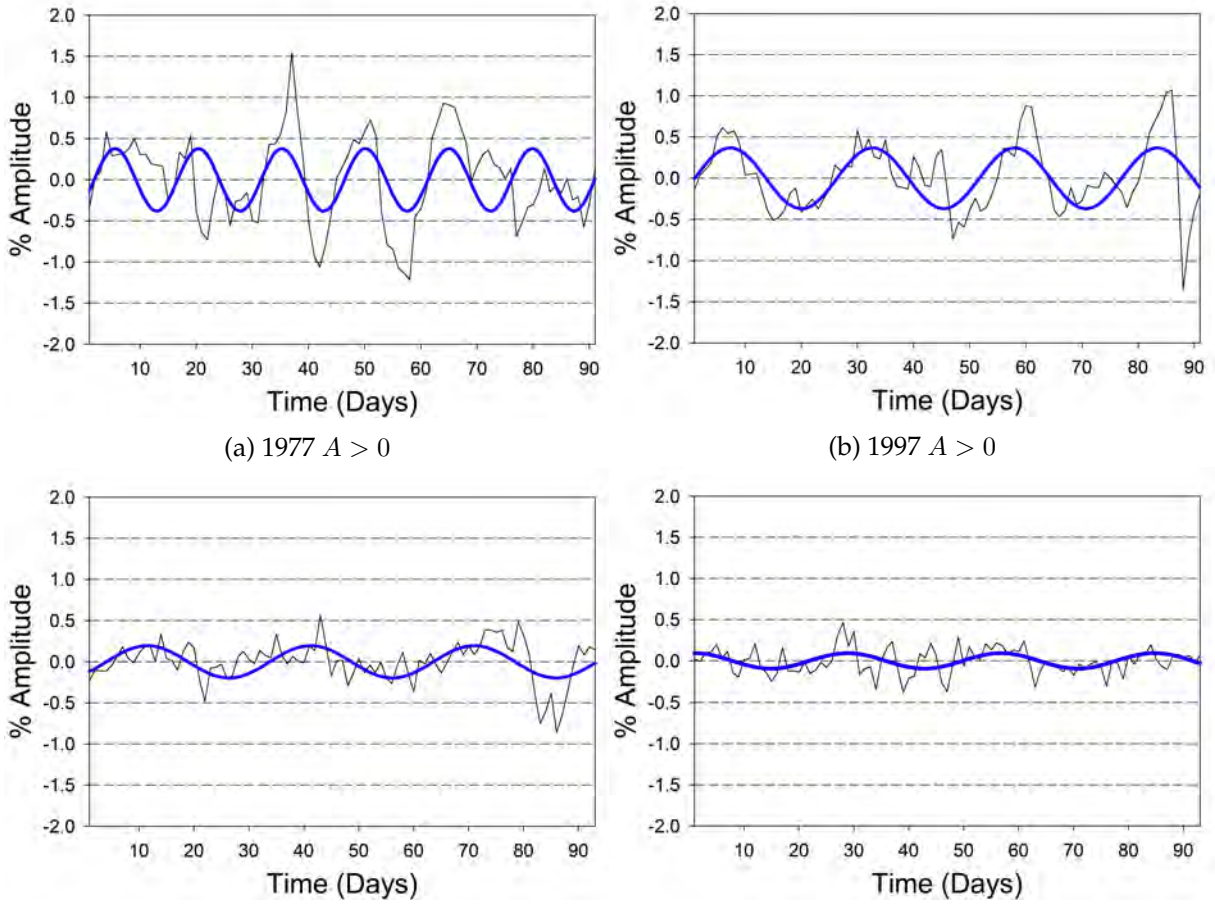

(a) 1977 $A > 0$

(b) 1997 $A > 0$

(c) 1987 $A < 0$

(d) 2009 $A < 0$

Figure 6.1: Panels (a) and (b) show variations of the neutron count rate at the NM stationed at Hermanus during the (a) 1977 and (b) 1997 solar minima ($A > 0$). The two bottom panels show the variations for the (c) 1987 and (d) 2009 solar minima ($A < 0$).

Figure 6.1 shows the variation of cosmic-ray intensities measured at the Hermanus NM station during both solar magnetic epochs under solar minimum conditions. Figures 6.1a and 6.1b show the $A > 0$ epoch of 1977 and 1997, while Figures 6.1c and 6.1d show the $A < 0$ epoch of 1987 and 2009. The horizontal axes of Figure 6.1 (a), (b), (c), and (d) represent the amount of days passed since 10 January 1977, 14 January 1997, 1 January 1987, and 28 August 2009, respectively, with solar minimum at day 45. A clear periodicity is seen in the NM data. The solid blue lines are from a sinusoidal fit. For this discussion, Figure 6.1 should be simultaneously considered with Figure 6.2 which shows the periodicities identified by a Lomb periodogram. Figures 6.1a, 6.1b, 6.1c, and 6.1d correspond to Figures 6.2a, 6.2b, 6.2c, and 6.2d.

Consider Figures 6.1a and 6.2a. The sinusoidal fit gives a periodicity of (14.9 ± 0.2) days

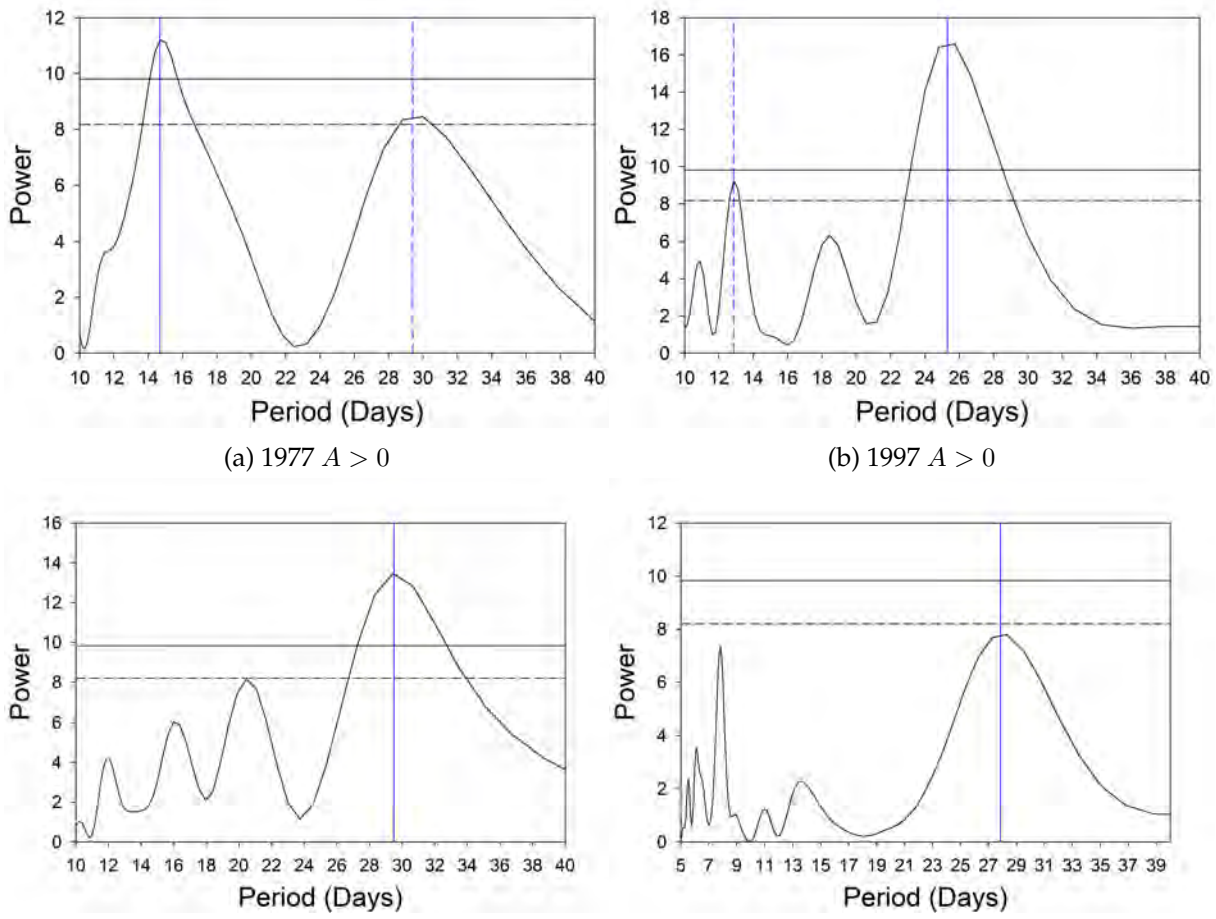

(a) 1977 $A > 0$ (b) 1997 $A > 0$

(c) 1987 $A < 0$ (d) 2009 $A < 0$

Figure 6.2: Panels (a) and (b) show the Lomb periodograms for the 1977 and 1997 solar minima ($A > 0$). The vertical and horizontal axes show the power and period identified in the data set. The two bottom panels (c) and (d) show the periodicities identified for the 1987 and 2009 solar minima ($A < 0$). The top solid reference line indicates the 99% confidence level, while the bottom dashed line indicates the 95% confidence level.

and the amplitude is $(0.38 \pm 0.06)\%$. A period of ~ 15 days can be attributed to an approximately half-solar rotation period variation since two co-rotating streams are normally sampled during one solar rotation [*Richardson et al.*, 1999]. The Lomb periodogram of Figure 6.2a shows a strong peak at ~ 15 days with a confidence level higher than 99% while a second, weaker periodicity is identified at 29.4 days with a confidence level above 95%. Figure 6.1b shows a

strong, dominant period of (25.35 ± 0.50) days and an amplitude of $(0.36 \pm 0.05)\%$. Its corresponding Lomb periodogram (Figure 6.2b) shows a second periodicity at 12.8 days which again could be due to a half-solar rotation period. The amplitudes of the variations of the cosmic-ray intensities for both $A > 0$ time periods are very similar at $\sim 0.4\%$.

Now consider Figures 6.1c and 6.2c. The former shows a period of (29.8 ± 0.8) days which is confirmed by the latter with a period of 29.5 days. The amplitude is $(0.19 \pm 0.03)\%$ and no other periodicities are identified in this data set. Moving to the periodicities during the 2009 solar minimum, a period of (27.9 ± 1) days was identified with an amplitude of $(0.09 \pm 0.02)\%$. Figure 6.2d shows the corresponding Lomb periodogram where a weak period of 27.8 days is identified. Although it falls below the 95% confidence level, the period corresponds to the expected synodic period of the Sun.

When comparing the amplitudes of the variations of both magnetic cycle epochs, a clear decrease in amplitude is visible from $A > 0$ to $A < 0$.

6.2.2 Oulu NM Station

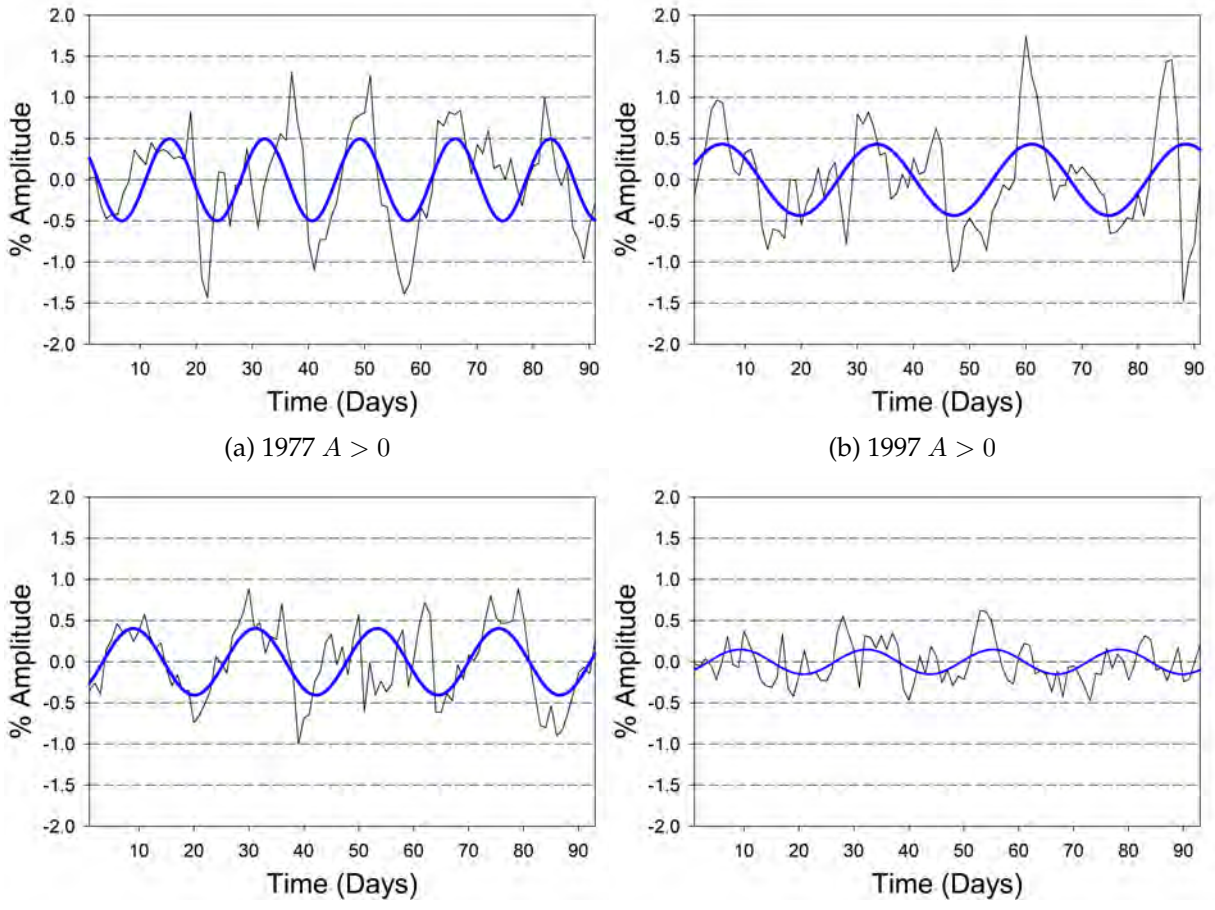

(a) 1977 $A > 0$

(b) 1997 $A > 0$

(c) 1987 $A < 0$

(d) 2009 $A < 0$

Figure 6.3: Panel (a) and (b) show the variations of the neutron count rate at the NM stationed in Oulu during the (a) 1977 and (b) 1997 solar minima ($A > 0$). Panels (c) and (d) show the variations for the 1987 and 2009 solar minima ($A < 0$), respectively.

Consider Figures 6.3a and 6.4a. The observed (black line) variation of the cosmic-ray intensities are indeed periodic with an identified (blue line) periodicity of (16.9 ± 0.2) days and an amplitude of $(0.50 \pm 0.07)\%$. A period of ~ 17 days is too high to be a potential half-solar rotation period, but too low to be indicative of the expected synodic period of the Sun. This periodicity is confirmed by the corresponding Lomb periodogram in Figure 6.4a where a high-power peak is visible at ~ 17 days. A second, much weaker periodicity is observed in Figure 6.4a at around ~ 30 days, but its power is too low to be of any significant value. Furthermore, Figure 6.3b shows good agreement between the observed variation and the identified periodicity of (27.5 ± 0.9) days and an amplitude of $(0.43 \pm 0.07)\%$. The Lomb periodogram (Figure 6.4b) confirms this period and also identifies a second period of 13 days which could be a half-solar rotation period.

Now consider Figures 6.3c and 6.4c. The dominant periodicity identified by the sinusoidal fit

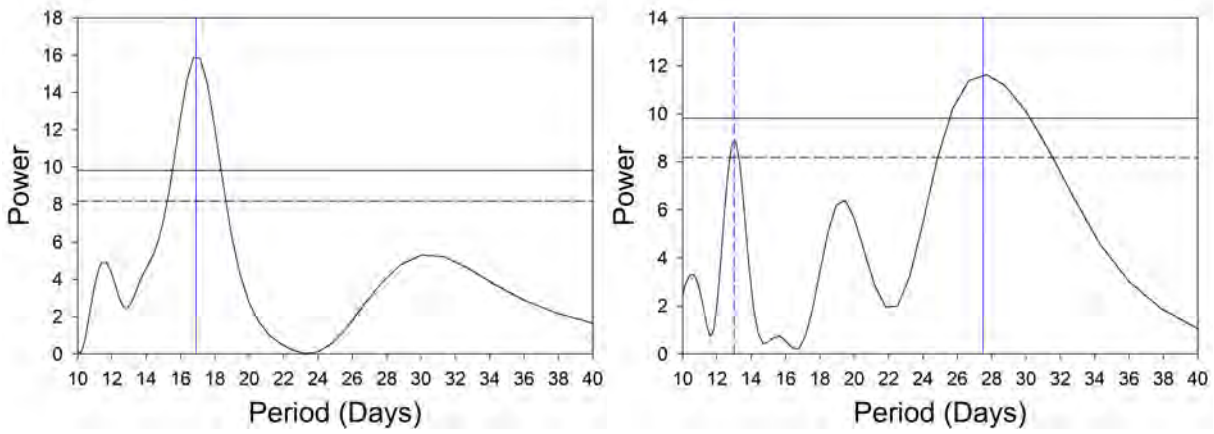

(a) 1977 $A > 0$

(b) 1997 $A > 0$

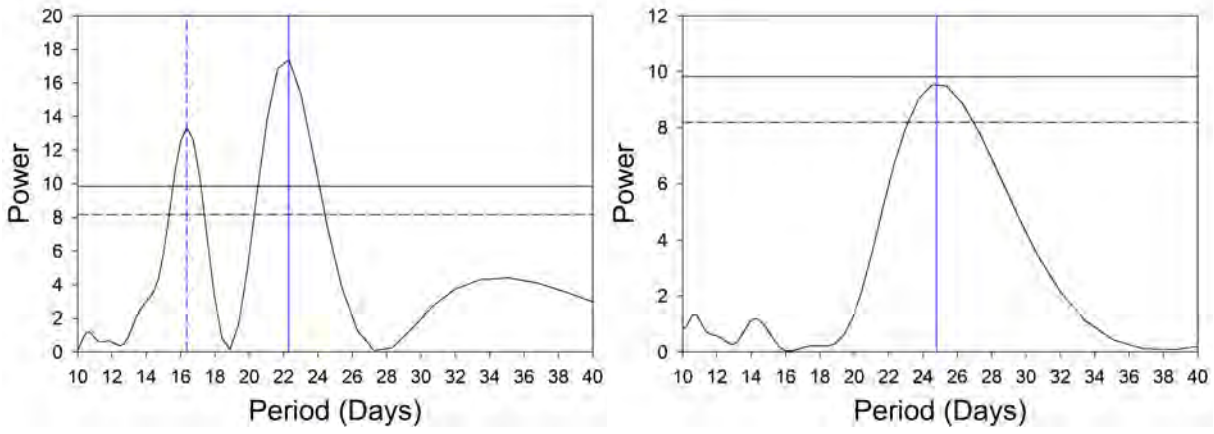

(c) 1987 $A < 0$

(d) 2009 $A < 0$

Figure 6.4: Panels (a) and (b) show the Lomb periodograms for the 1977 and 1997 solar minima ($A > 0$), respectively. The two bottom panels (c) and (d) show the periodicities identified for the 1987 and 2009 solar minima ($A < 0$). The top solid reference line indicates the 99% confidence level, while the bottom dashed line indicates the 95% confidence level.

(blue line) is (22.2 ± 0.4) days with an amplitude of $(0.40 \pm 0.05)\%$. The Lomb periodogram corroborates this periodicity and also identifies a second period of 16.3 days. Figure 6.3d shows a dominant period of (23.0 ± 0.7) days together with a relatively small amplitude of $(0.15 \pm$

$0.03)\%$. Its corresponding Lomb periodogram (Figure 6.4d) identifies a period of 24.8 days. Both NM stations agree on the observation that the amplitude deviation during the $A > 0$ epoch is larger relative to the $A < 0$ epoch. This will be discussed in the next section.

6.2.3 Comments on Neutron Monitor results

Following the results from Sections 6.2.1 and 6.2.2, a clear decrease in the amplitude of the cosmic-ray intensity variations is observed when comparing an $A > 0$ to an $A < 0$ solar magnetic cycle. In the case of the Hermanus NM station, the average amplitude is 0.37% during the $A > 0$ epoch, and only 0.14% during the $A < 0$ epoch. This amounts to a decrease of $\sim 60\%$. The amplitude at the Oulu NM station during the same time period showed a $\sim 40\%$ decrease from an average of 0.47% during the $A > 0$ epoch to 0.28% during the $A < 0$ epoch. This is in quantitative agreement with the results reported by *Richardson et al.* [1999] who investigated a 22-year cycle in the amplitude of recurrent, near-Earth, near-ecliptic GCR modulations during solar minima periods using NM data as well as integral and differential particle data from the *IMP 8* spacecraft. *Richardson et al.* [1999] showed that the amplitudes of recurrent intensity variations are $\sim 50\%$ larger during $A > 0$ epochs than during $A < 0$ epochs (see also *Alania et al.* [2001], *Alania et al.* [2008]). A possible explanation for this phenomena is the response of the CRs to solar wind speed enhancements seems to be reduced in *A*-negative conditions, although this is in contrast to what the drift model of CR modulation predicts (see, e.g., *Burger et al.* [2008]). However, Burger and co-workers have shown that Fisk-type fields can in principle explain the larger amplitudes during $A > 0$ epochs (see also *Engelbrecht* [2008]).

The dominant periods identified both by the Lomb periodograms and the sinusoidal fits are close to the 27-day synodic period. The average period detected for the $A > 0$ epoch in Hermanus is 26.2 days and 28.8 days during the $A < 0$ epoch. In Oulu, average periods of 22.3 days and 22.6 days are observed for the $A > 0$ and $A < 0$ epochs, respectively. Comparing the results of the two stations, it seems there is no solar-magnetic epoch dependence visible as in the case for the amplitude variations.

In the next section cosmic-ray data from several more NM stations are examined three months prior and three months after solar minimum.

6.2.4 Pre-, During, and Post- Solar Minimum Analysis

The exact time of solar minimum can be defined in different ways and as already mentioned, a minimum value for the tilt angle α defines solar minimum conditions in this study. If, however, solar minimum were defined by another parameter, eg. sunspot number, the intervals of three solar rotations to be examined can in principle be different from another study. Also, solar minimum conditions, carried by the solar wind, take some time to propagate throughout the heliosphere.. Therefore, neutron monitor data for approximately three solar rotations before, during, and after solar minimum were examined, with NM data centred on solar minimum for the middle interval.

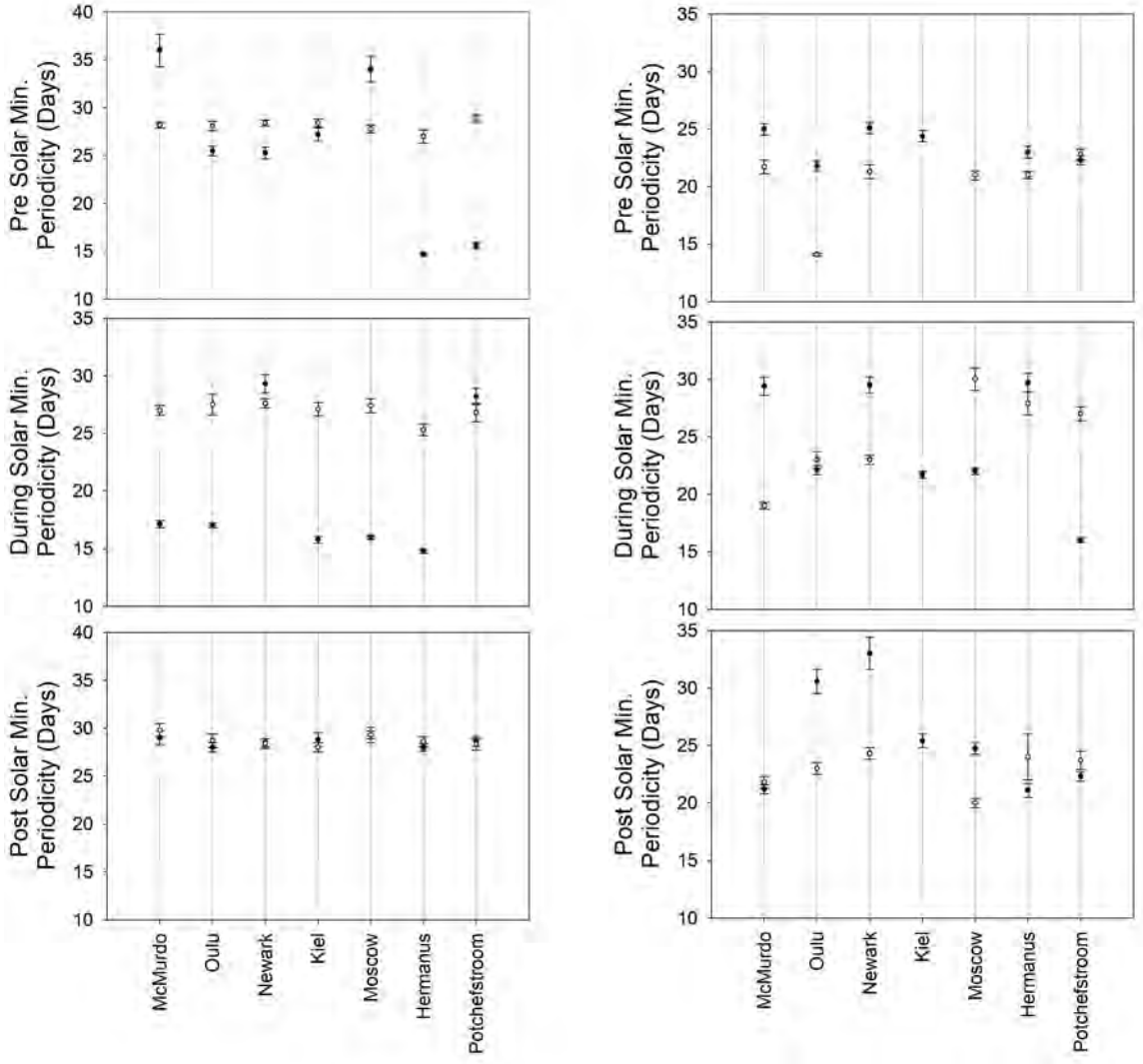

(a) 1977 and 1997 during the $A > 0$ epoch.

(b) 1987 and 2009 during the $A < 0$ epoch.

Figure 6.5: Pre-, during, and post solar minimum periodicities observed by NMs worldwide. The horizontal axis shows the NM station in order of increasing cut-off rigidity. Figure 6.5a is for the $A > 0$ epoch and Figure 6.5b for the $A < 0$ epoch. In Figure 6.5a solid black circles denote 1977 and open black circles 1997. In Figure 6.5b solid black circles denote 1987 and open black circles 2009.

The dominant periodicities identified at seven different NM stations (in order of increasing cut-off rigidity) are all presented in Figure 6.5, for $A > 0$ solar magnetic epochs on the left and $A < 0$ on the right. Data from 1977(1987) and 1997(2009) are presented with solid black circles and open black circles, respectively. The periods examined are from 10 October 1976 to 10 July 1977 and from 14 October 1996 to 14 July 1997 during the $A > 0$ epoch, and 1 October 1986 to 3 July 1987 and from 28 May 2009 to 28 February 2010 during the $A < 0$ epoch.

The top panel of Figure 6.5a shows an average periodicity of (25 ± 7) days prior to the solar minimum of 1977. The error margin of 7 days is quite high since McMurdo and Moscow stations report periodicities of 36 and 34 days, respectively. Also, Hermanus and Potchefstroom NM stations report a periodicity of ~ 15 days. If the latter is the detection of a half-solar rotation, it could in principle be indicative of a period of ~ 30 days. If these outlying periodicities

are temporarily excluded, the average periodicity during this time is (26.0 ± 0.9) days. During 1997, the average periodicity is (28.1 ± 0.6) days. A noticeable difference between the periodicities of 1977 and 1997 is observed during solar minimum in the second panel of Figure 6.5a. The average period of the former is (19 ± 6) days and (27.0 ± 0.7) for the latter. Remarkably, the entire $A > 0$ epoch shows very similar periodicities after solar minimum in the bottom panel of Figure 6.5a with an average periodicity of (28.7 ± 0.5) days.

Moving on to the top panel of Figure 6.5b, smooth and steady periodicities are observed for both 1987 and 2009 with average periods of (23 ± 2) days and (21.6 ± 0.7) days when excluding the outlier from Oulu in 2009. The middle panel shows an average period of (24 ± 5) days for 1987 and (25 ± 4) days for 2009. When examining the time period after solar minimum (bottom panel), two outliers are excluded, namely Oulu and Newark of 1987. Accordingly, the average periods are (23 ± 2) days and again (23 ± 2) days during 1987 and 2009, respectively. The lower periodicities during this time ($A < 0$) is echoed in Section 6.2.2 which seems to be a feature at all the NM stations prior, during, and after solar minimum.

Collectively, the periodicities prior to, during and after solar minimum condition during the $A > 0$ solar magnetic cycle does not seem to be vastly different from each other. The same is true for the $A < 0$ epoch. There is however an indication that periodicities in the three months after solar minimum during $A > 0$ epochs show very little scatter and an average value slightly larger than the synodic period. This may be a signature of a Fisk-type field as explained in section 6.1.

Next, the same method of presentation is used to show the amplitude of cosmic-ray intensity variations for seven different NM stations during both magnetic epochs. The left column of figures in Figure 6.6 show the amplitude variations prior to, during, and after solar minimum of the $A > 0$ epoch while the right column shows it for the $A < 0$ epoch. Table 6.1 summarizes the average amplitude variations. The top panel of Figure 6.5b shows the variations in amplitude is greater during 1977 than in 1997, but both being under 1%. During solar minimum, the amplitudes were much more similar with a combined average of $0.064 \pm 0.008\%$. After solar minimum, the scatter in amplitudes show much less scatter than for any other period, just as the case with the periodicities during this time period. Globally, Figure 6.5b shows a decrease in amplitude with increasing cut-off rigidity during the $A > 0$ epoch. Such a decrease can in principle be due to a Fisk-type field (see *Burger et al.* [2008]).

The top panel of Figure 6.2d shows that McMurdo station and Newark station recorded high amplitude variations prior to solar minimum in 1987. The rest of the amplitudes are grouped together below 0.6%. The amplitudes decreased during solar minimum (middle panel) to below 0.4%, except for the Kiel station in 1987. The bottom panel shows less scatter after solar minimum. The decrease in amplitude deviations with increasing cut-off rigidity is also noticed here during this $A < 0$ solar magnetic cycle. Also, the results of Sections 6.2.1 and 6.2.2 are validated here where the typically greater amplitudes during the $A > 0$ epoch has been established. The typically smaller amplitude values during the $A < 0$ epoch is shown in Table 6.1.

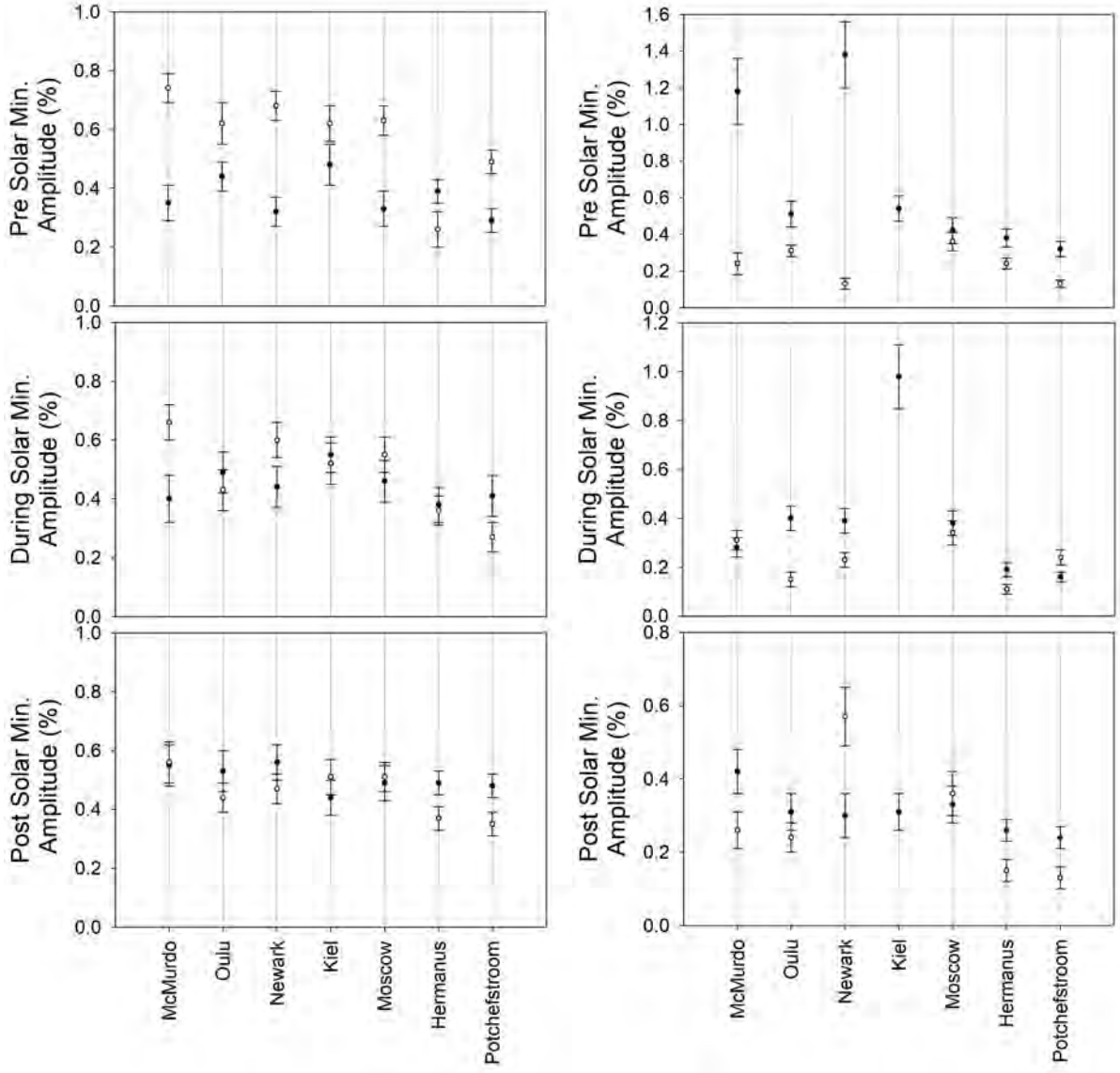

(a) 1977 and 1997 during the $A > 0$ epoch.

(b) 1987 and 2009 during the $A < 0$ epoch.

Figure 6.6: Pre-, during, and post solar minimum amplitude variations observed by NMs worldwide. The horizontal axis shows the NM station in order of increasing cut-off rigidity. Figure 6.6a is for the $A > 0$ epoch and Figure 6.6b for the $A < 0$ epoch. In Figure 6.6a solid black circles denote 1977 and open black circles 1997. In Figure 6.6b solid black circles denote 1987 and open black circles 2009.

Year	1977	1997	1987	2009
Pre	0.37 ± 0.06	0.57 ± 0.14	0.67 ± 0.39	0.23 ± 0.08
During	0.44 ± 0.05	0.48 ± 0.12	0.39 ± 0.25	0.23 ± 0.08
Post	0.50 ± 0.03	0.45 ± 0.07	0.31 ± 0.05	0.28 ± 0.14

Table 6.1: Summary of percentage amplitudes for both $A > 0$ (1977, 1997) and $A < 0$ (1987, 2009) epochs.

6.3 Summary

Recurrent cosmic-ray intensity variations were investigated in this chapter using neutron monitor data. The periodicities of the cosmic-ray intensities and the amplitude variations of such periodicities were also analysed. The least amount of scatter in periodicities were found during the $A > 0$ (1977 and 1997) epochs after solar minimum with values slightly larger than the synodic period of the Sun. This result adds to the evidence of a prevailing Fisk-type field since protons reaching the Earth during an $A > 0$ epoch travelled through the solar polar regions where the imprint of a Fisk-type field should be most observable. A $\sim 50\%$ decrease in amplitude variations were observed for $A < 0$ conditions compared with $A > 0$ conditions which agrees with previously published results (see *Richardson et al.* [1999]). This study confirms that the variation with amplitude decreases with increasing cut-off rigidity of the neutron monitor stations (see *Paizis et al.* [1999]), which is in qualitative agreement with the prediction of the signature of a Fisk-type field (see *Burger et al.* [2008], *Engelbrecht* [2008], *Sternal et al.* [2011]). The results of this chapter add to the pool of evidence pointing to the existence of Fisk-type fields.

Chapter 7

Summary and Conclusions

The main aim of this study was to introduce the generalised Fisk heliospheric magnetic field (HMF) model to test the existence of a Fisk-type field in the heliosphere. Since the Sun is the origin of any magnetic field model, the solar interior and atmosphere were investigated to ascertain the solar influences on magnetic field lines from beneath the solar surface to the solar wind source surface. All relevant influences on a magnetic field model, e.g. the solar-activity cycle, the heliospheric current sheet (HCS), the solar wind, etc., were briefly discussed.

Parker [1958] proposed the first successful HMF model and remains the preferred model by the cosmic-ray modulation community. On the other hand, *Fisk* [1996] introduced a model that challenged the traditional view of the HMF and remains a source of controversy, despite the fact that the Fisk field is based on irrefutable physical assumptions. This Fisk model was the first model to point out and include the relationship between the behaviour of the magnetic field at large radial distances away from the Sun to its corresponding behaviour on the photosphere. The Parker model works best in the equatorial region, while the Fisk model works best at high latitudes where open magnetic field lines eminating from polar coronal holes are found. Therefore, based on the model of *Fisk* [1996], *Burger and Hitge* [2004] introduced the Fisk-Parker hybrid HMF model which is valid at all solar latitudes.

The differential rotation rate ω of the photosphere is implemented differently for different HMF models. The divergence-free generalised Fisk field model implements a meridional and azimuthal dependent ω by making use of new transformations mapping observed magnetic field lines from the solar wind source surface to the photosphere uniquely to identify the differential rotation rate of an individual field line on the source surface. This results in an HMF model that is valid across all solar latitudes, whether the field line maps back to the polar or equatorial regions.

Magnetic field data from the *Ulysses* spacecraft mission were used to compare the observed magnetic field with the generalised Fisk model during its first orbit around the Sun in solar minimum conditions. The data analysis method of *Forsyth et al.* [2002] was used in this study. Histograms were used to bin the magnetic field directions to separate sunward and anti-sunward directed field lines, and to quantify the amount of over- and underwinding. The histograms of *Forsyth et al.* [2002] were compared to those of the generalised Fisk field model, and found that the latter corresponds to a better representation of the actual magnetic field,

except during one interval. The same conclusion is found when the observed magnetic field components, B_r and B_ϕ, are compared to those predicted by the Parker and generalised Fisk models, except this time the generalised Fisk model agrees with the data throughout all the scanned intervals. This surprising result is attributed to the fact that the histograms are a statistical approach independent of time, and the component analysis is chronological in time.

Cosmic-ray intensities from neutron monitors around the globe were used to investigate 26-day recurrent cosmic-ray intensity variations. Data sets before, during, and after solar minimum for both solar magnetic epochs were analysed. It was found that the amplitude of the variations were $\sim 50\%$ larger during an $A > 0$ epoch, than during an $A < 0$ epoch [*Richardson et al.*, 1999], and that the amplitude variations decrease with increasing cut-off rigidity [*Paizis et al.*, 1999]. The largest Fisk-effect is expected from positive particles sampling the polar regions of the Sun during an $A > 0$ epoch reaching the Earth. The least amount of scatter in data for both amplitudes and periodicities is seen during the three months following solar minimum in 1997 ($A > 0$) where all the neutron monitor stations used in this study reported a cosmic-ray intensity periodicity close to the synodic period of the Sun.

Considering the magnetic field and cosmic-ray data, it seems clear that a Fisk-type field cannot be ignored. It was shown that the generalised Fisk field model agrees better with magnetic field data, while the cosmic-ray data showed the expected signature of a Fisk-type field. No evidence contradicting the existence a Fisk-type field was found in this study, leading to the natural conclusion that the heliospheric magnetic field is more Fisk-like than previously thought.

This research hopes to stimulate more studies in the following areas:

- The generalised Fisk field model can be modified to include more time-dependent phenomena, e.g. a solar-cycle dependence, thereby including the time evolution of the boundaries of polar coronal holes both on the photosphere and source surface.
- The generalised Fisk field model assumes the polar coronal holes are symmetric about the magnetic axis $\vec{M}$ in contrast to the Fisk-Parker hybrid field where symmetry about the rotational axis $\vec{\Omega}$ is assumed. Changing this assumption in the current study may lead to interesting results, especially in the equatorial region since the model would not be symmetric around the $\vec{M}$-equator any more.
- It would be interesting to use the generalised Fisk field to model azimuth angles and magnetic field strength components outside the orbit of *Ulysses*, e.g. at large radial distances over the solar poles, to investigate the possible structure of the HMF in that region.
- Lastly, although it was outside the scope of this study to implement the generalised Fisk field in a numerical modulation code, it is the natural next step to show whether this HMF model can accurately predict cosmic-ray intensities in the heliosphere.

Acknowledgements

The author wishes to express his gratitude to several persons and institutions:

- Prof. R.A. Burger, my supervisor, for his valuable guidance, gracious leadership, and thought-provoking motivation. Thank you for teaching me, above all else, the importance of enjoying research while always maintaining one's moral integrity.
- Prof. S.E.S. Ferreira, Director of Research at the Centre for Space Research, for welcoming me into his department on my first day and always being available to guide, motivate, and teach.
- Mrs. Petro Sieberhagen, Mrs. Elanie van Rooyen, and Mrs. Lee-Ann van Wyk for their administrative assistance.
- The South African National Space Agency who provided the funding for this research, as well as sending me to the SANAE 4 base in Antarctica during the time of this study.
- The Centre for Space Research at the North-West University for the use of their facilities and additional financial assistance.
- Dr. Johan Steyn for evaluating the grammar and spelling of this dissertation.
- Mr. Benjamin Oberholzer for the countless discussions we had on various occasions. I would like to thank him for his friendship and willingness to help.

A special thanks to:

- My wife, Linell, whose unwavering support carried me through this venture. I would also like to thank her for her inspiration and reminding me of my own hopes and dreams.
- My parents, Johan and Yollanda Steyn, Mauritz and Lerinda Ellis, and Aubrey and Isabè Green for letting me pursue my career choice. I would also like to thank my brother, Wian, and my sister, Elanda, for their support.
- God, Who introduced me to His Creation using science, and letting me start my research career at the heartbeat of the heliosphere, the Sun.

Ruhann Steyn

Centre for Space Research, North-West University, Potchefstroom Campus, 2520, South Africa

Bibliography

Alania, M. V., D. G. Baranov, M. I. Tyasto, and E. S. Vernova, 27-Day variations of galactic cosmic rays and changes of solar and geomagnetic activities, *Adv. Space Res.*, *27*(3), 619–624, 2001.

Alania, M. V., A. Gil, and R. Modzelewska, Study of the 27-day variations of the galactic cosmic ray intensity and anisotropy, *Adv. Space Res.*, *41*(2), 280–286, 2008.

Alfvén, H., On the existence of electromagnetic-hydrodynamic waves, *Arkiv for Astronomi*, *29*(2), 1–7, 1943.

Altschuler, M. D., and G. Newkirk, Magnetic fields and the structure of the solar corona. I: Methods of calculating coronal fields, *Solar Physics*, *9*(1), 131–149, 1969.

Balogh, A., and G. Erdõs, The Heliospheric Magnetic Field, *Space Sci. Rev.*, *176*(1), 177–215, 2013.

Balogh, A., R. J. Forsyth, E. A. Lucek, T. S. Horbury, and E. J. Smith, Heliospheric magnetic field polarity inversions at high heliographic latitudes, *Geophys. Res. Lett.*, *26*(6), 631–634, 1999a.

Balogh, A., R. G. Marsden, and E. J. Smith, *The Heliosphere Near Solar Minimun: The Ulysses Perspective*, 8–39 pp., Praxis Publishing Ltd., 2001.

Balogh, A., L. J. Lanzerotti, and S. T. Suess, *The Heliosphere through the Solar Activity Cycle*, Praxis Publishing Ltd., 2007.

Balogh, A., H. S. Hudson, K. Petrovay, and R. von Steiger, Introduction to the Solar Activity Cycle: Overview of Causes and Consequences, *Space Sci. Rev.*, *186*(1), 1–15, 2014.

Balogh, A., et al., The solar origin of corotating interaction regions and their formation in the inner heliosphere, *Space Sci. Rev.*, *89*(1), 141–178, 1999b.

Bierman, L., *The Solar Wind and the Interplanetary Media*, p. 150, McGraw-Hill, 1961.

Biermann, L., Kometenschweife und solare Korpuskularstrahlung, *Z. Astrophys.*, *29*, 274, 1951.

Bilenko, I. A., Coronal holes and the solar polar field reversal, *Astron. Astrophys.*, *396*(2), 657–666, 2002.

Bruno, R., and B. Bavassano, On the winding of the IMF spiral for slow and fast wind within the inner heliosphere, *Geophys. Res. Lett.*, *24*(18), 2267, 1997.

Burger, R. A., Cosmic-ray modulation and the heliospheric magnetic field, *Adv. Space Res.*, *35*(4), 636–642, 2005.

Burger, R. A., and M. Hitge, The effect of a Fisk-type heliospheric magnetic field on cosmic-ray modulation, *Astrophys. J. Lett.*, *617*(1), L73–L76, 2004.

Burger, R. A., T. P. J. Krüger, M. Hitge, and N. E. Engelbrecht, A Fisk-Parker hybrid heliospheric magnetic field with a solar-cycle dependence, *Astrophys. J.*, *674*(1), 511-519, 2008.

Burlaga, L. F., and N. F. Ness, Large-scale distant heliospheric magnetic field: Voyager 1 and 2 observations from 1986 through 1989, *J. Geophys. Res.*, *98*(A10), 17,451–17,460, 1993.

Burlaga, L. F., R. P. Lepping, K. W. Behannon, L. W. Klein, and F. M. Neubauer, Large-scale variations of the interplanetary magnetic field - Voyager 1 and 2 observations between 1-5 AU, *J. Geophys. Res.*, *87*(A6), 4345–4353, 1982.

Dorotovič, I., Area of Polar Coronal Holes and Sunspot Activity: Years 1939-1993, *Solar Physics*, *167*, 419–426, 1996.

Engelbrecht, N. E., On the heliospheric diffusion tensor and its effect on 26-day recurrent cosmic-ray variations, Master's thesis, North-West University, 2008.

Feldman, U., U. Schühle, K. G. Widing, and J. M. Laming, Coronal Composition above the solar equator and the north pole as determined from spectra acquired by the SUMER instrument on SOHO, *Astrophys. J.*, *505*(2), 999–1006, 1998.

Ferreira, S. E. S., The heliospheric transport of galactic cosmic rays and Jovian electrons, Ph.D. thesis, Potchefstroomse Universiteit vir Christelike Hoër Onderwys, 2002.

Fisk, L. A., Motion of the footpoints of heliospheric magnetic field lines at the Sun: Implications for recurrent energetic particle events at high heliographic latitudes, *J. Geophys. Res.*, *101*(A7), 15,547–15,554, 1996.

Fisk, L. A., T. H. Zurbuchen, and N. A. Schwadron, On the Coronal Magnetic Field: Consequences of Large-Scale Motions, *Astrophys. J.*, *521*(2), 868–877, 1999a.

Fisk, L. A., T. H. Zurbuchen, and N. A. Schwadron, Coronal Hole Boundaries and their Interactions with Adjacent Regions, *Space Sci. Rev.*, *87*(1), 43–54, 1999b.

Forsyth, R. J., A. Balogh, E. J. Smith, G. Erdös, and D. J. McComas, The underlying Parker spiral structure in the Ulysses magnetic field observations, 1990-1994, *J. Geophys. Res.*, *101*(A1), 395–404, 1996.

Forsyth, R. J., A. Balogh, E. J. Smith, and J. T. Gosling, Ulysses observations of the northward extension of the heliospheric current sheet, *Geophys. Res. Lett.*, *24*(23), 3101–3104, 1997.

Forsyth, R. J., A. Balogh, and E. J. Smith, The underlying direction of the heliospheric magnetic field through the Ulysses first orbit, *J. Geophys. Res.*, *107*(A11), 1405, 2002.

Giacalone, J., Particle transport and acceleration at corotating interaction regions., *Adv. Space Res.*, *23*(3), 581–590, 1999.

Gizon, L., T. L. Duvall, and J. Schou, Wave-like properties of solar supergranulation, *Nature*, *421*(6918), 43–44, 2003.

Gosling, J. T., and V. J. Pizzo, Formation and evolution of corotating interaction regions and their three dimensional structure, *Space Sci. Rev.*, *89*(1), 21–52, 1999.

Hale, G. E., The Zeeman Effect in the Sun, *Publ. Astron. Soc. Pac.*, *20*(123), 287, 1908.

Hathaway, D. H., The Solar Cycle, *Living Rev. Solar Phys.*, *12*(1), 2015.

Hattingh, M., The modulation of galactic cosmic rays in a three-dimensional heliosphere, Ph.D. thesis, Potchefstroomse Universiteit vir Christelike Hoër Onderwys, 1998.

He, H.-Q., and R. Schlickeiser, Effects of latitudinally dependent solar wind Speed on diffusion coefficients of cosmic rays in the presence of adiabatic focusing, *Astrophys. J.*, *800*(2), 117, 2015.

Hoeksema, J. T., X. Zhao, and P. H. Scherrer, Prediction of coronal and heliospheric magnetic fields: the promise of SOI-MDI on SOHO., in *American Institute of Physics Conference Series*, vol. 382, edited by D. Winterhalter, J. T. Gosling, S. R. Habbal, W. S. Kurth, and M. Neugebauer, pp. 76–79, 1996.

Horne, J. H., and S. L. Baliunas, A prescription for period analysis of unevenly sampled time series, *Astrophys. J.*, *302*(1), 757–763, 1986.

Intriligator, D. S., J. Intriligator, and W. R. Webber, Examination of the Voyager 2 plasma observations in the vicinity of the termination shock, *AGU Fall Meeting Abstracts*, 2008.

Jokipii, J. R., and J. Kota, The polar heliospheric magnetic field, *Geophys. Res. Lett.*, *16*(1), 1–4, 1989.

Jokipii, J. R., and B. Thomas, Effects of drift on the transport of cosmic rays. IV - Modulation by a wavy interplanetary current sheet, *Astrophys. J.*, *243*(1), 1115–1122, 1981.

Jokipii, J. R., E. H. Levy, and W. B. Hubbard, Effects of particle drift on cosmic-ray transport. I - General properties, application to solar modulation, *Astrophys. J.*, *213*, 861–868, 1977.

Kobylinski, Z., Comparison of the Fisk magnetic field with the standard parker IMF: consequences for diffusion coefficients, *Adv. Space Res.*, *27*(3), 541–546, 2001.

Kopp, R. A., and T. E. Holzer, Dynamics of coronal hole regions. I - Steady polytropic flows with multiple critical points, *Solar Physics*, *49*(1), 43–56, 1976.

Kota, J., and J. R. Jokipii, Cosmic rays and the global heliospheric magnetic field: Meridional motion of footpoints, *28th International Cosmic Ray Conference*, *7*, 3791, 2003.

Krüger, T. P., The effect of a Fisk-type heliospheric magnetic field on cosmic-ray modulation, Master's thesis, North-West University, 2005.

Langer, U., Effects of termintation shock acceleration on cosmic rays in the heliosphere, Ph.D. thesis, Potchefstroomse Universiteit vir Christelike Hoër Onderwys, 2004.

Lomb, N. R., Least-squares frequency analysis of unequally spaced data, *Astrophys. Space. Sci.*, *39*(2), 447–462, 1976.

Maunder, E. W., Sunspot Variation in Latitude, *Popular Astronomy*, *12*, 616–619, 1904.

McComas, D. J., et al., Ulysses' return to the slow solar wind, *Geophys. Res. Lett.*, *25*(1), 1–4, 1998.

McComas, D. J., et al., The heliosphere's interstellar interaction: No bow shock, *Science*, *336*(6086), 1291–1293, 2012.

Moraal, H., Proton modulation near solar minimim periods in cosecutive solar cycles, *21st International Cosmic Ray Conference*, *6*, 140, 1990.

Mullan, D. J., *Physics of the Sun*, CRC Press., 2009.

Ness, N. F., and L. F. Burlaga, Spacecraft studies of the interplanetary magnetic field, *J. Geophys. Res.*, *106*(A8), 15,803–15,818, 2001.

Nolte, J. T., A. S. Krieger, A. F. Timothy, R. E. Gold, E. C. Roelof, G. Vaiana, A. J. Lazarus, J. D. Sullivan, and P. S. McIntosh, Coronal holes as sources of solar wind, *Solar Physics*, *46*(2), 303–322, 1976.

Oh, S., J. W. Bieber, P. Evenson, J. Clem, Y. Yi, and Y. Kim, Record neutron monitor counting rates from galactic cosmic rays, *J. Geophys. Res.*, *118*(9), 5431–5436, 2013.

Owens, M. J., and R. J. Forsyth, The Heliospheric Magnetic Field, *Living Rev. Solar Phys.*, *10*(5), 2013.

Paizis, C., et al., Amplitude evolution and rigidity dependence of the 26-day recurrent cosmic ray decreases: COSPIN/KET results, *J. Geophys. Res.*, *104*(A12), 28,241–28,248, 1999.

Parker, E., The passage of energetic charged particles through interplanetary space, *Planetary Space Science*, *13*(1), 9–49, 1965.

Parker, E. N., Dynamics of the interplanetary gas and magnetic fields., *Astrophys. J.*, *128*, 664, 1958.

Potgieter, M. S., Solar modulation of cosmic rays, *Living Rev. Solar Phys.*, *10*(3), 3, 2013.

Priest, E., M. G. Kivelson, and C. T. Russell, *Introduction to Space Physics*, Cambridge University Press, 1995.

Richardson, I. G., H. V. Cane, and G. Wibberenz, A 22-year dependence in the size of near-ecliptic corotating cosmic ray depressions during five solar minima, *J. Geophys. Res.*, *104*(A6), 12,549–12,562, 1999.

Roberts, D. A., J. Giacalone, J. R. Jokipii, M. L. Goldstein, and T. D. Zepp, Spectra of polar heliospheric fields and implications for field structure, *J. Geophys. Res.*, *112*(A8), A08103, doi: 10.1029/2007JA012247, 2007.

Roelof, E. C., G. M. Simnett, R. B. Decker, L. J. Lanzerotti, C. G. Maclennan, T. P. Armstrong, and R. E. Gold, Reappearance of recurrent low-energy particle events at Ulysses/HI-SCALE in the northern heliosphere, *J. Geophys. Res.*, *102*(A6), 11,251–11,262, 1997.

Sabbah, I., Twenty-seven-day variation of galactic cosmic rays, *Solar Physics*, *245*(1), 207–217, 2007.

Scargle, J. D., Studies in astronomical time series analysis. II - Statistical aspects of spectral analysis of unevenly spaced data, *Astrophys. J.*, *263*(1), 835–853, 1982.

Schatten, K. H., J. M. Wilcox, and N. F. Ness, A model of interplanetary and coronal magnetic fields, *Solar Physics*, *6*(3), 442–455, 1969.

Scherer, K., and H. Fichtner, The return of the bow shock, *Astrophys. J.*, *782*(1), 25, 2014.

Schou, J., et al., Helioseismic studies of differential rotation in the solar envelope by the solar oscillations investigation using the Michelson Doppler imager, *Astrophys. J.*, *505*(1), 390–417, 1998.

Schwabe, M., Sonnenbeobachtungen im Jahre 1843. Von Herrn Hofrath Schwabe in Dessau, *Astronomische Nachrichten*, *21*(495), 233, 1844.

Schwadron, N. A., An explanation for strongly underwound magnetic field in co-rotating rarefaction regions and its relationship to footpoint motion on the the sun, *Geophys. Research Lett.*, *29*(14), 1663, 2002.

Simpson, J. A., Solar origin of changes in the primary cosmic radiation, *Proceedings of the National Academy of Science*, *43*(1), 42–56, 1957.

Simpson, J. A., Cosmic radiation: Particle astrophysics in the heliosphere, *Annals of the New York Academy of Sciences*, *655*, 95–137, 1992.

Simpson, J. A., The Cosmic Ray Nucleonic Component: The Invention and Scientific Uses of the Neutron Monitor - (Keynote Lecture), *Space Sci. Rev.*, *93*, 11–32, 2000.

Simpson, J. A., et al., Cosmic ray and solar particle investigations over the south polar regions of the sun, *Science*, *268*(5213), 1019–1023, 1995.

Smith, C. W., and J. W. Bieber, Solar cycle variation of the interplanetary magnetic field spiral, *Astrophys. J.*, *370*(1), 435–441, 1991.

Snodgrass, H. B., Magnetic rotation of the solar photosphere, *Astrophys. J.*, *270*(1), 288–299, 1983.

Sternal, O., N. E. Engelbrecht, R. A. Burger, S. E. S. Ferreira, H. Fichtner, B. Heber, A. Kopp, M. S. Potgieter, and K. Scherer, Possible evidence for a Fisk-type heliospheric magnetic field. I. Analyzing Ulysses/KET electron observations, *Astrophys. J.*, *741*, 23, 2011.

Steyn, R., and R. A. Burger, A general Fisk-type model of the heliospheric magnetic field, *South African Journal of Science and Technology*, *34*(1), 2015.

Stoker, P. H., L. I. Dorman, and J. M. Clem, Neutron monitor design improvements, *Space Sci. Rev.*, *93*(1), 361–380, 2000.

Stone, E. C., A. C. Cummings, F. B. McDonald, B. C. Heikkila, N. Lal, and W. R. Webber, Voyager 1 explores the termination shock region and the heliosheath beyond, *Science*, *309*(5743), 2017–2020, 2005.

Strauss, R. d. T., Modelling of anomalous cosmic rays, Master's thesis, North-West University, 2010.

Thomas, B. T., and E. J. Smith, The Parker spiral configuration of the interplanetary magnetic field between 1 and 8.5 AU, *J. Geophys. Res.*, *85*(A12), 6861–6867, 1980.

Van Niekerk, Y., An investigation into the causes and consequences of north-south asymmetries in the heliosphere, Master's thesis, Potchefstroomse Universiteit vir Christelike Hoër Onderwys, 2000.

Wang, Y.-M., and J. N. R. Sheeley, On potential field models of the solar corona, *Astrophys. J.*, *392*(1), 310–319, 1992.

Wilcox, J. M., and N. F. Ness, Quasi-stationary corotating structure in the interplanetary medium, *J. Geophys. Res.*, *70*(23), 5793–5805, 1965.

Woo, R., S. R. Habbal, R. A. Howard, and C. M. Korendyke, Extension of the polar coronal hole boundary into interplanetary space, *Astrophys. J.*, *513*(10), 961–968, 1999.

Zank, G. P., Faltering steps into the galaxy: The boundary regions of the heliosphere, *Annu. Rev. Astron. Astrophys.*, *53*, 449–500, 2015.

Zhang, M., A linear relationship between the latitude gradient and 26 day recurrent variation in the fluxes of galactic cosmic rays and anomalous nuclear components. I. Observations, *Astrophys. J.*, *488*(2), 841–853, 1997.

Zhao, X.-P., and A. J. Hundhausen, Organization of solar wind plasma properties in a tilted, heliomagnetic coordinate system, *J. Geophys. Res.*, *86*(A7), 5423–5430, 1981.

Zurbuchen, T. H., A new view of the coupling of the sun and the heliosphere, *Annu. Rev. Astron. Astrophys.*, *45*(1), 297–338, 2007.

Zurbuchen, T. H., N. A. Schwadron, and L. A. Fisk, Direct observational evidence for a heliospheric magnetic field with large excursions in latitude, *Journal of Geophysical Research: Space Physics*, *102*(A11), 24,175–24,181, 1997.